

1N-01
48163
P. 98

Development and Validation of a Blade-Element Mathematical Model for the AH-64A Apache Helicopter

M. Hossein Mansur

(NASA-TM-108863) DEVELOPMENT AND
VALIDATION OF A BLADE-ELEMENT
MATHEMATICAL MODEL FOR THE AH-64A
APACHE HELICOPTER (Army Aviation
Systems Command) 98 p

N95-26710

Unclass

G3/01 0048163

April 1995



National Aeronautics and
Space Administration



US Army
Aviation and Troop Command

Aeroflightdynamics Directorate
Moffett Field, CA 94035-1000

Development and Validation of a Blade-Element Mathematical Model for the AH-64A Apache Helicopter

*M. Hossein Mansur, Aeroflightdynamics Directorate, U.S. Army Aviation and Troop
Command, Ames Research Center, Moffett Field, California*

April 1995



National Aeronautics and
Space Administration

Ames Research Center
Moffett Field, CA 94035-1000



US Army
Aviation and Troop Command

Aeroflightdynamics Directorate
Moffett Field, CA 94035-1000

Development and Validation of a Blade-Element Mathematical Model for the AH-64A Apache Helicopter

M. Hossein Mansur
Aeroflightdynamics Directorate
U.S. Army Aviation and Troop Command
Ames Research Center

Summary

A high-fidelity blade-element mathematical model for the AH-64A Apache Advanced Attack Helicopter has been developed by the Aeroflightdynamics Directorate of the U.S. Army's Aviation and Troop Command (ATCOM) at Ames Research Center. The model is based on the McDonnell Douglas Helicopter Systems' (MDHS) Fly Real Time (FLYRT) model of the AH-64A (acquired under contract) which was modified in-house and augmented with a blade-element-type main-rotor module. This report describes, in detail, the development of the rotor module, and presents some results of an extensive validation effort.

Introduction

High-fidelity simulation models of helicopters are needed for a variety of tasks including handling qualities evaluations, pilot training, simulation of life-cycle upgrades, and accident investigations. Many different approaches are currently used to develop mathematical models for helicopters. These approaches can be organized into three distinct categories (ref. 1): 1) analytical models, 2) identified models, and 3) combinations of 1 and 2. Analytical models rely on dynamic and aerodynamic theories and usually attempt to model each component of the helicopter individually. The combined, end-to-end, responses of such models are generally accurate for the dominant responses and nonlinearities, but are often imprecise in modeling rotor dynamics, especially in the off-axis (ref. 2). Identified models, on the other hand, use available vehicle-response data (collected through flight testing) to generate models which accurately characterize the end-to-end responses of an existing aircraft. Such models are commonly used during prototype testing for optimization of flight control systems, where very accurate response prediction is critical. In addition, they are very useful bases for simulation model validation, as is demonstrated herein. Identified models generally do not attempt to treat the components of the helicopter individually and their region of validity is restricted to the configuration and the linear response at the flight condition of the identification. Further, there is no way to identify models of aircraft still under development (prior to first flight) since there can be no access to flight-test data for such vehicles.

Component type models are, therefore, the only way to simulate helicopters during the design phase, and provide the best way to simulate aircraft over their entire flight envelope. The latter is

especially true at extreme conditions, such as may be encountered in accident investigations. Aside from their applicability to the entire flight envelope, however, there is a further advantage to making the investment of time and resources needed to develop a component type model of an existing helicopter. This advantage is the availability of flight-test data, which allows engineers to perform the extensive testing and comparisons of simulation and aircraft responses that are necessary to develop new modeling methods or enhance existing ones. These new or enhanced methods can then be applied to the modeling of both existing and future helicopters, improving our modeling capability overall.

In the late 1980s the U.S. Army initiated efforts to obtain a high-fidelity component type model for the AH-64A Apache helicopter (fig. 1). The effort was prompted by the success of two pilot-in-the-loop UH-60 accident-investigation-simulations conducted at NASA Ames. Those simulations were conducted using a component-type model of the Black Hawk known as GenHel, developed by Sikorsky and expanded/improved at Ames (ref. 3). A model with comparable complexity and fidelity was sought for the AH-64A.

As a result of a competitive procurement effort, the best available model for the AH-64A, the McDonnell Douglas Helicopter Systems' (MDHS) Fly Real Time (FLYRT) (ref. 4), was obtained including validation-flight-data in hover and forward flight. FLYRT responses were shown to match the provided flight data reasonably well. However, a great shortcoming of FLYRT was perceived to be its main-rotor module which is based on a map-type approach. This modeling approach was originally conceived in the late 70s to allow real-time operation with the limited computational capabilities available at that time (ref. 5). The approach relies on a pregenerated map to determine the rotor's quasi-steady response at each cycle. First-order-lag approximations to rotor dynamics are then added to these quasi-steady values to complete the rotor response. The problem with this technique is one of complete dependency on and restriction by this pregenerated map, especially since the code for the generation of more maps was not provided as part of FLYRT. The restriction was deemed surmountable since the computational power of current computers makes it possible to run blade-element models in real-time, without the need for the generation of a map.

A blade-element-type main-rotor module was therefore developed to replace the map-type module in FLYRT. The goal was to achieve the flexibility that a blade-element-type module, unburdened by the restrictions of a pregenerated map, would provide. Further, the access that a blade-element-type rotor module allows to the actual physical parameters of the rotor would make it possible to introduce corrections, enhancements, and new theories as they are developed. It would therefore allow for continual improvement, which would not have been possible with the map-type rotor module. The new rotor was incorporated into FLYRT, along with additional modifications as necessary. The new model is known as the Blade-Element Model for APache (BEMAP). BEMAP has been validated in comparison with available flight data in hover and forward flight in both time and frequency domains. The frequency-domain validation methods draw heavily on the tools contained in CIPHER^R (Comprehensive Identification from FrEQUENCY Responses) (ref. 6), as will be discussed. This report describes, in detail, the derivation of the rotor equations for the blade-element rotor module. It also presents some results from the validation effort. In every case, FLYRT responses have been included for comparison. Note, however, that the intent is not to show superiority of one model to the other but to show that the blade-element rotor module has been derived and implemented correctly.

Mathematical Model Description

To facilitate the introduction of the blade-element rotor module, FLYRT was first extensively modified. The modifications included: 1) reorganization of the code to improve modularity, 2) improvements in its input/output capability, and 3) addition of a plotting capability not provided under the contract. The basic structure of the new rotor module is based on the main-rotor module of GenHel (ref. 7), with the relevant equations for modeling the AH-64A derived with the aid of the symbolic manipulation program MACSYMA (ref. 8). The derivation of the rotor equations was part of an earlier effort, initiated by Chen (ref. 9), to develop complete blade dynamic equations for fully articulated configurations which use one of the three hinge arrangements most commonly used, i.e., lag-flap-pitch (l-f-p), flap-lag-pitch (f-l-p), and flap-pitch-lag (f-p-l). Chen derived the inertial portion of the equations using a Lagrangian approach, making no high order or small angle assumptions. MACSYMA was later used to rederive the same equations using a Newtonian approach, again making no high order or small angle assumptions. The two sets of equations were compared and were found to be in general agreement. Though the Apache uses an f-p-l hinge sequence, the simpler f-l-p sequence was used in the new rotor module. The choice was made in order to avoid the added complexity that would have resulted from treating blade pitch as a degree of freedom. The reasoning was that given the small lead-lag angles, the increased accuracy achieved by using the actual f-p-l sequence would be minimal.

The new rotor was then integrated into FLYRT to create BEMAP. This also required the replacement of the trim module and the modification of the equations-of-motion (EOFM) module, as will be discussed later. The modules representing other components of the Apache helicopter, i.e., fuselage/empennage/wings, vertical tail/tail rotor, horizontal stabilator, and landing gears were used directly from FLYRT with minimal changes required for implementation. The Digital Automatic Stabilization Equipment (DASE) model used in FLYRT was also retained, however, extensive modifications to allow introduction of control inputs from flight-data were made. BEMAP is, therefore, a version of FLYRT which has been: 1) equipped with a blade-element main-rotor module, 2) upgraded with new trim and modified equations-of-motion modules, 3) restructured to improve modularity, 4) enhanced with flight-data-control-input access capability for flight-data comparisons, and 5) updated with a versatile plotting option.

The development of the new blade-element model will be discussed in detail in the next section. The trim module and the modifications to the equations-of-motion module will also be briefly discussed subsequently. No attempt is made in this report, however, to redocument the modules which remain functionally unchanged or only slightly changed from FLYRT. The description and documentation of those modules can be found in reference 4, generated by MDHS as part of the contract to deliver FLYRT to the Army.

Development of the Rotor Module

In order to minimize the development time of the blade-element main-rotor module, the main-rotor module of Sikorsky/Ames GenHel was used as a basic structure. To develop an AH-64A version of this rotor, it was necessary to: 1) modify the module to allow noncollocated flap and lead-lag hinges, 2) replace all UH-60-specific data with AH-64A-specific data, 3) incorporate new aerodynamic coefficient tables and new table-lookup and interpolation routines, and 4) replace all UH-60-specific equations with AH-64A-specific equivalents.

Like the GenHel main-rotor (ref. 3), the BEMAP rotor considers flapping, lead-lag, rotor rotational speed, and inflow degrees of freedom. An equal-annuli method (ref. 7), modified for noncollocated hinges, was implemented to divide each blade into elements. Equations for the local velocity and acceleration of each element were then derived based on aircraft and blade (lead-lag, flapping, and rotational) motions and the element's position with respect to the aircraft Center of Gravity (C.G.).

The local velocity, along with local inflow and wind, determine the local angle of attack and Mach number for entry into the aerodynamic coefficient tables. The coefficients are then used to calculate components of the aerodynamic force and moment per blade element. Summing these over all the blade-elements results in the aerodynamic forces and moments per blade. No dynamic twisting or bending of the blades were modeled. The preformed linear twist of the blades, however, is represented through adjustments of the blade-element pitch angle.

The local acceleration at the blade element was used to derive equations for the inertial forces and moments per blade. Unlike the case of aerodynamic forces, the blade elements used for the inertial derivations were differential elements and analytical integration, rather than numerical summation, was used along the blade span. No simplifying assumptions were made in the derivation of the equations (aside from the assumption of rigid blades) and, therefore, the equations are quite complex. They, however, provide a good tool for exploring the effects of higher order terms (usually dropped) on the fidelity of the rotor module.

The derivation of the equations for the rotor forces, rotor moments, and the coupled flapping and lead-lag equations of motion are provided in the following subsections and appendix A. Simple MACSYMA macros developed to aid in the derivations have also been provided (app. B). The aerodynamic portion of the equations follow the methods used in the GenHel main rotor (ref. 7), modifying for the AH-64A as necessary. Following the GenHel structure, the BEMAP rotor module contains its own integration algorithm which gives flapping and lagging positions and velocities in the rotating frame. The AH-64A specific data and the aerodynamic-coefficient tables were obtained from the "Air Vehicle Technical Description Data for the AH-64A Advanced Attack Helicopter," reference 10. For angles of attack between -5 deg and $+30$ deg the values of section lift and drag coefficients are from wind-tunnel tests and are functions of local angle of attack and Mach number. For angles of attack from $+30$ deg to $+355$ deg the values of section lift and drag coefficients are from C-81 equations (ref. 11), are independent of Mach number, and the lift coefficient data include the increase in maximum lift due to dynamic stall.

The inflow components are calculated using the Pitt/Peters inflow model implemented as described by Peters and HaQuang in their AHS Technical Note (ref. 12). The model, which is based on unsteady actuator-disk theory, is valid for forward flight as well as hover and uses coefficients of aerodynamic thrust, pitching moment, and rolling moment to calculate the three induced velocity states.

Derivation of Rotor Equations

As mentioned previously, the symbolic manipulation program MACSYMA was used to derive the rotor equations using a Newtonian approach. Figure 2(a) shows the coordinate systems used in the derivations. As can be seen, the model assumes a fully articulated rotor hub using flapping and lead-lag hinges in a flap-lag-pitch hinge arrangement, the flapping hinge being closest to the center of rotation. From the rotor shaft up, the rotating-shaft (rs) frame has its origin at the rotor hub and its y-axis

along the blade segment between the hub and the flapping hinge and rotating with the rotor. Frame 3 is similar to the rotating-shaft system except that its origin is at the flapping hinge. Frame 2 also has its origin at the flapping hinge but has its y-axis along the blade-segment between the flapping and the lead-lag hinges, i.e., rotated about the negative x-axis through β (flapping up is positive). Finally, frame 1 is similar to frame 2 except that its origin is located on the lead-lag hinge.

Velocity and acceleration vectors at the rotor hub— The translational and rotational velocity and acceleration vectors at the main-rotor hub due to the motion of the helicopter are independent of the hinge sequence used for the rotor. These vectors are the result of the translational and rotational velocity and acceleration of the aircraft's C.G. and its separation from the rotor hub (refer to fig. 2(b)).

Let:

$$\vec{V}_{cgb} = \begin{Bmatrix} u \\ v \\ w \end{Bmatrix} = \text{Inertial translational velocity of aircraft C.G. (body axes)}$$

$$\vec{\omega}_{cgb} = \begin{Bmatrix} p \\ q \\ r \end{Bmatrix} = \text{Inertial rotational velocity of aircraft C.G. (body axes)}$$

$$\vec{l}_{hb} = \begin{Bmatrix} x_h \\ y_h \\ z_h \end{Bmatrix} = \text{Hub location relative to C.G. (body axes)}$$

The translational velocity at the rotor hub, in body axes, may then be calculated from:

$$\vec{V}_{hb} = \vec{V}_{cgb} + \vec{\omega}_{cgb} \times \vec{l}_{hb} \quad (1)$$

substituting, we get:

$$\vec{V}_{hb} = \begin{Bmatrix} u_{hb} \\ v_{hb} \\ w_{hb} \end{Bmatrix} = \begin{Bmatrix} u \\ v \\ w \end{Bmatrix} + \begin{Bmatrix} p \\ q \\ r \end{Bmatrix} \times \begin{Bmatrix} x_h \\ y_h \\ z_h \end{Bmatrix} = \begin{Bmatrix} u + qz_h - ry_h \\ v + rx_h - pz_h \\ w + py_h - qx_h \end{Bmatrix} \quad (2)$$

The translational acceleration at the rotor hub, in body axes, may be calculated in a similar manner. We have:

$$\dot{\vec{V}}_{hb} = \dot{\vec{V}}_{cgb} + \dot{\vec{\omega}}_{cgb} \times \vec{V}_{hb} \quad (3)$$

where,

$$\dot{\vec{V}}_{hb} = \begin{Bmatrix} \dot{u} + \dot{q}z_h - \dot{r}y_h \\ \dot{v} + \dot{r}x_h - \dot{p}z_h \\ \dot{w} + \dot{p}y_h - \dot{q}x_h \end{Bmatrix} \quad (4)$$

Performing the cross product and summing, the acceleration vector at the rotor hub (body axes) is found to be:

$$\dot{\vec{V}}_{hb} = \begin{Bmatrix} \dot{u} + qw - rv - (q^2 + r^2)x_h + (pq - \dot{r})y_h + (pr + \dot{q})z_h \\ \dot{v} + ru - pw + (pq + \dot{r})x_h - (r^2 + p^2)y_h + (qr - \dot{p})z_h \\ \dot{w} + pv - qu + (pr - \dot{q})x_h + (qr + \dot{p})y_h - (p^2 + q^2)z_h \end{Bmatrix} \quad (5)$$

To simplify the inclusion of the gravity terms in the analysis, the acceleration of gravity may be added to the hub acceleration vector at this point. This is similar to the way GenHel (ref. 7) deals with the gravity terms. The acceleration of gravity in body axes is found from:

$$\vec{a}_{gb} = \begin{bmatrix} 1 & 0 & 0 \\ 0 & \cos \phi & \sin \phi \\ 0 & -\sin \phi & \cos \phi \end{bmatrix} \begin{bmatrix} \cos \theta & 0 & -\sin \theta \\ 0 & 1 & 0 \\ \sin \theta & 0 & \cos \theta \end{bmatrix} \begin{Bmatrix} 0 \\ 0 \\ g \end{Bmatrix} = \begin{Bmatrix} -g \sin \theta \\ g \sin \phi \cos \theta \\ g \cos \phi \cos \theta \end{Bmatrix} \quad (6)$$

where θ and ϕ are pitch and roll attitudes of the helicopter, respectively. Since gravity is an external force, the negative of this acceleration should be added to the hub acceleration which will then be used for calculating the inertial forces and moments. The augmented hub acceleration vector is:

$$\vec{a}_{hb} = \begin{Bmatrix} a_{hbx} \\ a_{hby} \\ a_{hbz} \end{Bmatrix} = \begin{Bmatrix} \dot{u} + qw - rv - (q^2 + r^2)x_h + (pq - \dot{r})y_h + (pr - \dot{q})z_h + g \sin \theta \\ \dot{v} + ru - pw + (pq + \dot{r})x_h - (r^2 + p^2)y_h + (qr - \dot{p})z_h - g \sin \phi \cos \theta \\ \dot{w} + pv - qu + (pr - \dot{q})x_h + (qr + \dot{p})y_h - (p^2 + q^2)z_h - g \cos \phi \cos \theta \end{Bmatrix} \quad (7)$$

To transform the velocity and acceleration vectors from the body axes to a fixed-shaft axes (fig. 2(b)), assuming that the shaft is tilted longitudinally through an angle i_θ (tilt back positive) and laterally through an angle i_ϕ (tilt right positive), the acceleration vector in body axes should be multiplied by the transformation matrix:

$$[T_{tilt}] = \begin{bmatrix} \cos i_\theta & 0 & -\sin i_\theta \\ \sin i_\phi \sin i_\theta & \cos i_\phi & \sin i_\phi \cos i_\theta \\ \cos i_\phi \sin i_\theta & -\sin i_\phi & \cos i_\phi \cos i_\theta \end{bmatrix} \quad (8)$$

Therefore, the hub velocity and acceleration vectors in a fixed-shaft axes are:

$$\vec{V}_{hfs} = \begin{Bmatrix} u_{hfs} \\ v_{hfs} \\ w_{hfs} \end{Bmatrix} = [T_{tilt}] \begin{Bmatrix} u_{hb} \\ v_{hb} \\ w_{hb} \end{Bmatrix} \quad (9)$$

$$\vec{a}_{hfs} = \begin{Bmatrix} a_{hfsx} \\ a_{hfsy} \\ a_{hfsz} \end{Bmatrix} = [T_{tilt}] \begin{Bmatrix} a_{hbx} \\ a_{hby} \\ a_{hbz} \end{Bmatrix} \quad (10)$$

$$\vec{\omega}_{hfs} = \begin{Bmatrix} p_{fs} \\ q_{fs} \\ r_{fs} \end{Bmatrix} = [T_{tilt}] \begin{Bmatrix} p \\ q \\ r \end{Bmatrix} \quad (11)$$

Velocity and acceleration vectors at the blade element– In order to derive the inertial portion of the coupled flap-lag equations of motion using a Newtonian approach, the acceleration vector at an arbitrary blade element needs to be determined. The acceleration at the rotor hub in a fixed-shaft-axes system was derived previously. This acceleration vector has to be transformed to a rotating-shaft system and summed with the local acceleration vector. Referring to figure 2(c), the hub acceleration in a rotating-shaft system may be calculated by rotating the fixed-shaft-frame-vector through an angle $(\pi/2 - \psi)$ in the positive z_{fs} -direction. This is equivalent to multiplying by the rotation matrix:

$$[T_{fsrs}] = \begin{bmatrix} \cos(\pi/2 - \psi) & \sin(\pi/2 - \psi) & 0 \\ -\sin(\pi/2 - \psi) & \cos(\pi/2 - \psi) & 0 \\ 0 & 0 & 1 \end{bmatrix} \quad (12)$$

Simplifying the matrix and multiplying, we get:

$$\vec{a}_{hrs} = \begin{bmatrix} \sin \psi & \cos \psi & 0 \\ -\cos \psi & \sin \psi & 0 \\ 0 & 0 & 1 \end{bmatrix} \begin{Bmatrix} a_{hfsx} \\ a_{hfsy} \\ a_{hfsz} \end{Bmatrix} = \begin{Bmatrix} a_{hfsx} \sin \psi + a_{hfsy} \cos \psi \\ -a_{hfsx} \cos \psi + a_{hfsy} \sin \psi \\ a_{hfsz} \end{Bmatrix} \quad (13)$$

To calculate the contribution of the local flapping and lead-lag motion we first need to write the position vector of an arbitrary blade element in the rotating-shaft frame. Referring again to figure 2(a), the position vector in frame 1 is (note, that lead is positive):

$$\begin{Bmatrix} r_\delta \sin \delta \\ r_\delta \cos \delta \\ 0 \end{Bmatrix}$$

in frame 2:

$$\begin{Bmatrix} r_\delta \sin \delta \\ r_\delta \cos \delta + \Delta e \\ 0 \end{Bmatrix}$$

in frame 3:

$$\begin{bmatrix} 1 & 0 & 0 \\ 0 & \cos \beta & \sin \beta \\ 0 & -\sin \beta & \cos \beta \end{bmatrix} \begin{Bmatrix} r_\delta \sin \delta \\ r_\delta \cos \delta + \Delta e \\ 0 \end{Bmatrix} = \begin{Bmatrix} r_\delta \sin \delta \\ \cos \beta (r_\delta \cos \delta + \Delta e) \\ -\sin \beta (r_\delta \cos \delta + \Delta e) \end{Bmatrix} \quad (14)$$

and finally in the rotating-shaft frame:

$$\vec{r}_{rs} = \begin{Bmatrix} r_\delta \sin \delta \\ \cos \beta (r_\delta \cos \delta + \Delta e) + e_\beta \\ -\sin \beta (r_\delta \cos \delta + \Delta e) \end{Bmatrix} \quad (15)$$

The blade-element velocity vector in the rotating-shaft frame may then be calculated from:

$$\vec{V}_{rs} = \begin{Bmatrix} V_{rsx} \\ V_{rsy} \\ V_{rsz} \end{Bmatrix} = \dot{\vec{r}}_{rs} = \vec{V}_{hrs} + \vec{r}_{rs} + \vec{\omega}_{rs} \times \vec{r}_{rs} \quad (16)$$

where the hub velocity vector in a rotating-shaft frame is:

$$\vec{V}_{hrs} = \begin{Bmatrix} u_{fs} \sin \psi + v_{fs} \cos \psi \\ -u_{fs} \cos \psi + v_{fs} \sin \psi \\ w_{fs} \end{Bmatrix} \quad (17)$$

and the local derivative of the position vector is:

$$\dot{\vec{r}} = \begin{Bmatrix} r_\delta \dot{\delta} \cos \delta \\ -\dot{\beta} \sin \beta (r_\delta \cos \delta + \Delta e) - r_\delta \dot{\delta} \cos \beta \sin \delta \\ -\dot{\beta} \cos \beta (r_\delta \cos \delta + \Delta e) + r_\delta \dot{\delta} \sin \beta \sin \delta \end{Bmatrix} \quad (18)$$

The rotational velocity of the rotating-shaft axis is found by summing the rotations due to body and rotor motions, as follows:

$$\vec{\omega}_{rs} = \begin{Bmatrix} 0 \\ 0 \\ -\Omega \end{Bmatrix} + \begin{bmatrix} \sin \psi & \cos \psi & 0 \\ -\cos \psi & \sin \psi & 0 \\ 0 & 0 & 1 \end{bmatrix} \begin{Bmatrix} p_{fs} \\ q_{fs} \\ r_{fs} \end{Bmatrix} = \begin{Bmatrix} p_{fs} \sin \psi + q_{fs} \cos \psi \\ -p_{fs} \cos \psi + q_{fs} \sin \psi \\ r_{fs} - \Omega \end{Bmatrix} \quad (19)$$

MACSYMA was used for the derivation of the terms. Parameters in the MACSYMA derivations were given symbolic names representative of the notation used up to this point. For example, the blade-element velocity vector in the rotating-shaft frame (eq. 16) was developed as:

$$VRS = RRS DI = VHRS + RRS DL + CROSS3(OMEGARS, RRS)$$

where,

$$RRSDI \equiv \dot{\vec{r}}_{rs} \text{ (r, rotating-shaft, derivative, inertial)}$$

$$RRSDL \equiv \vec{r}_{rs} \text{ (r, rotating-shaft, derivative, local)}$$

and "CROSS3(X,Y)" is a simple MACSYMA macro that calculates the cross product of two 3-D vectors X and Y (included in app. B). The MACSYMA results are shown in appendix A. This velocity vector is later used, along with inflow and wind velocities, to calculate the aerodynamic forces and moments.

The blade-element acceleration vector in a rotating-shaft frame:

$$\vec{a}_{rs} = \begin{Bmatrix} a_{rsx} \\ a_{rsy} \\ a_{rsz} \end{Bmatrix} = \dot{\vec{V}}_{rs} = \vec{a}_{hrs} + \dot{\vec{r}}_{rs} + 2\vec{\omega}_{rs} \times \vec{r}_{rs} + \dot{\vec{\omega}}_{rs} \times \vec{r}_{rs} + \vec{\omega}_{rs} \times (\vec{\omega}_{rs} \times \vec{r}_{rs}) \quad (20)$$

is found in a similar manner:

ARS =

$$AHRs + RRSDDL + 2 * CROSS3(OMEGARS, RRS DL) + CROSS3(OMEGARSD, RRS) \\ + CROSS3(OMEGARS, CROSS3(OMEGARS, RRS))$$

where,

$$RRSDDL \equiv \ddot{r}_{rs} \text{ (r, rotating shaft, derivative, derivative, local)}$$

$$OMEGARSD \equiv \dot{\omega}_{rs} \text{ (omega, rotating shaft, derivative)}$$

MACSYMA results are again shown in appendix A.

Inertial Terms

Now that we have the inertial acceleration vector in the rotating-shaft frame, we can derive the inertial forces and moments and the inertial portion of the flap-lag equations of motion.

Blade inertial shears at the lead-lag hinge, rotating-shaft frame– The elemental inertial force may be written, in rotating-shaft frame, as:

$$\Delta \vec{F}_{irs} = -\Delta m \vec{a}_{rs} \quad (21)$$

The inertial force itself may then be written, in component form, as the sum of the elemental forces over the entire blade:

$$\vec{F}_{irs} = \begin{Bmatrix} F_{irsx} \\ F_{irsy} \\ F_{irsz} \end{Bmatrix} = \begin{Bmatrix} \sum -\Delta m a_{rsx} \\ \sum -\Delta m a_{rsy} \\ \sum -\Delta m a_{rsz} \end{Bmatrix} \quad (22)$$

where the summation is over all the blade-elements. Allowing MACSYMA to do the integration by letting:

$$M = \sum \Delta m : \text{Mass of one blade outboard of outer hinge}$$

$$FM = \sum \Delta m r_{\delta} : \text{First mass moment of one blade about outer hinge}$$

we find expressions for the components of the inertial shear at the lead-lag hinge in rotating-shaft axes. The resulting equations are quite long and are, therefore, not included. In fact, from here on only the MACSYMA output for the flapping and lead-lag equations have been included. All the intermediate equations, however, can be generated by following the derivations provided.

Blade inertial hub forces, rotating-shaft frame– The inertial forces at the hub in a rotating-shaft frame, for one blade, are the same as the inertial shears at the hinges. These were calculated before as:

$$\vec{F}_{irs} = \begin{Bmatrix} F_{irsx} \\ F_{irsy} \\ F_{irsz} \end{Bmatrix} = \begin{Bmatrix} \sum -\Delta m a_{rsx} \\ \sum -\Delta m a_{rsy} \\ \sum -\Delta m a_{rsz} \end{Bmatrix} \quad (23)$$

Blade inertial hub forces, fixed-shaft frame– The inertial hub forces in the fixed-shaft frame may be written, for one blade, as:

$$\vec{F}_{ifs} = \begin{bmatrix} \sin \psi & -\cos \psi & 0 \\ \cos \psi & \sin \psi & 0 \\ 0 & 0 & 1 \end{bmatrix} \begin{Bmatrix} F_{irsx} \\ F_{irsy} \\ F_{irsz} \end{Bmatrix} = \begin{Bmatrix} F_{irsx} \sin \psi - F_{irsy} \cos \psi \\ F_{irsx} \cos \psi + F_{irsy} \sin \psi \\ F_{irsz} \end{Bmatrix} \quad (24)$$

Blade inertial moment at the lead-lag hinge, frame 1– In order to derive the inertial moment at the lead-lag hinge, in frame-1, the acceleration vector needs to be defined in frame 1 (refer to fig. 2(a)). Since the acceleration vectors in frames 1 and 2 are identical and frame 2 is simply a single rotation through the flapping angle β up from the rotating-shaft frame, we have:

$$\vec{a}_2 = \begin{Bmatrix} a_{2x} \\ a_{2y} \\ a_{2z} \end{Bmatrix} = \begin{bmatrix} 1 & 0 & 0 \\ 0 & \cos \beta & -\sin \beta \\ 0 & \sin \beta & \cos \beta \end{bmatrix} \begin{Bmatrix} a_{rsx} \\ a_{rsy} \\ a_{rsz} \end{Bmatrix} = \begin{Bmatrix} a_{rsx} \\ a_{rsy} \cos \beta - a_{rsz} \sin \beta \\ a_{rsy} \sin \beta + a_{rsz} \cos \beta \end{Bmatrix} = \begin{Bmatrix} a_{1x} \\ a_{1y} \\ a_{1z} \end{Bmatrix} = \vec{a}_1 \quad (25)$$

Now, the moment at the lead-lag hinge may be written as:

$$\vec{M}_{il1} = \sum \vec{r}_{\delta 1} \times (-\Delta m \vec{a}_1) \quad (26)$$

where,

$$\vec{r}_{\delta 1} = \begin{Bmatrix} r_\delta \sin \delta \\ r_\delta \cos \delta \\ 0 \end{Bmatrix} \quad (27)$$

Therefore, the inertial moment at the lead-lag hinge is:

$$\vec{M}_{il1} = \begin{Bmatrix} M_{il1x} \\ M_{il1y} \\ M_{il1z} \end{Bmatrix} = \begin{Bmatrix} \sum -\Delta m r_\delta a_{1z} \cos \delta \\ \sum \Delta m r_\delta a_{1z} \sin \delta \\ \sum -\Delta m r_\delta (a_{1y} \sin \delta - a_{1x} \cos \delta) \end{Bmatrix} \quad (28)$$

Again allowing MACSYMA to do the integration, by additionally letting:

$$SM = \sum \Delta m r_\delta^2 : \text{Second mass moment of one blade about the outer hinge}$$

we get expressions for the components of the inertial moment at the lead-lag hinge.

The lead-lag equation of motion is simply the expression of the moment equilibrium about the lead-lag hinge (z_1 -axis) and will therefore only involve the M_{il1z} component of the inertial moment at the lead-lag hinge. Also, the lead-lag hinge does not support any moment about the z_1 -axis and therefore only the x_1 and y_1 components of the inertial moment are transferred down (except through the lead-lag dampers, which are considered independently).

Blade inertial moments at the flapping hinge, frame 2– Inertial moments at the flapping hinge come from two sources, 1) the moment of the inertial shear forces at the lead-lag hinge, 2) the moment transferred through the lead-lag hinge.

The inertial moment due to inertial shears at the lead-lag hinge may be written, in frame 2, as:

$$\vec{M}_{if21} = \begin{Bmatrix} 0 \\ \Delta e \\ 0 \end{Bmatrix} \times \begin{Bmatrix} F_{if1x} \\ F_{if1y} \\ F_{if1z} \end{Bmatrix} = \begin{Bmatrix} \Delta e F_{if1z} \\ 0 \\ -\Delta e F_{if1x} \end{Bmatrix} \quad (29)$$

where,

$$\begin{Bmatrix} F_{if1x} \\ F_{if1y} \\ F_{if1z} \end{Bmatrix} = \begin{bmatrix} 1 & 0 & 0 \\ 0 & \cos \beta & -\sin \beta \\ 0 & \sin \beta & \cos \beta \end{bmatrix} \begin{Bmatrix} F_{irsx} \\ F_{irsy} \\ F_{irsz} \end{Bmatrix} \quad (30)$$

The inertial moment transferred through the lead-lag hinge may be written, in frame 2, as:

$$\vec{M}_{if22} = \begin{Bmatrix} M_{il1x} \\ M_{il1y} \\ 0 \end{Bmatrix} \quad (31)$$

Then, the total inertial moment at the lead-lag hinge may be calculated as the sum of the two parts above,

$$\vec{M}_{if2} = \vec{M}_{if21} + \vec{M}_{if22} = \begin{Bmatrix} M_{if2x} \\ M_{if2y} \\ M_{if2z} \end{Bmatrix} = \begin{Bmatrix} M_{il1x} + \Delta e F_{if1z} \\ M_{il1y} \\ -\Delta e F_{if1x} \end{Bmatrix} \quad (32)$$

The flapping equation of motion is simply the expression of the moment equilibrium about the flapping hinge (x_2 -axis) and will therefore only involve the M_{if2x} component of the inertial moment at the flapping hinge. Also, the flapping hinge does not support any moment about the x_2 -axis and therefore only the y_2 and z_2 components of the inertial moment are transferred down.

Blade inertial hub moments, rotating-shaft frame— The inertial hub moment in the rotating-shaft frame, for one blade, is composed of two parts, 1) the moment of the inertial shear force at the flapping hinge, and 2) the moment transferred through the flapping hinge.

The moments due to inertial shears at the flapping hinge may be written, in rotating-shaft frame, as:

$$\vec{M}_{ihrs1} = \begin{Bmatrix} 0 \\ e_\beta \\ 0 \end{Bmatrix} \times \begin{Bmatrix} F_{irsx} \\ F_{irsy} \\ F_{irsz} \end{Bmatrix} = \begin{Bmatrix} e_\beta F_{irsz} \\ 0 \\ -e_\beta F_{irsx} \end{Bmatrix} \quad (33)$$

The moments due to nonflapping moments at the flapping hinge may be written, in rotating-shaft frame, as:

$$\vec{M}_{ihrs2} = \begin{bmatrix} 1 & 0 & 0 \\ 0 & \cos \beta & \sin \beta \\ 0 & -\sin \beta & \cos \beta \end{bmatrix} \begin{Bmatrix} 0 \\ M_{il1y} \\ -\Delta e F_{if1x} \end{Bmatrix} = \begin{Bmatrix} 0 \\ M_{il1y} \cos \beta - \Delta e F_{if1x} \sin \beta \\ -M_{il1y} \sin \beta - \Delta e F_{if1x} \cos \beta \end{Bmatrix} \quad (34)$$

So the total inertial moment at the hub may be calculated as the sum of the two parts above,

$$\vec{M}_{ihrs} = \vec{M}_{ihrs1} + \vec{M}_{ihrs2} = \left\{ \begin{array}{c} e_{\beta} F_{irsz} \\ M_{il1y} \cos \beta - \Delta e F_{if1x} \sin \beta \\ -M_{il1y} \sin \beta - \Delta e F_{if1x} \cos \beta - e_{\beta} F_{irsx} \end{array} \right\} \quad (35)$$

Blade inertial hub moments, fixed-shaft frame– The total inertial moment at the hub, in the fixed-shaft frame, can now be calculated by rotating from rotating to fixed-shaft frame:

$$\vec{M}_{ihfs} = \begin{bmatrix} \sin \psi & -\cos \psi & 0 \\ \cos \psi & \sin \psi & 0 \\ 0 & 0 & 1 \end{bmatrix} \left\{ \begin{array}{c} e_{\beta} F_{irsz} \\ M_{il1y} \cos \beta - \Delta e F_{if1x} \sin \beta \\ -M_{il1y} \sin \beta - \Delta e F_{if1x} \cos \beta - e_{\beta} F_{irsx} \end{array} \right\} \quad (36)$$

Multiplying, we get:

$$\vec{M}_{ihfs} = \left\{ \begin{array}{c} e_{\beta} F_{irsz} \sin \psi - M_{il1y} \cos \beta \cos \psi + \Delta e F_{if1x} \sin \beta \cos \psi \\ e_{\beta} F_{irsz} \cos \psi + M_{il1y} \cos \beta \sin \psi - \Delta e F_{if1x} \sin \beta \sin \psi \\ -M_{il1y} \sin \beta - \Delta e F_{if1x} \cos \beta - e_{\beta} F_{irsx} \end{array} \right\} \quad (37)$$

Aerodynamic Terms

The calculation of the aerodynamic forces and moments follows closely the implementation used by Howlett in GenHel (ref. 7). Specifically:

1. Treatment of the blade segment aerodynamic force calculation is completely nonlinear.
2. Bivariate maps, as a function of angle of attack and Mach number, are defined in the range -5 deg to +30 deg, allowing some accounting of blade stall effects.
3. For angles of attack from +30 deg to +355 deg, values of section lift and drag coefficients are from C-81 equations. These, along with the low-angle maps, provide a complete coverage of angles of attack, allowing some treatment of the aerodynamic characteristics on the retreating blade side of the rotor disk.
4. Simple sweep theory is used to modify the unyawed blade-element lift coefficients.
5. Reynolds number effects, unsteady flow effects, and compressibility have been ignored.

No attempt was made to improve the application of swept wing theory used to calculate elemental force components (tangential, radial, and normal) based on the lift and drag coefficients. The tables of coefficients themselves, however, and the lookup scheme used to access them were, of course, changed to represent the AH-64A Apache helicopter. Also, the different hinge sequence and the noncollocated hinges of the AH-64A required reformulation of the transfer of aerodynamic forces and moments. This in turn significantly modified the lead-lag and flapping equations as is detailed in the following derivations. For details of the lift and drag calculations using coefficients based on local angle of attack and Mach number, and the details of sweep theory used for enhancing the 2-D nature of the lift and drag coefficient data, refer to Howlett (ref. 7).

Blade aerodynamic shear forces, rotating-shaft frame— Let $F_{t_{is}}$, $F_{r_{is}}$, and $F_{p_{is}}$ be the tangential, radial, and perpendicular (normal) components of the elemental aerodynamic force at a given blade element (fig. 2(d)). Then the aerodynamic shear force may be written, in frame 1, as:

$$\vec{F}_{a1} = \begin{bmatrix} \cos \delta & \sin \delta & 0 \\ -\sin \delta & \cos \delta & 0 \\ 0 & 0 & 1 \end{bmatrix} \begin{Bmatrix} -\sum F_{t_{is}} \\ \sum F_{r_{is}} \\ -\sum F_{p_{is}} \end{Bmatrix} = \begin{Bmatrix} -F_t \cos \delta + F_r \sin \delta \\ F_t \sin \delta + F_r \cos \delta \\ -F_p \end{Bmatrix} \quad (38)$$

The aerodynamic shear at the flapping hinge, at the lead-lag hinge, and at the hub are identical. Therefore, the hub aerodynamic shear in the rotating-shaft frame, for one blade, may be written as:

$$\vec{F}_{ars} = \begin{bmatrix} 1 & 0 & 0 \\ 0 & \cos \beta & \sin \beta \\ 0 & -\sin \beta & \cos \beta \end{bmatrix} \begin{Bmatrix} -F_t \cos \delta + F_r \sin \delta \\ F_t \sin \delta + F_r \cos \delta \\ -F_p \end{Bmatrix} \quad (39)$$

or,

$$\begin{Bmatrix} F_{arsx} \\ F_{arsy} \\ F_{arsz} \end{Bmatrix} = \begin{Bmatrix} -F_t \cos \delta + F_r \sin \delta \\ F_t \sin \delta \cos \beta + F_r \cos \delta \cos \beta - F_p \sin \beta \\ -F_t \sin \delta \sin \beta - F_r \cos \delta \sin \beta - F_p \cos \beta \end{Bmatrix} \quad (40)$$

Blade aerodynamic shear forces, fixed-shaft frame— Rotating down to a fixed-shaft frame, we get:

$$\vec{F}_{afs} = \begin{bmatrix} \sin \psi & -\cos \psi & 0 \\ \cos \psi & \sin \psi & 0 \\ 0 & 0 & 1 \end{bmatrix} \begin{Bmatrix} F_{arsx} \\ F_{arsy} \\ F_{arsz} \end{Bmatrix} = \begin{Bmatrix} F_{arsx} \sin \psi - F_{arsy} \cos \psi \\ F_{arsx} \cos \psi + F_{arsy} \sin \psi \\ F_{arsz} \end{Bmatrix} \quad (41)$$

Blade aerodynamic moment about the lead-lag hinge, frame 1— The elemental aerodynamic force at each blade element, in frame-1, is:

$$\vec{F}_{a1_{is}} = \begin{bmatrix} \cos \delta & \sin \delta & 0 \\ -\sin \delta & \cos \delta & 0 \\ 0 & 0 & 1 \end{bmatrix} \begin{Bmatrix} -F_{t_{is}} \\ F_{r_{is}} \\ -F_{p_{is}} \end{Bmatrix} = \begin{Bmatrix} -F_{t_{is}} \cos \delta + F_{r_{is}} \sin \delta \\ F_{t_{is}} \sin \delta + F_{r_{is}} \cos \delta \\ -F_{p_{is}} \end{Bmatrix} \quad (42)$$

the elemental aerodynamic moment at the lead-lag hinge, in frame-1, may then be written as:

$$\vec{M}_{al1_{is}} = \begin{Bmatrix} r_{\delta_{is}} \sin \delta \\ r_{\delta_{is}} \cos \delta \\ 0 \end{Bmatrix} \times \begin{Bmatrix} -F_{t_{is}} \cos \delta + F_{r_{is}} \sin \delta \\ F_{t_{is}} \sin \delta + F_{r_{is}} \cos \delta \\ -F_{p_{is}} \end{Bmatrix} = \begin{Bmatrix} -r_{\delta_{is}} F_{p_{is}} \cos \delta \\ r_{\delta_{is}} F_{p_{is}} \sin \delta \\ r_{\delta_{is}} F_{t_{is}} \end{Bmatrix} \quad (43)$$

The blade aerodynamic moment about the lead-lag hinge may then be written as:

$$\vec{M}_{af1} = \begin{Bmatrix} \sum -r_{\delta_{is}} F_{p_{is}} \cos \delta \\ \sum r_{\delta_{is}} F_{p_{is}} \sin \delta \\ \sum r_{\delta_{is}} F_{t_{is}} \end{Bmatrix} \quad (44)$$

where the summation is over all the blade-elements.

Blade aerodynamic moment at the flapping hinge, frame 2– The aerodynamic moment about the flapping hinge consists of two parts: 1) moment due to the shear force at the lead-lag hinge, and 2) moment due to the non-lead-lag component of moment about the lead-lag hinge.

The moment due to aerodynamic shear force at the lead-lag hinge may be written, in frame 2, as:

$$\vec{M}_{af2_1} = \begin{Bmatrix} 0 \\ \Delta e \\ 0 \end{Bmatrix} \times \begin{Bmatrix} -F_t \cos \delta + F_r \sin \delta \\ F_t \sin \delta + F_r \cos \delta \\ -F_p \end{Bmatrix} = \begin{Bmatrix} -\Delta e F_p \\ 0 \\ \Delta e F_t \cos \delta - \Delta e F_r \sin \delta \end{Bmatrix} \quad (45)$$

The moment due to the non-lead-lag components of the moment about the lead-lag hinge may be written, in frame 2, as:

$$\vec{M}_{af2_2} = \begin{Bmatrix} \sum -r_{\delta_{is}} F_{p_{is}} \cos \delta \\ \sum r_{\delta_{is}} F_{p_{is}} \sin \delta \\ 0 \end{Bmatrix} \quad (46)$$

So, the total aerodynamic moment at the flapping hinge is:

$$\vec{M}_{af2} = \vec{M}_{af2_1} + \vec{M}_{af2_2} = \begin{Bmatrix} \sum -r_{\delta_{is}} F_{p_{is}} \cos \delta - \Delta e F_p \\ \sum r_{\delta_{is}} F_{p_{is}} \sin \delta \\ \Delta e F_t \cos \delta - \Delta e F_r \sin \delta \end{Bmatrix} \quad (47)$$

Blade aerodynamic hub moment, rotating-shaft frame– The aerodynamic hub moment consists of two parts, 1) the moment due to shear force at the flapping hinge, and 2) the moment due to the nonflapping moment at the flapping hinge.

The moment due to shear force at the flapping hinge may be written as:

$$\vec{M}_{ahrs_1} = \begin{Bmatrix} 0 \\ e_\beta \\ 0 \end{Bmatrix} \times \begin{Bmatrix} -F_t \cos \delta + F_r \sin \delta \\ F_t \sin \delta \cos \beta + F_r \cos \delta \cos \beta - F_p \sin \beta \\ -F_t \sin \delta \sin \beta - F_r \cos \delta \sin \beta - F_p \cos \beta \end{Bmatrix} \quad (48)$$

or,

$$\vec{M}_{ahrs_1} = \begin{Bmatrix} e_\beta (-F_t \sin \delta \sin \beta - F_r \cos \delta \sin \beta - F_p \cos \beta) \\ 0 \\ -e_\beta (-F_t \cos \delta + F_r \sin \delta) \end{Bmatrix} \quad (49)$$

The moment due to the nonflapping moment about the flapping hinge may be written as:

$$\vec{M}_{ahrs_2} = \begin{bmatrix} 1 & 0 & 0 \\ 0 & \cos \beta & \sin \beta \\ 0 & -\sin \beta & \cos \beta \end{bmatrix} \left\{ \begin{array}{c} 0 \\ \sum r_{\delta_{is}} F_{p_{is}} \sin \delta \\ \Delta e F_t \cos \delta - \Delta e F_r \sin \delta \end{array} \right\} \quad (50)$$

or

$$\vec{M}_{ahrs_2} = \left\{ \begin{array}{c} 0 \\ \cos \beta (\sum r_{\delta_{is}} F_{p_{is}} \sin \delta) + \sin \beta (\Delta e F_t \cos \delta - \Delta e F_r \sin \delta) \\ -\sin \beta (\sum r_{\delta_{is}} F_{p_{is}} \sin \delta) + \cos \beta (\Delta e F_t \cos \delta - \Delta e F_r \sin \delta) \end{array} \right\} \quad (51)$$

So, the aerodynamic hub moment in a rotating-shaft frame, for one blade, is:

$$\vec{M}_{ahrs} = \vec{M}_{ahrs_1} + \vec{M}_{ahrs_2} = \left\{ \begin{array}{c} M_{ahrs_x} \\ M_{ahrs_y} \\ M_{ahrs_z} \end{array} \right\} = \left\{ \begin{array}{c} e_\beta (-F_t \sin \delta \sin \beta - F_r \cos \delta \sin \beta - F_p \cos \beta) \\ \cos \beta (\sum r_\delta F_{p_{is}} \sin \delta) + \sin \beta (\Delta e F_t \cos \delta - \Delta e F_r \sin \delta) \\ -e_\beta (-F_t \cos \delta + F_r \sin \delta) + -\sin \beta (\sum r_\delta F_{p_{is}} \sin \delta) + \cos \beta (\Delta e F_t \cos \delta - \Delta e F_r \sin \delta) \end{array} \right\} \quad (52)$$

Rotating to a fixed-shaft frame, we have:

$$\left\{ \begin{array}{c} M_{ahfs_x} \\ M_{ahfs_y} \\ M_{ahfs_z} \end{array} \right\} = \begin{bmatrix} \sin \psi & -\cos \psi & 0 \\ \cos \psi & \sin \psi & 0 \\ 0 & 0 & 1 \end{bmatrix} \left\{ \begin{array}{c} M_{ahrs_x} \\ M_{ahrs_y} \\ M_{ahrs_z} \end{array} \right\} = \left\{ \begin{array}{c} M_{ahrs_x} \sin \psi - M_{ahrs_y} \cos \psi \\ M_{ahrs_x} \cos \psi + M_{ahrs_y} \sin \psi \\ M_{ahrs_z} \end{array} \right\} \quad (53)$$

Blade Restraint Terms

Both lead-lag and flapping spring and damping constraints are dealt with as proportional terms. Referring to figure 2(e), the lead-lag spring and damper exert a moment of:

$$\vec{M}_{rl1} = \left\{ \begin{array}{c} 0 \\ 0 \\ K_\delta \delta + K_\dot{\delta} \dot{\delta} \end{array} \right\} \quad (54)$$

on the blade. The lead-lag spring and damper and the flapping spring and damper together exert a moment of:

$$\vec{M}_{rf2} = \left\{ \begin{array}{c} K_\beta \beta + K_\dot{\beta} \dot{\beta} \\ 0 \\ -K_\delta \delta - K_\dot{\delta} \dot{\delta} \end{array} \right\} \quad (55)$$

on the blade segment between the flapping and the lead-lag hinges (Δe in fig. 2(e)) in frame 2, and a moment of:

$$\vec{M}_{rhfs} = \begin{bmatrix} \sin \psi & -\cos \psi \cos \beta & -\cos \psi \sin \beta \\ \cos \psi & \sin \psi \cos \beta & \sin \psi \sin \beta \\ 0 & -\sin \beta & \cos \beta \end{bmatrix} \begin{Bmatrix} -K_\beta \beta - K_{\dot{\beta}} \dot{\beta} \\ 0 \\ -K_\delta \delta - K_{\dot{\delta}} \dot{\delta} \end{Bmatrix} \quad (56)$$

or

$$\vec{M}_{rhfs} = \begin{Bmatrix} -(K_\beta \beta + K_{\dot{\beta}} \dot{\beta}) \sin \psi + (K_\delta \delta + K_{\dot{\delta}} \dot{\delta}) \cos \psi \sin \beta \\ -(K_\beta \beta + K_{\dot{\beta}} \dot{\beta}) \cos \psi - (K_\delta \delta + K_{\dot{\delta}} \dot{\delta}) \sin \psi \sin \beta \\ -(K_\delta \delta + K_{\dot{\delta}} \dot{\delta}) \cos \beta \end{Bmatrix} \quad (57)$$

on the hub in the fixed-shaft axes.

Lead-lag equation of motion– The lead-lag equation of motion is simply the solution of:

$$M_{il1z} + M_{al1z} + M_{rl1z} = 0 \quad (58)$$

for δ . This was done using MACSYMA with the “SIMPORG” macro (app. B) used for the factoring work. “SIMORG” basically takes the desired parts of the unsimplified equation from the initial stack and adds them to the final stack after performing algebraic and trigonometric simplifications (for more information refer to app. B). The resulting equation is given in appendix A.

Flapping equation of motion– The flapping equation of motion is simply the solution of:

$$M_{if2x} + M_{af2x} + M_{rf2x} = 0 \quad (59)$$

for β . This was also done using MACSYMA. The “SIMPORG” macro was again used for the factoring work, and the resulting equation is given in appendix A.

Upgrades to Other Modules

As in actual rotors, the total rotor outputs from the blade-element rotor module contain high frequency harmonics. Because of this harmonic variation, the original trim module supplied with FLYRT could not be used to trim the new model. The original trim module was designed to calculate the variation matrix only once and then use it throughout the trim procedure. A routine which would recalculate this matrix at every step was needed instead. Also, the original equations-of-motion module had to be modified to allow the averaging necessary to remove the harmonics of the forces and moments generated by the blade-element rotor module.

A new trim module, based on the IMSL (ref. 13) subroutine ZXSSQ but following the general setup of the original FLYRT trim module, was therefore developed. Also, the equations-of-motion module was upgraded to provide the needed averaging during trim. The combination of the new trim and equations-of-motion routines were shown to be satisfactory for trimming BEMAP throughout the flight envelope.

Further modifications of the equations-of-motion module were also necessary. In the map-type rotor module inertial effects are not taken into account explicitly. Instead, the polar moment of inertia

of the rotor is lumped with the other inertias in the equations-of-motion module. By contrast, the blade-element module explicitly accounts for the inertial forces and moments at the rotor. Therefore, the equations-of-motion module had to be modified to account for this difference. In effect, the rotor polar moment of inertia was replaced with the hub polar moment of inertia and the rotor inertias were accounted for explicitly at the rotor module itself.

Apache Flight Data

During the summer of 1990, an instrumented AH-64A Apache helicopter was used to perform a series of tests to collect data specifically for model validation purposes. The tests were conducted at the U.S. Army's Airworthiness Qualification Test Directorate (AQTD) at Edwards Air Force Base in California, and were part of a broader effort (ref. 14) aimed at validating the new Handling Qualities Requirements for Military Rotorcraft (ADS-33C) (ref. 15). This database represents the best available source of flight-data for the AH-64A Apache. The only major shortcoming of the data is the fact that the helicopter used for the tests did not have an instrumented rotor and therefore rotor data were not collected.

Both static and dynamic validation data were collected. Static (or trim) validation data were collected for various flight conditions from hover to 129 kts forward airspeed, several side-ward and rear-ward speeds, and a steady climb condition. In addition, some of the forward flight data were collected at two different aircraft C.G. positions to allow analysis of the effects of C.G. location on aircraft response. To collect trim data at each flight condition, the aircraft was flown to a stable trim at the desired flight condition and about 10 sec of data were collected at the trim state before moving on to the next run.

The dynamic validation data consisted of doublets and frequency sweeps in all four control axes at hover, 60 and 120 kts forward airspeed. Data were collected with both DASE on and off. In order to reduce the effects of winds and gusts on the recorded responses, the flights were conducted in conditions of near zero winds.

BEMAP Validation

BEMAP was extensively validated by comparing its responses with the flight data described above. The validation effort spanned both hover and forward flight and was conducted in both time and frequency domains. Some of the results of the validation work are presented below.

Trim Validation

The trim checks were conducted by setting up the model to match, as closely as possible, the configuration and flight condition of the available flight data. This included the use of flight-test values of aircraft weight, C.G. location, ambient temperature/density, and altitude. It's usual practice to trim models at zero sideslip for low-speed flight and at zero-roll angle for high speed. Since the longitudinal and lateral components of the aircraft airspeed were available, however, it was decided to trim the model on roll angle at all speeds and treat sideslip angle as a fixed trim parameter. Therefore, four controls and two attitudes (pitch and roll) were used to trim the model in all cases. As discussed earlier a new trimming algorithm was developed to trim the new blade-element rotor. Using this routine, and

a simple averaging scheme in the equations-of-motion module (only during trim), it was possible to zero out the net forces and moments on the aircraft even with the harmonic nature of the rotor forces and moments.

The checks were run for hover, 10, 20, 30, 40, 60, 80, 100, 120, and 129 kts and the results are shown in figures 3(a-g). As may be seen, the model trim values match flight data quite well. The differences are seen to be less than 10 percent in most cases. The largest variations are in the 20-40 kts range which expands the transitional lift region where inflow modeling is less accurate.

Figure 3(a) compares the predicted trim pitch attitude (both BEMAP and FLYRT) with flight data. The match between BEMAP and flight data is quite good close to hover and at high speed (>80 kts). Between 20 and 80 kts, however, the model first over and then under predicts the trim pitch attitude. The largest variation occurs at 40 kts where BEMAP underpredicts the actual pitch angle by about 2.9 deg. Everywhere else the variation is significantly smaller than this maximum.

Figure 3(b) compares the predicted collective input required to trim with the flight values. BEMAP predicts the general trend of the collective variation with airspeed quite well. The model, however, consistently underpredicts the required collective by up to 10 percent. The variation is the largest at hover and high speed and is on average lower between 20 and 80 kts. The reason for this discrepancy at hover may be the simplified treatment of the rotor/fuselage interaction incorporated into the fuselage model. The effect of the rotor downwash on the fuselage does not seem to be accounted for in a satisfactory manner, underpredicting the downforce on the fuselage. Note, that FLYRT does a slightly better job of predicting the collective input required to trim.

Figure 3(c) compares the predicted longitudinal cyclic input to trim with the corresponding flight values. BEMAP is seen to duplicate the general trend in the migration of the longitudinal cyclic with airspeed quite well. The match is seen to be excellent below 20 kts (less than 1 percent difference) and quite good above 60 kts (around 3 percent or less). In the middle speeds (transitional lift region), however, the model overpredicts the longitudinal cyclic required to trim by up to 8 percent at one point.

Figure 3(d) compares the predicted roll attitude with the actual flight values. The general trend of the roll angle variation with airspeed is duplicated very well. BEMAP slightly underpredicts the roll angle (by less than 1 deg) close to hover and then overpredicts it by a maximum of about 1 deg between 30 and 120 kts.

Figure 3(e) compares the lateral cyclic required for trim with the flight values. Again, the general trend in the migration of the lateral cyclic with airspeed is duplicated quite well. Below 30 kts, BEMAP underpredicts the lateral cyclic required to trim by 1-2 percent. Above 30 kts, the model consistently overpredicts the lateral cyclic requirement by around 2 percent all the way to 120 kts. Overall, BEMAP results are seen to be closer to the flight values than FLYRT.

Figure 3(f) compares the modeled pedal requirement for trim with flight data. It can be seen that the general variation with airspeed is not duplicated as well as it was for the other trim parameters. The difference between predicted and actual values, however, never exceeds 14 percent and is less than 10 percent in most cases. The inadequate treatment of the effects of main-rotor downwash on the tail rotor is thought to be the cause of this discrepancy.

Finally, figure 3(g) shows the variation of the horizontal stabilator incidence angle with airspeed and shows that the model predicts the incidence angle quite well throughout. This indicates that an error in the horizontal stabilator angle is not responsible for the trim pitch attitude discrepancies between 20 and 80 kts. This however, does not mean that the horizontal stabilator is not the cause since the main rotor to horizontal tail interference effect, and not the angle, may be the source of the errors.

Time Domain Validation

Similar to trim, the time-domain validations were conducted by setting up the model to match, as closely as possible, the configuration and flight conditions of the available flight data. This included the use of flight-test values of aircraft weight, C.G. location, ambient temperature/density, and altitude. No information, however, was available concerning moments and products of inertia of the test aircraft. Therefore, best estimates based on values given in the FLYRT documentation and related AH-64A work for an AH-64A helicopter configured similar to the test aircraft were used (table 1).

Actual pilot-control inputs were used to drive the model in all cases. To avoid the initial abrupt control changes that would have been encountered due to mismatches in trim, the actual pilot controls were first converted to difference values. This simply consisted of subtracting the initial trim-control values from the control values at all subsequent times. These difference values were then added to the trim values of the controls calculated by the model. As a result, the lines depicting the model control inputs in all the plots presented in this section are parallel to the lines depicting the flight-test values. The bias between the two lines is an indication of how close the model trim values were to the actual flight-data values at the initiation of the data run.

The flight data used for hover were collected with the DASE turned off whereas the flight data used for forward flight were collected with the DASE on. Since the validation of the airframe model was the only objective, control inputs were injected at the main- and tail-rotor swashplates for all maneuvers. This, in effect, bypassed the DASE module and prevented any DASE module errors from affecting the results of the comparisons. Note, however, that in the absence of the stabilizing effects of the DASE the model diverges much more rapidly. This point is explored later in this report.

The test data were used as received from AEFA and no attempt was made to correct or remove instrument biases or recording errors. For each maneuver, control inputs in all four axes, angular rates, rotor rpm, body-axis velocities, normal acceleration, and horizontal stabilator incidence angle are shown and compared to flight data (in some cases engine torque is shown instead of stabilator incidence angle to help explain discrepancies). Note, that this large amount of data is provided for completeness and therefore not every plot is explicitly referred to in the following discussions.

Hover

Four maneuvers, a doublet in each control axis, were considered. The aircraft configuration data for the four maneuvers are presented in table 2. All the maneuvers were characterized by the pilot input in the main control being much larger than his inputs in the other three controls. Nevertheless, all the inputs were fed into the model to insure as close a match to the actual maneuver as possible.

In most cases, there is some small control activity in all the axes prior to the start of the maneuver. These were most likely made by the pilot to maintain or tighten the trim condition as the helicopter continually tends to depart from trim. Also, in some cases the initial rates at the beginning of the data are not zero and the pilot may have attempted to correct them using appropriate inputs prior to the actual initiation of the maneuver. Since the model rates are hard-zeros at trim, such corrective inputs can cause the model to diverge from the flight data even before the maneuver actually begins. This effect is especially pronounced at hover. To overcome this problem to some extent, a provision was added to allow the introduction of inputs to be delayed until a specific time after the start of the data (start of data is time = 0.0). The criterion for the selection of the modified start time was set to be the occurrence of zero rates (or as close to it as possible) in the flight data. In other words, the flight data for each maneuver were scanned and a time (prior to the beginning of the maneuver) was selected when all the angular rates were jointly as close to zero as possible. This time was then used as the start of pilot-input control of the model, the inputs being left at the trim values until then. As a consequence of this modification, the control input traces for the model are flat and do not follow the flight data between time = 0.0 and the modified start time. This modification was only used in hover.

Finally, due to control freeplay in the actual aircraft, small inputs sometimes produced no flight-test response. Because there is no modeling of control freeplay, simulation responses may be expected to be faster with greater magnitude. A similar situation was noted by Ballin in his UH-60 modeling work (ref. 3).

Lateral response— Figures 4(a-c) compare the responses of BEMAP with flight data for a left-right lateral doublet. The pilot inputs are depicted in figure 4(a). There is significant control activity prior to the start of the maneuver itself. These are especially noticeable in the lateral-cyclic and pedals. As discussed above, to prevent these extraneous inputs from affecting the match, the pilot-control-input injection into the model was delayed, in this case to time = 2.8 sec. Overall, BEMAP predicts the trim controls quite well in all axes except collective. As mentioned in the trim validation section, the main reason for the discrepancy in collective is thought to be insufficient modeling of the effects of rotor downwash impingement on the fuselage. Figure 4(b) shows that the roll-rate response of the aircraft is duplicated quite correctly by BEMAP. The yaw-rate response is also duplicated quite well and the rotor rpm variation has the same character as the flight-test results. The pitch-rate response, however, initially goes the wrong way. The problem of predicting the pitch-to-roll and roll-to-pitch coupling responses will be discussed further, later in the report. Figure 4(c) shows that the components of body velocity are duplicated well initially. Finally, it seems that the incidence angle of the horizontal stabilator is overestimated by the model. However, according to the ADS-10 document for the Apache (ref. 10), the horizontal stabilator should be at 25 deg in this flight condition. The reason for the lower flight data value is therefore not known.

Longitudinal response— Figures 5(a-c) compare the responses of BEMAP with flight data for a forward-aft longitudinal doublet. Figure 5(a) shows that even though only longitudinal cyclic inputs were intended, there is significant activity in the lateral axes. Again, the model predicts the controls required to trim quite well except for collective. Note, that the injection of pilot-control into the model starts at time = 1.0 sec. Figure 5(b) shows that the on-axis pitch rate is modeled quite well for the first part of the doublet. The match deteriorates, however, for the second part of the doublet. The off-axis roll response rate initially goes the wrong way in much the same way as the off-axis pitch response did in the lateral doublet case, suggesting a symmetry in the off-axis response error in hover. From figure 5(c) it may be seen that BEMAP predicts the normal acceleration well. Also, the variations in

the body lateral and longitudinal velocities are duplicated reasonably well initially. However, variations of the modeled horizontal tail incidence angle do not follow the flight data. Note, that the flight values of the horizontal tail incidence angle seem to exceed the 25 deg limit, implying a possible measurement error.

Directional response— Comparisons of the responses of BEMAP with flight data for a left-right directional doublet are shown in figures 6(a-c). As may be seen from figure 6(a), pilot-input injection into the model does not occur until time = 2 sec. Figure 6(b) shows that yaw-rate response and rotor rpm variations are duplicated reasonably well. Also, BEMAP duplicates the aircraft roll rate reasonably well up to the second part of the doublet (9 sec). Finally, the pitch-rate response seems to follow the general trends of the actual response, with BEMAP and FLYRT responses being very similar. Figure 6(c) shows that the lateral translational velocity variation predicted by the model is significantly larger than the actual variation. The reason for this is probably the higher positive roll rate predicted by the model between 4 and 7 sec and the resulting higher roll attitudes.

Heave response— Figures 7(a-c) compare BEMAP responses with flight data for an up-down collective doublet. Figure 7(a) depicts the control inputs for the maneuver. As may be seen from figure 7(b), all the model angular rate characteristics are similar to the flight data for the first 8-9 sec of the maneuver. The modeled rotor rpm response, however, shows significant discrepancy. The main reason for this error is the engine torque response, as depicted in figure 7(c). As may be seen, the engine response, as triggered by the collective input, is so fast that the model rotor not only does not droop, it actually overspeeds. No attempt, however, was made to modify the 701 engine module provided with FLYRT. Finally, figure 7(c) also shows that the model duplicates the normal acceleration response reasonably well, indicating proper implementation of the Pitt/Peters inflow model.

60 kts

Four maneuvers, a doublet in each control axis, were considered. The aircraft configuration data for the four maneuvers are presented in table 3. Again, all the maneuvers were characterized by the pilot input in the main control being much larger than his inputs in the other three controls. Nevertheless, all the inputs were fed into the model to insure as close a match to the actual maneuver as possible.

Lateral response— Comparisons of BEMAP responses with flight data for a right-left lateral doublet at 60 kts are presented in figures 8(a-c). The pilot control inputs are shown in figure 8(a). As noted in the trim validation section, the pedal input required to trim is underpredicted by BEMAP. Identical results were obtained using FLYRT. The angular rate and rotor rpm responses are shown in figure 8(b). BEMAP predicts the roll-rate response very well for the first half of the doublet, but underpredicts the roll-rate magnitude during the second half. BEMAP also predicts the yaw-rate response quite well for the first 6 sec of the maneuver. The predicted pitch-rate response, however, is significantly in error. Note, that the discrepancy is quite similar to the discrepancy noted in hover for the lateral doublet maneuver. Finally, BEMAP predicts the general trend of rotor rpm variation quite well, though the magnitude of the response is underpredicted. Figure 8(c) compares BEMAP's longitudinal and lateral components of body velocity, and normal acceleration with flight data and also shows the position of the horizontal stabilator throughout the maneuver. The longitudinal velocity compares well with the flight data. The predicted lateral-velocity response is somewhat different than flight, however, and the maximum lateral velocity encountered is slightly higher. Also, BEMAP does not predict the variation of the normal acceleration very well for this maneuver. Finally, the model

predicts the initial incidence angle of the horizontal stabilator within 1 deg. The match worsens with time, but it's probably because the model, as a whole, is diverging from flight data.

Longitudinal response— Figures 9(a–c) depict the validation results for a forward-aft longitudinal doublet at 60 kts. The control inputs are shown in figure 9(a). Figure 9(b) shows that the on-axis pitch-rate response is predicted quite well. Also, BEMAP seems to predict the general shape of the off-axis roll-rate response quite well. This is interesting since BEMAP's prediction of the off-axis pitch-rate response to a roll doublet at 60 kts seemed to go the wrong way. Also, this is different than hover where the results showed a symmetry in the off-axes responses, by both being in error in a similar way. Figure 9(b) also shows that yaw coupling to pitch is not predicted well. Further, there is a discrepancy in the rotor rpm response even though the engine response is modeled fairly well, as shown in figure 9(c). Finally, figure 9(c) also shows that the general shape of the normal acceleration response is duplicated well.

Directional response— Figures 10(a–c) compare the responses of BEMAP with flight-test results for a left-right directional doublet. Figure 10(a) shows the control inputs for the maneuver. Figure 10(b) indicates that the on axes yaw-rate response is modeled quite well throughout the maneuver. Also, the roll rate is matched quite well for the majority of the time. The pitch rate, however, is not predicted well. Figure 10(c) shows that the longitudinal component of body velocity remains fairly flat and this characteristic is modeled well. The variation of the lateral component of body velocity is also modeled well in magnitude, but there seems to be a significant delay in its actual buildup which is not duplicated well. Finally, the error seen in the normal acceleration is likely caused by the error in the pitch rate.

Heave response— Figures 11(a–c) present comparisons of BEMAP responses with flight data for an up-down collective doublet. Figure 11(a) shows the control inputs for the maneuver. Figure 11(b) shows that all angular rates are predicted reasonably well. The rotor rpm variation, however, shows significant discrepancy. A look at figure 11(c) shows that the reason for this discrepancy, as in the hover collective doublet case, is the engine response. As may be seen, the engine-torque response as triggered by the collective input is so fast that the modeled rotor not only does not droop, it actually overspeeds. Finally, figure 11(c) shows that the normal acceleration is duplicated quite well, indicating that the dynamic inflow model seems to be valid.

120 kts

In general, BEMAP responses at 120 kts are not as good as those in hover and 60 kts. This is likely because at 120 kts the aerodynamic theory used for the rotor-blade-segment aerodynamics begins to be inadequate. Effects such as reverse flow and compressibility become more pronounced at these high speeds. Since such effects are not accounted for rigorously (or not at all in the case of compressibility) in the model, the model's ability to predict the aircraft responses deteriorates. Again, four maneuvers, a doublet in each control axes, were considered. The aircraft configuration data for the four maneuvers are presented in table 4.

Lateral response— Figures 12(a–c) show the results of comparing BEMAP responses with flight data at 120 kts for a right-left lateral doublet. Figure 12(a) shows that all the controls required to trim are predicted reasonably well except for collective. Interestingly, the discrepancy in collective seems quite similar to what was observed in the hover cases. In the 120 kts case, however, the rotor downwash impingement on the fuselage cannot be the cause of the discrepancy because the skew angle is quite

large. Figure 12(b) shows that the initial roll-rate response is duplicated quite well by the model, but it underpredicts the magnitude of the response to the second part of the doublet. Also, as in the hover cases, the pitch-rate response to a lateral input is not modeled well, and initially goes in the opposite direction. Figure 12(c) shows that neither BEMAP nor FLYRT seem to be very accurate in predicting the lateral and longitudinal components of body velocity, or the variation of the normal acceleration.

Longitudinal response— Figures 13(a–c) compare the responses of BEMAP with flight data for a forward-aft longitudinal doublet at 120 kts. The control inputs are shown in figure 13(a). Figure 13(b) shows the on-axis pitch response to be duplicated quite well. More interestingly, the initial off-axis roll-rate response of the model seems to follow the general trend of the actual response. Specifically, the response does not seem to go in the opposite direction, as it does in the case of the off-axis pitch response to a roll input. Since the same kind of results were noted at 60 kts, this further suggests that there is some asymmetry in the ability to duplicate the two off-axes responses in forward flight. This asymmetry might provide some clues as to the cause of the discrepancies and why none of the current models are capable of duplicating the off-axis response (as discussed in ref. 2).

Directional response— Figures 14(a–c) show BEMAP responses to a directional doublet at 120 kts. The pilot controls are shown in figure 14(a). Figure 14(b) indicates that the BEMAP yaw-rate response duplicates flight quite well. BEMAP pitch and roll rates, however, show significant discrepancy. Note, that FLYRT does a better job matching the flight-roll rate. Finally, figure 14(c) shows that both models fall short of matching either the velocity components or the normal acceleration observed in flight.

Heave response— Figures 15(a–c) depict BEMAP responses to a collective doublet at 120 kts. Pilot inputs are shown in figure 15(a). Figure 15(b) shows that BEMAP duplicates the general trends of the angular-rate responses of the aircraft. Again, however, the fast engine-module response to collective causes the model rpm responses to be incorrect. Finally, as figure 15(c) shows, BEMAP fails to match the lateral component of velocity observed in flight.

Effects of Bypassing the DASE Model

As mentioned earlier, in the absence of the stabilizing effects of the DASE the model diverges much more rapidly. Introducing pilot inputs at the swashplate, as was done here to concentrate on the airframe model validation, in effect removes the stabilizing effects of the modeled DASE. Moreover, since the test aircraft's DASE could have been responding to conditions not duplicated by the simulation, significant discrepancies could result. To demonstrate this effect, the lateral maneuver at 120 kts discussed previously with pilot inputs introduced at the swashplate was repeated with the modeled DASE turned on and pilot inputs introduced at the stick. The results are shown in figure 16. As may be seen, the new results show significant improvement over the original run in the on-axis. The roll-rate response is seen to match the flight data much better, especially for the second half of the doublet. As expected, the effect of feedback is to mask errors at low frequencies. Therefore, leaving the DASE model on and introducing pilot inputs at the stick for all the runs would have led to much closer results. However, it would have masked errors in the airframe modeling which need to be identified and addressed.

Frequency Domain Validation

Flight-data-based frequency responses for hover were already available from Schroeder et. al. (ref. 1). Frequency responses for forward flight, however, were not available and had to be generated as part of the BEMAP validation effort. As in reference 1, CIPHER^R was used along with frequency sweep data collected at AEFA (discussed earlier) to generate the frequency responses. Briefly, the process was as follows:

1. All available forward-flight-sweep data were processed through FRESPID and MISOSA using a single representative window size. FRESPID is a CIPHER^R subprogram which uses the chirp-z transform (an advanced fast-fourier transform algorithm) and overlapping hanning windows (used to provide low spectral variance through averaging) to calculate magnitude, phase, and coherence data from frequency sweep time histories. MISOSA is another CIPHER^R subprogram which processes FRESPID results to remove the corrupting effects of correlated inputs in the off-axis controls. In effect, the output of MISOSA consists of "conditioned" frequency responses that represent the relationship of the output to the input with the contribution of all other inputs removed.

This preliminary processing was performed to insure that the highest possible coherence could be achieved in the final-frequency response pairs.

2. For each axis, the two/three best runs were selected (based on the coherence plots obtained from MISOSA in step 1), concatenated, and reprocessed through FRESPID using five windows. The windows used were 10, 20, 30, 35, and 40 sec long and were sized to provide the best combination of low-frequency coverage and maximized spectral averaging.
3. The results of step 2 were then processed through MISOSA to eliminate the contaminating effects of correlated off-axis inputs.
4. Finally, the results of step 3 were processed through COMPOSITE, which is the CIPHER^R subprogram used to optimize the data obtained using various window sizes.

Only DASE-off data were used for all the frequency-domain comparisons. In the absence of stability augmentation the pilot often has to use significant off-axis control inputs in order to maintain safe flying attitudes during the sweep. Consequently, the coherence of the frequency response pairs are poor in some cases, especially in the off-axis responses.

Ideally, it would have been preferable to drive the model with the same frequency-sweep inputs and process the model responses through CIPHER^R to generate frequency response pairs (magnitude and phase plots). However, since the open-loop model is unstable and would diverge long before the 90 sec duration of a typical sweep, running frequency sweeps through the model would have required additional effort to introduce additional stability loops as in reference 3. Instead, a simple numerical linearization technique was used to generate linear state-space models which could then be compared with the flight data. The stability derivative generation routine delivered with FLYRT was modified for this task. In particular, it was modified to perform a two-sided linearization to provide more accurate results, i.e., each derivative was calculated as:

$$\left. \frac{\delta y}{\delta x} \right|_{x=x_0} = \frac{y(x_0 + \Delta x) - y(x_0 - \Delta x)}{2\Delta x} \quad (60)$$

Hover

Preliminary hover results were briefly documented in reference 16 and are expanded upon here. As in reference 16, the identified time delays from reference 1 were used with BEMAP 6-DOF results to partially compensate for the limitations of 6-DOF analysis. Table 5(a) provides a comparison of the stability derivatives identified by Schroeder et. al. (ref. 1) with the derivatives obtained from BEMAP. As may be seen, there is general agreement between the model and the identified on-axis rotational-stability derivatives. The pitch to roll (M_p) and roll to pitch (L_q) off-axis derivatives, however, do not agree with the flight-identified values. In fact, the BEMAP-based values for both M_p and L_q are of the same magnitude but opposite sign compared to the identified values. This is not surprising considering the time domain comparisons discussed earlier.

Moving to control derivatives, examination of the results in table 5(b) shows good agreement for the on-axis rotational pitch (M_{lon}), roll (L_{lat}), and yaw (N_{ped}) control derivatives. The on-axis translational longitudinal (X_{lon}), lateral (Y_{lat}), and heave (Z_{col}) control derivatives also show general agreement with the flight values.

The closeness of the match between BEMAP responses and flight data can be better seen by comparing the actual frequency response pairs instead of derivative values. These are shown in figures 17(a-d). In figure 17(a), BEMAP roll-rate and lateral-velocity responses are compared with flight data. As can be seen, BEMAP responses match the flight data quite well, especially in the frequency range between 0.8 and 7 rad/sec. Furthermore, BEMAP responses show slight improvement over FLYRT for both cases. Figure 17(b) compares BEMAP's pitch-rate and longitudinal-velocity responses with flight data. Again, the figure shows that the responses are quite close. The coherence of the pitch-rate response results is quite good and the match is seen to be good in a wider frequency range (0.5-10 rad/sec) compared to roll. However, the unsatisfactory coherence of the longitudinal velocity results at very low frequencies (less than 0.5 rad/sec) makes them unreliable. Figure 17(c) compares BEMAP yaw rate and heave velocity responses with flight data. The responses again compare favorably and BEMAP and FLYRT seem to be identical in high frequencies (this should be expected since BEMAP uses the same tail-rotor module). At low frequencies, however, FLYRT seems to do better in predicting the yaw-rate response. Finally, figure 17(d) depicts the poor match between BEMAP off-axes responses and flight data and shows that FLYRT responses are the same way. Note, that the match in magnitude is significantly better than the match in phase, which reflects the time domain effect of magnitude matching but with wrong phasing (opposite), and the derivatives M_p and L_q having the correct magnitude but the wrong sign.

60 kts

Tables 5(a-b) provide the stability and control derivatives obtained from BEMAP and FLYRT at 60 kts. Since state-space models based on flight data were not identified in forward flight, the model derivatives can not be evaluated and are only provided for completeness. The quality of the BEMAP responses can, however, be evaluated by comparing Bode plots of the responses of a BEMAP-based 6-DOF linear model (the same identified time delays used in hover were used here due to a lack of more appropriate values) with frequency response pairs obtained from flight data. Figures 18(a-c) show such a comparison. Figure 18(a) shows the roll- and pitch-rate responses to lateral and longitudinal inputs respectively. As may be seen, BEMAP does quite well in predicting the roll-rate response and significantly improves on FLYRT. The two models both match the pitch-rate data reasonably well. Figure 18(b) shows that BEMAP provides noticeable improvement over FLYRT in predicting

the yaw-rate response to pedals. Both models, however, have difficulty predicting the vertical-velocity response to a collective input. Finally, figure 18(c) corroborates the results obtained in the time domain regarding the asymmetry of the off-axis prediction in forward flight. As may be seen, BEMAP does fairly well in predicting the off-axis roll-to-pitch response at frequencies above 0.7 rad/sec, showing noticeable improvement over FLYRT. It still, however, does poorly in predicting the pitch response to a lateral input, as does FLYRT.

120 kts

The frequency response pairs generated from the 120 kts flight data had the lowest overall coherence of all the data. As a result only the on-axes responses had sufficient coherence to provide reasonable reliability. Therefore, only on-axes responses are presented here. Table 6(a-b) present the 6-DOF-stability derivatives from BEMAP and FLYRT. As in the 60 kts case, flight-identified state-space models were not available, so the derivatives can not be compared to flight data. They are, nevertheless, presented for completeness. Also, the hover flight-identified time delays were again used due to a lack of more appropriate values. Figure 19(a) depicts the on-axes lateral and longitudinal responses. As may be seen, BEMAP does quite well in both cases and shows improvement over FLYRT. Figure 19(b) depicts the on-axes directional and heave responses. Again, BEMAP responses are seen to match the flight data reasonably well and to show improvement over FLYRT.

Concluding Remarks

A blade-element mathematical model for the AH-64A Apache Advanced Attack Helicopter (BEMAP) has been developed by the Aeroflightdynamics Directorate of the U.S. Army ATCOM. BEMAP is based on the MDHS FLYRT model of the AH-64A, but incorporates a blade-element approach in its main-rotor module. This approach treats the aerodynamic and especially the inertial forces and moments more rigorously and removes the dependency on pregenerated maps inherent in the original FLYRT main-rotor module.

Results of the BEMAP validation effort described in this report indicate that:

1. Responses compare favorably with FLYRT, indicating that the blade-element rotor module has been derived and implemented correctly.
2. On-axis responses match hover and forward-flight flight data well as indicated by the time and frequency domain comparisons.
3. Off-axes results match flight data poorly at hover for both pitch-to-roll and roll-to-pitch responses. This may be seen in both time and frequency domains and by comparing the off-axes stability derivatives with those identified from flight.
4. Off-axes correlation results for forward flight are mixed. The aircraft's roll response to a pitch input is predicted fairly well whereas the pitch response to a roll input is not. This difference can be seen in both the time and the frequency domain results.

Improvements in our AH-64A simulation capability, including a solution to the off-axes discrepancies, can now be attempted by including enhanced aerodynamics and explicit treatment of compressibility, blade stall, and reverse flow in the blade-element rotor module.

Appendix A



Blade-element velocity vector in rotating-shaft frame

$$V_{rsx} =$$

$$\begin{aligned} & \text{COS(PSI) VHFS} + \text{SIN(PSI) UHFS} + (\text{COS(BETA)} (\text{COS(DELTA) RDELTA} + \text{DELE}) \\ & + \text{EBETA}) (\text{OMG} - \text{RFS}) - \text{SIN(BETA)} (\text{SIN(PSI) QFS} - \text{PFS COS(PSI)}) \\ & (\text{COS(DELTA) RDELTA} + \text{DELE}) + \text{COS(DELTA)} \frac{\text{dDELTA}}{\text{dT}} \text{RDELTA} \end{aligned}$$

$$V_{rsy} =$$

$$\begin{aligned} & \text{SIN(PSI) VHFS} - \text{COS(PSI) UHFS} + \text{SIN(DELTA) RDELTA} (\text{RFS} - \text{OMG}) \\ & - \text{SIN(BETA)} (-\text{COS(PSI) QFS} - \text{PFS SIN(PSI)}) (\text{COS(DELTA) RDELTA} + \text{DELE}) \\ & - \text{SIN(BETA)} \frac{\text{dBETA}}{\text{dT}} (\text{COS(DELTA) RDELTA} + \text{DELE}) \\ & - \text{COS(BETA) SIN(DELTA)} \frac{\text{dDELTA}}{\text{dT}} \text{RDELTA} \end{aligned}$$

$$V_{rsz} =$$

$$\begin{aligned} & \text{WHFS} + (\text{COS(PSI) QFS} + \text{PFS SIN(PSI)}) \\ & (\text{COS(BETA)} (\text{COS(DELTA) RDELTA} + \text{DELE}) + \text{EBETA}) \\ & - \text{COS(BETA)} \frac{\text{dBETA}}{\text{dT}} (\text{COS(DELTA) RDELTA} + \text{DELE}) \\ & + \text{SIN(DELTA)} (\text{PFS COS(PSI)} - \text{SIN(PSI) QFS}) \text{RDELTA} \\ & + \text{SIN(BETA) SIN(DELTA)} \frac{\text{dDELTA}}{\text{dT}} \text{RDELTA} \end{aligned}$$

Blade-element acceleration vector in rotating-shaft frame

$$a_{rsx} =$$

$$(\text{COS(BETA)} (\text{COS(DELTA) RDELTA} + \text{DELE}) + \text{EBETA}) \left(\frac{\text{dOMG}}{\text{dT}} - \frac{\text{dRFS}}{\text{dT}} \right)$$

$$\begin{aligned}
& + (\text{OMG} - \text{RFS}) (\text{SIN}(\text{DELTA}) \text{RDELTA} (\text{RFS} - \text{OMG})) \\
& - \text{SIN}(\text{BETA}) (- \text{COS}(\text{PSI}) \text{QFS} - \text{PFS} \text{SIN}(\text{PSI})) (\text{COS}(\text{DELTA}) \text{RDELTA} + \text{DELE}) \\
& + 2 \left((- \text{SIN}(\text{BETA}) \frac{d\text{BETA}}{dT} (\text{COS}(\text{DELTA}) \text{RDELTA} + \text{DELE}) \right. \\
& \quad \left. - \text{COS}(\text{BETA}) \text{SIN}(\text{DELTA}) \frac{d\text{DELTA}}{dT} \text{RDELTA} (\text{OMG} - \text{RFS}) \right. \\
& \quad \left. + (\text{SIN}(\text{PSI}) \text{QFS} - \text{PFS} \text{COS}(\text{PSI})) (\text{SIN}(\text{BETA}) \text{SIN}(\text{DELTA}) \frac{d\text{DELTA}}{dT} \text{RDELTA} \right. \\
& \quad \left. - \text{COS}(\text{BETA}) \frac{d\text{BETA}}{dT} (\text{COS}(\text{DELTA}) \text{RDELTA} + \text{DELE})) \right) \\
& + (\text{SIN}(\text{PSI}) \text{QFS} - \text{PFS} \text{COS}(\text{PSI})) ((\text{COS}(\text{PSI}) \text{QFS} + \text{PFS} \text{SIN}(\text{PSI})) \\
& (\text{COS}(\text{BETA}) (\text{COS}(\text{DELTA}) \text{RDELTA} + \text{DELE}) + \text{EBETA}) \\
& + \text{SIN}(\text{DELTA}) (\text{PFS} \text{COS}(\text{PSI}) - \text{SIN}(\text{PSI}) \text{QFS}) \text{RDELTA}) \\
& - \text{SIN}(\text{BETA}) (\text{SIN}(\text{PSI}) \frac{d\text{QFS}}{dT} + \text{COS}(\text{PSI}) \frac{d\text{PSI}}{dT} \text{QFS} + \text{PFS} \text{SIN}(\text{PSI}) \frac{d\text{PSI}}{dT} \\
& \quad - \text{COS}(\text{PSI})) (\text{COS}(\text{DELTA}) \text{RDELTA} + \text{DELE}) + \text{COS}(\text{DELTA}) \frac{d\text{DELTA}^2}{dT^2} \text{RDELTA} \\
& - \text{SIN}(\text{DELTA}) \left(\frac{d\text{DELTA}^2}{dT^2} \text{RDELTA} + \text{AHFSX} \text{SIN}(\text{PSI}) + \text{AHFSY} \text{COS}(\text{PSI}) \right)
\end{aligned}$$

$a_{rsy} =$

$$\begin{aligned}
& \text{SIN}(\text{DELTA}) \text{RDELTA} \left(\frac{d\text{RFS}}{dT} - \frac{d\text{OMG}}{dT} \right) + 2 \\
& (\text{COS}(\text{DELTA}) \frac{d\text{DELTA}}{dT} \text{RDELTA} (\text{RFS} - \text{OMG}) + (- \text{COS}(\text{PSI}) \text{QFS} - \text{PFS} \text{SIN}(\text{PSI})) \\
& \quad \frac{d\text{DELTA}}{dT} \text{RDELTA} \quad \frac{d\text{BETA}}{dT}
\end{aligned}$$

$$\begin{aligned}
& (\text{SIN}(\text{BETA}) \text{ SIN}(\text{DELTA}) \frac{\text{-----}}{\text{dT}} \text{RDELTA} - \text{COS}(\text{BETA}) \frac{\text{-----}}{\text{dT}} \\
& (\text{COS}(\text{DELTA}) \text{RDELTA} + \text{DELE})) + ((\text{COS}(\text{BETA}) (\text{COS}(\text{DELTA}) \text{RDELTA} + \text{DELE}) + \text{EBETA}) \\
& (\text{OMG} - \text{RFS}) - \text{SIN}(\text{BETA}) (\text{SIN}(\text{PSI}) \text{QFS} - \text{PFS} \text{COS}(\text{PSI})) \\
& (\text{COS}(\text{DELTA}) \text{RDELTA} + \text{DELE})) (\text{RFS} - \text{OMG}) \\
& + (- \text{COS}(\text{PSI}) \text{QFS} - \text{PFS} \text{SIN}(\text{PSI})) ((\text{COS}(\text{PSI}) \text{QFS} + \text{PFS} \text{SIN}(\text{PSI})) \\
& (\text{COS}(\text{BETA}) (\text{COS}(\text{DELTA}) \text{RDELTA} + \text{DELE}) + \text{EBETA}) \\
& + \text{SIN}(\text{DELTA}) (\text{PFS} \text{COS}(\text{PSI}) - \text{SIN}(\text{PSI}) \text{QFS}) \text{RDELTA}) \\
& - \text{SIN}(\text{BETA}) (- \text{COS}(\text{PSI}) \frac{\text{dQFS}}{\text{dT}} + \text{SIN}(\text{PSI}) \frac{\text{dPSI}}{\text{dT}} \text{QFS} - \text{PFS} \text{COS}(\text{PSI}) \frac{\text{dPSI}}{\text{dT}} \\
& \frac{\text{dPFS}}{\text{dT}} \text{SIN}(\text{PSI})) (\text{COS}(\text{DELTA}) \text{RDELTA} + \text{DELE}) \\
& - \text{SIN}(\text{BETA}) \frac{\text{d}^2 \text{BETA}}{\text{dT}^2} (\text{COS}(\text{DELTA}) \text{RDELTA} + \text{DELE}) \\
& - \text{COS}(\text{BETA}) \frac{\text{dBETA}^2}{\text{dT}} (\text{COS}(\text{DELTA}) \text{RDELTA} + \text{DELE}) \\
& - \text{COS}(\text{BETA}) \text{SIN}(\text{DELTA}) \frac{\text{d}^2 \text{DELTA}}{\text{dT}^2} \text{RDELTA} - \text{COS}(\text{BETA}) \text{COS}(\text{DELTA}) \frac{\text{dDELTA}^2}{\text{dT}} \text{RDELTA} \\
& + 2 \text{SIN}(\text{BETA}) \frac{\text{dBETA}}{\text{dT}} \text{SIN}(\text{DELTA}) \frac{\text{dDELTA}}{\text{dT}} \text{RDELTA} + \text{AHFSY} \text{SIN}(\text{PSI}) - \text{AHFSX} \text{COS}(\text{PSI})
\end{aligned}$$

$a_{rsz} =$

$$\begin{aligned}
& (\text{COS}(\text{PSI}) \text{QFS} + \text{PFS} \text{SIN}(\text{PSI})) (\text{SIN}(\text{DELTA}) \text{RDELTA} (\text{RFS} - \text{OMG}) \\
& - \text{SIN}(\text{BETA}) (- \text{COS}(\text{PSI}) \text{QFS} - \text{PFS} \text{SIN}(\text{PSI})) (\text{COS}(\text{DELTA}) \text{RDELTA} + \text{DELE})) \\
& + (\text{PFS} \text{COS}(\text{PSI}) - \text{SIN}(\text{PSI}) \text{QFS}) ((\text{COS}(\text{BETA}) (\text{COS}(\text{DELTA}) \text{RDELTA} + \text{DELE})
\end{aligned}$$

$$+ EBETA) (OMG - RFS) - SIN(BETA) (SIN(PHI) QFS - PFS COS(PHI))$$

$$(COS(DELTA) RDELTA + DELE)) + 2 ((COS(PHI) QFS + PFS SIN(PHI))$$

$$(- SIN(BETA) \frac{dBETA}{dT} (COS(DELTA) RDELTA + DELE)$$

$$- COS(BETA) SIN(DELTA) \frac{dDELTA}{dT} RDELTA) + COS(DELTA) \frac{dDELTA}{dT}$$

$$(PFS COS(PHI) - SIN(PHI) QFS) RDELTA) + (COS(PHI) \frac{dQFS}{dT} - SIN(PHI) \frac{dPSI}{dT} QFS$$

$$+ PFS COS(PHI) \frac{dPSI}{dT} + \frac{dPFS}{dT} SIN(PHI)) (COS(BETA) (COS(DELTA) RDELTA + DELE)$$

$$+ EBETA) - COS(BETA) \frac{d^2 BETA}{dT^2} (COS(DELTA) RDELTA + DELE)$$

$$+ SIN(BETA) \frac{dBETA^2}{dT} (COS(DELTA) RDELTA + DELE)$$

$$+ SIN(DELTA) (- SIN(PHI) \frac{dQFS}{dT} - COS(PHI) \frac{dPSI}{dT} QFS - PFS SIN(PHI) \frac{dPSI}{dT}$$

$$+ \frac{dPFS}{dT} COS(PHI)) RDELTA + SIN(BETA) SIN(DELTA) \frac{d^2 DELTA}{dT^2} RDELTA$$

$$+ SIN(BETA) COS(DELTA) \frac{d^2 DELTA}{dT^2} RDELTA$$

$$+ 2 COS(BETA) \frac{dBETA}{dT} SIN(DELTA) \frac{dDELTA}{dT} RDELTA + AHFSZ$$

Lead-lag equation of motion

$\ddot{\delta} =$

```

((COS(BETA)*'DIFF(RFS,T,1)+(1-COS(BETA)**2)*COS(DELTA)*SIN(DELTA)*
1 RFS**2+(((2*SIN(BETA)*COS(DELTA)**2-SIN(BETA))*COS(PSI)-2*COS(B
2 ETA)*SIN(BETA)*COS(DELTA)*SIN(DELTA)*SIN(PSI))*QFS+(2*SIN(BETA)
3 *COS(DELTA)**2-SIN(BETA))*PFS*SIN(PSI)+2*COS(BETA)*SIN(BETA)*CO
4 S(DELTA)*SIN(DELTA)*PFS*COS(PSI)+(2*COS(BETA)**2-2)*COS(DELTA)*
5 SIN(DELTA)*OMG-2*SIN(BETA)*'DIFF(BETA,T,1)*COS(DELTA)**2)*RFS+S
6 IN(BETA)*SIN(PSI)*'DIFF(QFS,T,1)+((COS(BETA)-2*COS(BETA)*COS(DE
7 LTA)**2)*COS(PSI)*SIN(PSI)+(-COS(BETA)**2-1)*COS(DELTA)*SIN(DEL
8 TA)*COS(PSI)**2+COS(BETA)**2*COS(DELTA)*SIN(DELTA))*QFS**2+(SIN
9 (BETA)*COS(PSI)*'DIFF(PSI,T,1)+((-2*COS(BETA)**2-2)*COS(DELTA)*
: SIN(DELTA)*PFS*COS(PSI)+2*COS(BETA)*SIN(BETA)*COS(DELTA)*SIN(DE
; LTA)*OMG+2*COS(BETA)*'DIFF(BETA,T,1)*COS(DELTA)**2)*SIN(PSI)+(4
< *COS(BETA)*COS(DELTA)**2-2*COS(BETA))*PFS*COS(PSI)**2+((SIN(BET
= A)-2*SIN(BETA)*COS(DELTA)**2)*OMG+2*'DIFF(BETA,T,1)*COS(DELTA)*
> SIN(DELTA))*COS(PSI)+(COS(BETA)-2*COS(BETA)*COS(DELTA)**2)*PFS)
? *QFS+SIN(BETA)*PFS*SIN(PSI)*'DIFF(PSI,T,1)+((2*COS(BETA)*COS(DE
@ LTA)**2-COS(BETA))*PFS**2*COS(PSI)+((SIN(BETA)-2*SIN(BETA)*COS(
1 DELTA)**2)*OMG+2*'DIFF(BETA,T,1)*COS(DELTA)*SIN(DELTA))*PFS)*SI
2 N(PSI)+(COS(BETA)**2+1)*COS(DELTA)*SIN(DELTA)*PFS**2*COS(PSI)**
3 2+((-2*COS(BETA)*SIN(BETA)*COS(DELTA)*SIN(DELTA)*OMG-2*COS(BETA
4 )*'DIFF(BETA,T,1)*COS(DELTA)**2)*PFS-SIN(BETA)*'DIFF(PFS,T,1))*
5 COS(PSI)-COS(DELTA)*SIN(DELTA)*PFS**2-COS(BETA)*'DIFF(OMG,T,1)+
6 (1-COS(BETA)**2)*COS(DELTA)*SIN(DELTA)*OMG**2+2*SIN(BETA)*'DIFF
7 (BETA,T,1)*COS(DELTA)**2*OMG-('DIFF(BETA,T,1))**2*COS(DELTA)*SI
8 N(DELTA))*SM+(COS(DELTA)*EBETA+COS(BETA)*DELE*COS(DELTA))*FM*'D
9 IFF(RFS,T,1)+(-COS(BETA)*SIN(DELTA)*EBETA-COS(BETA)**2*DELE*SIN
: (DELTA))*FM*RFS**2+(((SIN(BETA)*SIN(DELTA)*EBETA-2*COS(BETA)*S
; IN(BETA)*DELE*SIN(DELTA))*FM*SIN(PSI)+SIN(BETA)*DELE*COS(DELTA)
< *FM*COS(PSI))*QFS+SIN(BETA)*DELE*COS(DELTA)*FM*PFS*SIN(PSI)+(SI
= N(BETA)*SIN(DELTA)*EBETA+2*COS(BETA)*SIN(BETA)*DELE*SIN(DELTA))
> *FM*PFS*COS(PSI)+(2*COS(BETA)*SIN(DELTA)*EBETA+2*COS(BETA)**2*D
? ELE*SIN(DELTA))*FM*OMG-2*SIN(BETA)*'DIFF(BETA,T,1)*DELE*COS(DEL
@ TA)*FM)*RFS+(SIN(BETA)*DELE*COS(DELTA)*FM*SIN(PSI)-SIN(BETA)*SI
1 N(DELTA)*EBETA*FM*COS(PSI))*'DIFF(QFS,T,1)+((-COS(DELTA)*EBETA-
2 COS(BETA)*DELE*COS(DELTA))*FM*COS(PSI)*SIN(PSI)+(-COS(BETA)*SIN
3 (DELTA)*EBETA-COS(BETA)**2*DELE*SIN(DELTA))*FM*COS(PSI)**2+(COS
4 (BETA)**2-1)*DELE*SIN(DELTA)*FM)*QFS**2+((SIN(BETA)*SIN(DELTA)*
5 EBETA*FM*SIN(PSI)+SIN(BETA)*DELE*COS(DELTA)*FM*COS(PSI))*'DIFF(
6 PSI,T,1)+((-2*COS(BETA)*SIN(DELTA)*EBETA-2*COS(BETA)**2*DELE*SI
7 N(DELTA))*FM*PFS*COS(PSI)+(SIN(BETA)*SIN(DELTA)*EBETA+2*COS(BET
8 A)*SIN(BETA)*DELE*SIN(DELTA))*FM*OMG+2*COS(BETA)*'DIFF(BETA,T,1
9 )*DELE*COS(DELTA)*FM)*SIN(PSI)+(2*COS(DELTA)*EBETA+2*COS(BETA)*
: DELE*COS(DELTA))*FM*PFS*COS(PSI)**2+(2*'DIFF(BETA,T,1)*DELE*SIN
; (DELTA)*FM-SIN(BETA)*DELE*COS(DELTA))*FM*OMG)*COS(PSI)+(-COS(DEL
< TA)*EBETA-COS(BETA)*DELE*COS(DELTA))*FM*OMG)*COS(PSI)+(-COS(DEL
= E*COS(DELTA)*FM*PFS*SIN(PSI)-SIN(BETA)*SIN(DELTA)*EBETA*FM*PFS*
> COS(PSI))*'DIFF(PSI,T,1)+((COS(DELTA)*EBETA+COS(BETA)*DELE*COS(

```

```

? DELTA))*FM*PFS**2*COS(PSI)-SIN(BETA)*SIN(DELTA)*EBETA*FM*'DIFF(
@ PFS,T,1)+(2*'DIFF(BETA,T,1)*DELE*SIN(DELTA)*FM-SIN(BETA)*DELE*C
1 OS(DELTA)*FM*OMG)*PFS+(AHFSY*COS(BETA)*SIN(DELTA)-AHFSX*COS(DEL
2 TA))*FM)*SIN(PSI)+(COS(BETA)*SIN(DELTA)*EBETA+COS(BETA)**2*DELE
3 *SIN(DELTA))*FM*PFS**2*COS(PSI)**2+(-SIN(BETA)*DELE*COS(DELTA)*
4 FM*'DIFF(PFS,T,1)+((-SIN(BETA)*SIN(DELTA)*EBETA-2*COS(BETA)*SIN
5 (BETA)*DELE*SIN(DELTA))*FM*OMG-2*COS(BETA)**'DIFF(BETA,T,1)*DELE
6 *COS(DELTA)*FM)*PFS+(-AHFSX*COS(BETA)*SIN(DELTA)-AHFSY*COS(DEL
7 TA))*FM)*COS(PSI)+(-COS(BETA)*SIN(DELTA)*EBETA-DELE*SIN(DELTA))*
8 FM*PFS**2+(-COS(DELTA)*EBETA-COS(BETA)*DELE*COS(DELTA))*FM*'DIF
9 F(OMG,T,1)+(-COS(BETA)*SIN(DELTA)*EBETA-COS(BETA)**2*DELE*SIN(D
: ELTA))*FM*OMG**2+2*SIN(BETA)**'DIFF(BETA,T,1)*DELE*COS(DELTA)*FM
; *OMG-MRL1Z-MAL1Z+(-'DIFF(BETA,T,1))**2*DELE-AHFSZ*SIN(BETA))*S
< IN(DELTA)*FM)/SM

```

Flapping equation of motion

$\ddot{\beta} =$

```

((SIN(BETA)*COS(DELTA)*SIN(DELTA)*'DIFF(RFS,T,1)-COS(BETA)*SIN(BET
1 A)*COS(DELTA)**2*RFS**2+(((2*COS(BETA)**2-1)*COS(DELTA)**2*SIN(
2 PSI)+COS(BETA)*COS(DELTA)*SIN(DELTA)*COS(PSI))*QFS+COS(BETA)*CO
3 S(DELTA)*SIN(DELTA)*PFS*SIN(PSI)+(1-2*COS(BETA)**2)*COS(DELTA)*
4 *2*PFS*COS(PSI)+2*COS(BETA)*SIN(BETA)*COS(DELTA)**2*OMG+2*SIN(B
5 ETA)*COS(DELTA)**2*'DIFF(DELTA,T,1))*RFS+(COS(DELTA)**2*COS(PSI
6 )-COS(BETA)*COS(DELTA)*SIN(DELTA)*SIN(PSI))*'DIFF(QFS,T,1)+(COS
7 (BETA)*SIN(BETA)*COS(DELTA)**2*SIN(PSI)**2+SIN(BETA)*COS(DELTA)
8 *SIN(DELTA)*COS(PSI)*SIN(PSI))*QFS**2+((-COS(DELTA)**2*SIN(PSI)
9 -COS(BETA)*COS(DELTA)*SIN(DELTA)*COS(PSI))*'DIFF(PSI,T,1)+SIN(B
: ETA)*COS(DELTA)*SIN(DELTA)*PFS*SIN(PSI)**2+(-2*COS(BETA)*SIN(BE
; TA)*COS(DELTA)**2*PFS*COS(PSI)+(1-2*COS(BETA)**2)*COS(DELTA)**2
< *OMG-2*COS(BETA)*COS(DELTA)**2*'DIFF(DELTA,T,1))*SIN(PSI)-SIN(B
= ETA)*COS(DELTA)*SIN(DELTA)*PFS*COS(PSI)**2+(-COS(BETA)*COS(DEL
> TA)*SIN(DELTA)*OMG-2*COS(DELTA)*SIN(DELTA)*'DIFF(DELTA,T,1))*COS
? (PSI))*QFS+(COS(DELTA)**2*PFS*COS(PSI)-COS(BETA)*COS(DELTA)*SIN
@ (DELTA)*PFS*SIN(PSI))*'DIFF(PSI,T,1)+(-SIN(BETA)*COS(DELTA)*SIN
1 (DELTA)*PFS**2*COS(PSI)+COS(DELTA)**2*'DIFF(PFS,T,1)+(-COS(BETA
2 )*COS(DELTA)*SIN(DELTA)*OMG-2*COS(DELTA)*SIN(DELTA)*'DIFF(DELTA
3 ,T,1))*PFS)*SIN(PSI)+COS(BETA)*SIN(BETA)*COS(DELTA)**2*PFS**2*C
4 OS(PSI)**2+(COS(BETA)*COS(DELTA)*SIN(DELTA)*'DIFF(PFS,T,1)+((2*
5 COS(BETA)**2-1)*COS(DELTA)**2*OMG+2*COS(BETA)*COS(DELTA)**2*'DI
6 FF(DELTA,T,1))*PFS)*COS(PSI)-SIN(BETA)*COS(DELTA)*SIN(DELTA)*'D
7 IFF(OMG,T,1)-COS(BETA)*SIN(BETA)*COS(DELTA)**2*OMG**2-2*SIN(BET
8 A)*COS(DELTA)**2*'DIFF(DELTA,T,1)*OMG+2*'DIFF(BETA,T,1)*COS(DEL
9 TA)*SIN(DELTA)*'DIFF(DELTA,T,1))*SM+SIN(BETA)*DELE*SIN(DELTA)*F
: M*'DIFF(RFS,T,1)+((-SIN(BETA)*DELE*EBETA-COS(BETA)*SIN(BETA)*DE
; LE**2)*M+(-SIN(BETA)*COS(DELTA)*EBETA-2*COS(BETA)*SIN(BETA)*DEL
< E*COS(DELTA))*FM)*RFS**2+(((COS(BETA)*DELE*EBETA+(2*COS(BETA)*
= *2-1)*DELE**2)*M+(COS(BETA)*COS(DELTA)*EBETA+(4*COS(BETA)**2-2)
> *DELE*COS(DELTA))*FM)*SIN(PSI)+COS(BETA)*DELE*SIN(DELTA)*FM*COS

```

```

? (PSI))*QFS+COS(BETA)*DELE*SIN(DELTA)*FM*PFS*SIN(PSI)+(((1-2*COS
@ (BETA)**2)*DELE**2-COS(BETA)*DELE*EBETA)*M+((2-4*COS(BETA)**2)*
1 DELE*COS(DELTA)-COS(BETA)*COS(DELTA)*EBETA)*FM)*PFS*COS(PSI)+((
2 2*SIN(BETA)*DELE*EBETA+2*COS(BETA)*SIN(BETA)*DELE**2)*M+(2*SIN(
3 BETA)*COS(DELTA)*EBETA+4*COS(BETA)*SIN(BETA)*DELE*COS(DELTA))*F
4 M)*OMG+2*SIN(BETA)*DELE*COS(DELTA)*'DIFF(DELTA,T,1)*FM)*RFS+(((
5 COS(BETA)*DELE*EBETA+DELE**2)*M+(COS(BETA)*COS(DELTA)*EBETA+2*D
6 ELE*COS(DELTA))*FM)*COS(PSI)-COS(BETA)*DELE*SIN(DELTA)*FM*SIN(P
7 SI))*'DIFF(QFS,T,1)+((COS(BETA)*SIN(BETA)*DELE**2*M+2*COS(BETA)
8 *SIN(BETA)*DELE*COS(DELTA)*FM)*SIN(PSI)**2+SIN(BETA)*DELE*SIN(D
9 ELTA)*FM*COS(PSI)*SIN(PSI)+(-SIN(BETA)*DELE*EBETA*M-SIN(BETA)*C
: OS(DELTA)*EBETA*FM)*COS(PSI)**2)*QFS**2+((((-COS(BETA)*DELE*EBE
; TA-DELE**2)*M+(-COS(BETA)*COS(DELTA)*EBETA-2*DELE*COS(DELTA))*F
< M)*SIN(PSI)-COS(BETA)*DELE*SIN(DELTA)*FM*COS(PSI))*'DIFF(PSI,T,
= 1)+SIN(BETA)*DELE*SIN(DELTA)*FM*PFS*SIN(PSI)**2+(((2*SIN(BETA)
> *DELE*EBETA-2*COS(BETA)*SIN(BETA)*DELE**2)*M+(-2*SIN(BETA)*COS(
? DELTA)*EBETA-4*COS(BETA)*SIN(BETA)*DELE*COS(DELTA))*FM)*PFS*COS
@ (PSI)+(((1-2*COS(BETA)**2)*DELE**2-COS(BETA)*DELE*EBETA)*M+((2-
1 4*COS(BETA)**2)*DELE*COS(DELTA)-COS(BETA)*COS(DELTA)*EBETA)*FM)
2 *OMG-2*COS(BETA)*DELE*COS(DELTA)*'DIFF(DELTA,T,1)*FM)*SIN(PSI)-
3 SIN(BETA)*DELE*SIN(DELTA)*FM*PFS*COS(PSI)**2+(-COS(BETA)*DELE*S
4 IN(DELTA)*FM*OMG-2*DELE*SIN(DELTA)*'DIFF(DELTA,T,1)*FM)*COS(PSI
5 ))*QFS+(((COS(BETA)*DELE*EBETA+DELE**2)*M+(COS(BETA)*COS(DELTA)
6 *EBETA+2*DELE*COS(DELTA))*FM)*PFS*COS(PSI)-COS(BETA)*DELE*SIN(D
7 ELTA)*FM*PFS*SIN(PSI))*'DIFF(PSI,T,1)+(-SIN(BETA)*DELE*EBETA*M-
8 SIN(BETA)*COS(DELTA)*EBETA*FM)*PFS**2*SIN(PSI)**2+(-SIN(BETA)*D
9 ELE*SIN(DELTA)*FM*PFS**2*COS(PSI)+((COS(BETA)*DELE*EBETA+DELE**
: 2)*M+(COS(BETA)*COS(DELTA)*EBETA+2*DELE*COS(DELTA))*FM)*'DIFF(P
; FS,T,1)+(-COS(BETA)*DELE*SIN(DELTA)*FM*OMG-2*DELE*SIN(DELTA)*'D
< IFF(DELTA,T,1)*FM)*PFS+AHFSY*SIN(BETA)*DELE*M+AHFSY*SIN(BETA)*C
= OS(DELTA)*FM)*SIN(PSI)+(COS(BETA)*SIN(BETA)*DELE**2*M+2*COS(BET
> A)*SIN(BETA)*DELE*COS(DELTA)*FM)*PFS**2*COS(PSI)**2+(COS(BETA)*
? DELE*SIN(DELTA)*FM)*'DIFF(PFS,T,1)+(((COS(BETA)*DELE*EBETA+(2*CO
@ S(BETA)**2-1)*DELE**2)*M+(COS(BETA)*COS(DELTA)*EBETA+(4*COS(BET
1 A)**2-2)*DELE*COS(DELTA))*FM)*OMG+2*COS(BETA)*DELE*COS(DELTA)*'
2 DIFF(DELTA,T,1)*FM)*PFS-AHFSX*SIN(BETA)*DELE*M-AHFSX*SIN(BETA)*
3 COS(DELTA)*FM)*COS(PSI)-SIN(BETA)*DELE*SIN(DELTA)*FM)*'DIFF(OMG,
4 T,1)+((-SIN(BETA)*DELE*EBETA-COS(BETA)*SIN(BETA)*DELE**2)*M+(-S
5 IN(BETA)*COS(DELTA)*EBETA-2*COS(BETA)*SIN(BETA)*DELE*COS(DELTA)
6 ))*FM)*OMG**2-2*SIN(BETA)*DELE*COS(DELTA)*'DIFF(DELTA,T,1)*FM*OM
7 G-MRF2X-MAF2X-AHFSZ*COS(BETA)*DELE*M+(2*'DIFF(BETA,T,1)*DELE*SI
8 N(DELTA)*'DIFF(DELTA,T,1)+AHFSZ*COS(BETA)*COS(DELTA))*FM)/(COS(
9 DELTA)**2*SM+DELE**2*M+2*DELE*COS(DELTA)*FM)

```


Appendix B

PRECEDING PAGE BLANK NOT FILMED

PAGE 36 INTENTIONALLY BLANK


```

/*
*****
cross or dot product of two 3D vectors
*****
CROSS3(A,B) :=
BLOCK([CROSSP,TEMP],
TEMP: MATRIX([0,-A[3,1],A[2,1]], [A[3,1],0,-A[1,1]],
[-A[2,1],A[1,1],0]),
CROSSP: TEMP.B,
CROSSP: TEMP.B,
/*
****
****
*/
DOT3(A,B) :=
BLOCK([DOTP,TEMP],
DOTP: MULTTRHD(A[1,1],B[1,1])+MULTTRHD(A[2,1],B[2,1])+
MULTTRHD(A[3,1],B[3,1]),
DOTP);

```

```

/*
****
SUBROUTINE ORG:

This subroutine is an interactive routine for simplifying a given expression
"A". The call is of the form:

    ORG(A, [STATUS])

where "A" is the expression to be simplified. After the routine is invoked
it changes the regular MACSYMA prompt to ORG> signifying that the program
is awaiting the expression to be factored out. After the user enters this
expression, followed by a ";" as usual, the subroutine factors out the
given expression, gives the part that was factored out (calls it THIS TIME:).
Entering a new expression at this point will continue the process by factoring
out this newly entered expression from the REMAINS part. Entering a "QUIT"
will quit the routine. The result of the factoring operation is the sum of the
two parts RUNSUM and RUNREM. If complete factorization is accomplished, RUNREM
will be zero.
****
*/
ORG(EXP, STATUS) := BLOCK([FACT, RUNPART],
    RUNREM: EXP,
    IF STATUS = NEW THEN RUNSUM: 0,
    DO
    (FACT: READ("ORG> "),
    IF FACT # QUIT THEN
        (if atom(FACT) then
            (if ratcoef(runrem, FACT, 1) = 0 then
                runpart: 0
            else
                (runpart: FACT*TRIGSIMPL(
                    RATSIMP(ratcoef(runrem, FACT, 1))),
                    runrem: ratcoef(runrem, FACT, 0),
                    runsum: runsum+runpart))
            else
                (RUNREM: RATSUBST(SUB, FACT, RUNREM),
                IF RATCOEF(RUNREM, SUB, 1) = 0 THEN
                    (RUNPART: 0,
                    runrem: subst(FACT, sub, runrem))
                ELSE
                    (RUNPART: SUB*TRIGSIMPL(
                        RATSIMP(RATCOEF(RUNREM, SUB, 1))),
                    RUNREM: RATEXPAND(RATCOEF(RUNREM, SUB, 0)),
                    RUNREM: SUBST(FACT, SUB, RUNREM),
                    RUNPART: SUBST(FACT, SUB, RUNPART),
                    RUNSUM: RUNSUM+RUNPART)),
                PRINT("THIS TIME: ", RUNPART))
            else
                RETURN("END ORGANIZE")));

```

References

1. Schroeder, J.; Watson, D. C.; Tischler, M. B.; and Eshow, M. M.: Identification and Simulation Evaluation of an AH-64A Helicopter Hover Math Model. AIAA Atmospheric Flight Mechanics Conference, AIAA Paper 91-2877, New Orleans, La., Aug. 12-14, 1991.
2. Curtiss, H. C., Jr.: On the Calculation of Response of Helicopters to Control Inputs. 18th European Rotorcraft Forum, Avignon, France, 1992.
3. Ballin, Mark G.: Validation of a Real-Time Engineering Simulation of the UH-60A Helicopter. NASA TM-88360, Feb. 1987.
4. Kumar, S.; Harding, J.; Bass, S.; Metz, B.; and Mouritsen, S.: AH-64A Apache Engineering Simulation Program Documentation. USAAVSCOM TR 90-A-012, Final Report, Oct. 1990.
5. Harrison, J. M.: An Integrated Approach to Effective Analytical Support of Helicopter Design and Development. Paper no. 52, Proceedings of the Sixth European Rotorcraft and Powered Lift Aircraft Forum, Sept. 16-19, 1980.
6. Tischler, M. B.; and Cauffman, M. G.: Frequency-Response Method for Rotorcraft System Identification: Flight Applications to BO-105 Coupled Rotor/Fuselage Dynamics. J. Amer. Hel. Soc., vol. 37, no. 3, July 1992, pp. 3-17.
7. Howlett, J. J.: UH-60A Black Hawk Engineering Simulation Program: Volume I-Mathematical Model. NASA CR-166309, Dec. 1981.
8. MACSYMA Reference Manual. The Mathlab Group. Laboratory for Computer Science, Massachusetts Institute of Technology, Version 10, Jan. 1983.
9. Chen, Robert T. N.: Flap-Lag Equations of Motion of Rigid, Articulated Rotor Blades with Three Hinge Sequences. NASA TM-100023, Nov. 1987.
10. Acker, G. F., et. al.: Air Vehicle Technical Description Data for the AH-64A Advanced Attack Helicopter. Hughes Helicopter, Inc., Report no. 77-X-8002-3, Mar. 1984.
11. Davis, John M.; Bennett, Richard L.; and Blankenship, Barney L.: Rotorcraft Flight Simulation with Aeroelastic Rotor and Improved Aerodynamic Representation. Volume II-User's Manual. USAAMRDL-TR-74-10B, June 1974.
12. Peters, D. A.; and Ha Quang, N.: Dynamic Inflow for Practical Applications. J. Amer. Hel. Soc., vol. 33, no. 4, 1988, pp. 64-68.
13. IMSL Library Reference Manual, 9th edition. IMSL, Inc., Houston, Tex., 1982.
14. Abbott, William Y., et. al.: Engineering Evaluation of Aeronautical Design Standard (ADS)-33C, Handling Qualities Requirements for Military Rotorcraft, Utilizing an AH-64A Apache Helicopter. TECOM Project no. 4-CO-230-000-004, AVSCOM Project no. 87-17, Nov. 1991.

15. Aeronautical Design Standard-33C, Handling Qualities Requirements for Military Rotorcraft. U.S. Army Aviation Systems Command, St. Louis, Mo., Aug. 1989.
16. Chaimovich, M.; and Mansur, M. H.: Investigation of the Flight Mechanics Simulation of a Hovering Helicopter. Presented at the 48th Annual Forum of the AHS, Washington, D.C., 1992.

Table 1. Aircraft inertias (slug \times ft²)

I_{xx}	6852
I_{yy}	37961
I_{zz}	38260
I_{xz}	4379

Table 2. Aircraft configuration data for hover maneuvers

Maneuver	Main input	Airspeed (kts)	Weight (lb)	C.G. (in.)	Altitude (ft)	Start time (sec)
4020	Lateral	Hover	15399	204.73	100	2.8
4017	Long.	Hover	15475	204.72	100	1.0
4014	Dir.	Hover	15619	204.70	100	2.0
4028	Heave	Hover	15184	204.77	100	2.8

Table 3. Aircraft configuration data for 60 kts maneuvers

Maneuver	Main input	Airspeed (kts)	Weight (lb)	C.G. (in.)	Altitude (ft)	Start time (sec)
4927	Lateral	71	14957	204.80	6000	0.0
4912	Long.	72	15580	204.69	6000	0.0
5105	Dir.	70	15811	204.66	6000	0.0
5112	Heave	75	15372	204.74	6000	0.0

Table 4. Aircraft configuration data for 120 kts maneuvers

Maneuver	Main input	Airspeed (kts)	Weight (lb)	C.G. (in.)	Altitude (ft)	Start time (sec)
4317	Lateral	128	15246	204.65	6000	0.0
4310	Long.	130	15887	204.55	6000	0.0
4320	Dir.	135	15103	204.67	6000	0.0
4326	Heave	131	14740	204.73	6000	0.0

Table 5. (a) Stability derivatives in hover

Derivative	Flight	BEMAP	FLYRT
	Param. value	Param. value	Param. value
X_u	-0.02000 †	-0.03290	-0.03320
X_w	0.000 +	0.02280	0.02790
X_q	0.000 +	1.715	3.023
X_v	0.000 +	-7.000E-03	0.01210
X_p	0.6849	-1.117	-0.4413
X_r	0.000 +	-0.02830	-0.03220
Z_u	0.000 +	6.300E-03	4.500E-03
Z_w	-0.1220	-0.3171	-0.2921
Z_q	0.000 +	0.3261	0.1199
Z_v	0.000 +	1.100E-03	-3.900E-03
Z_p	0.000 +	-0.1442	-0.2241
Z_r	0.000 +	2.357	2.171
M_u	8.443E-04	-4.500E-03	-3.700E-03
M_w	-5.142E-03	1.000E-03	-6.000E-04
M_q	-0.4192	-0.6069	-0.5521
M_v	7.103E-03	2.800E-03	-1.400E-03
M_p	-0.2272	0.2142	0.08750
M_r	-0.09000 †	0.01510	0.01160
Y_u	0.000 +	0.01790	-8.300E-03
Y_w	0.000 +	-1.900E-03	-0.01740
Y_q	0.000 +	-1.375	-1.203
Y_v	-0.2788	-0.05790	-0.05020
Y_p	-1.560	-2.672	-2.938
Y_r	0.000 +	0.6762	0.4704
L_u	0.000 +	0.02360	-6.900E-03
L_w	0.000 +	-2.100E-03	-0.01150
L_q	1.040 †	-1.171	-0.9598
L_v	-4.247E-03	-0.01820	-0.01710
L_p	-1.828	-2.977	-2.424
L_r	0.000 +	0.4681	-0.07800
N_u	0.000 +	2.700E-03	-1.800E-03
N_w	0.000 +	2.000E-04	-7.000E-04
N_q	0.000 +	-0.1570	-0.1114
N_v	3.008E-03	6.400E-03	6.600E-03
N_p	-0.3085	-0.2605	-0.3376
N_r	-0.2702	-0.2291	-0.3176

+Eliminated during model structure determination.

†Fixed value in model.

Table 5. (b) Control derivatives in hover

	Flight	BEMAP	FLYRT
Derivative	Param. value	Param. value	Param. value
X_{lon}	-1.483	-1.519	-1.841
X_{lat}	-0.1939	0.04810	-0.07600
X_{ped}	0.000 +	-0.07430	-0.06320
X_{col}	0.8355	0.6636	0.6897
Z_{lon}	0.000 +	-0.09910	-0.1563
Z_{lat}	0.000 +	3.400E-03	-0.03070
Z_{ped}	0.000 +	-8.000E-03	-1.000E-04
Z_{col}	-5.430	-7.306	-7.863
M_{lon}	0.2353	0.2625	0.3144
M_{lat}	0.05917	-0.02710	0.01330
M_{ped}	0.000 +	0.01750	0.01810
M_{col}	0.000 +	5.000E-04	1.500E-03
Y_{lon}	0.000 +	-0.2022	-0.1123
Y_{lat}	0.4958	1.266	1.287
Y_{ped}	-2.791	-1.796	-1.708
Y_{col}	-0.8557	-0.2165	-0.1659
L_{lon}	-0.1042 †	-0.1370	-0.1000
L_{lat}	0.8341	1.184	1.145
L_{ped}	-0.4008	-0.5612	-0.3560
L_{col}	0.000 +	-0.07360	-0.02640
N_{lon}	0.000 +	-0.01770	-0.01310
N_{lat}	0.1041	0.1553	0.1501
N_{ped}	0.4943	0.5763	0.5887
N_{col}	0.2662	0.1941	0.2915
τ_{lon}	0.08830	0.08830	0.08830
τ_{lat}	0.1206	0.1206	0.1206
τ_{ped}	0.07951	0.07951	0.07951
τ_{col}	0.06107	0.06107	0.06107

+Eliminated during model structure determination.

†Fixed value in model.

Table 6. (a) Stability derivatives at 60 kts

Derivative	BEMAP	FLYRT
	Param. value	Param. value
X_u	-0.03390	-0.03530
X_w	0.02470	0.01900
X_q	-0.03360	1.023
X_v	0.02040	0.05380
X_p	-1.013	-0.1456
X_r	-0.3169	-0.1559
Z_u	-0.06070	-0.05480
Z_w	-0.5419	-0.5034
Z_q	98.40	101.3
Z_v	-0.4638	-0.4439
Z_p	4.714	-0.5447
Z_r	2.557	1.797
M_u	1.700E-03	1.500E-03
M_w	2.300E-03	1.500E-03
M_q	-1.368	-0.8738
M_v	3.300E-03	-2.200E-03
M_p	0.1127	0.04590
M_r	0.02980	0.01120
Y_u	5.400E-03	5.700E-03
Y_w	1.200E-03	-0.03760
Y_q	-1.087	-1.031
Y_v	-0.08810	-0.1706
Y_p	1.615	-0.6978
Y_r	-100.3	-100.3
L_u	-2.700E-03	3.700E-03
L_w	0.01720	-0.01790
L_q	-0.8584	-1.181
L_v	-9.700E-03	-0.08480
L_p	-4.290	-3.067
L_r	-0.1564	-0.1169
N_u	-3.600E-03	-3.600E-03
N_w	-2.000E-03	-7.800E-03
N_q	0.1280	-0.02520
N_v	6.300E-03	-4.800E-03
N_p	-0.5311	-0.4812
N_r	-0.4518	-0.5120

Table 6. (b) Control derivatives at 60 kts

Derivative	BEMAP	FLYRT
	Param. value	Param. value
X_{lon}	-1.615	-1.733
X_{lat}	-0.1791	-0.06850
X_{ped}	0.1434	0.1150
X_{col}	0.1470	0.1416
Z_{lon}	-1.630	-2.462
Z_{lat}	0.1510	-0.07630
Z_{ped}	1.200E-03	8.000E-04
Z_{col}	-6.982	-6.690
M_{lon}	0.3700	0.3316
M_{lat}	0.03360	0.01500
M_{ped}	-0.01550	-5.400E-03
M_{col}	0.09080	0.07190
Y_{lon}	-0.1311	-0.3392
Y_{lat}	0.9025	1.227
Y_{ped}	-1.163	-1.254
Y_{col}	0.04740	-0.1801
L_{lon}	-0.08710	-0.2402
L_{lat}	1.263	1.100
L_{ped}	-0.2921	-0.2558
L_{col}	0.1696	-0.1233
N_{lon}	-0.02670	-0.08140
N_{lat}	0.1495	0.1482
N_{ped}	0.3740	0.4367
N_{col}	0.09920	0.1018
τ_{lon}	0.08830	0.08830
τ_{lat}	0.1206	0.1206
τ_{ped}	0.07951	0.07951
τ_{col}	0.06107	0.06107

Table 7. (a) Stability derivatives at 120 kts

Derivative	BEMAP	FLYRT
	Param. value	Param. value
X_u	-0.05680	-0.05520
X_w	0.02640	0.01360
X_q	10.37	10.29
X_v	0.04610	0.05670
X_p	-0.9485	-0.5177
X_r	-0.06490	-0.05550
Z_u	0.01620	0.02210
Z_w	-0.7376	-0.6446
Z_q	201.0	201.8
Z_v	-1.239	-1.138
Z_p	1.775	-2.334
Z_r	3.022	2.229
M_u	2.200E-03	1.800E-03
M_w	2.600E-03	2.500E-03
M_q	-1.430	-1.077
M_v	7.400E-03	4.400E-03
M_p	0.1902	0.1295
M_r	0.02380	0.02190
Y_u	0.01420	0.01390
Y_w	-3.800E-03	-0.03580
Y_q	-1.044	-0.6811
Y_v	-0.1422	-0.2552
Y_p	-9.555	-10.40
Y_r	-200.7	-200.8
L_u	-4.000E-04	3.200E-03
L_w	0.01440	-9.500E-03
L_q	-1.129	-0.8714
L_v	-3.600E-03	-0.09040
L_p	-3.626	-3.168
L_r	-0.07620	-0.06570
N_u	-5.200E-03	-5.900E-03
N_w	-3.000E-04	-2.500E-03
N_q	0.06130	2.300E-03
N_v	8.300E-03	2.000E-03
N_p	-0.2875	-0.2754
N_r	-0.6668	-0.7556

Table 7. (b) Control derivatives at 120 kts

Derivative	BEMAP	FLYRT
	Param. value	Param. value
X_{lon}	-1.479	-1.771
X_{lat}	-0.1824	-0.06870
X_{ped}	0.09060	0.08340
X_{col}	7.200E-03	-0.04460
Z_{lon}	-5.472	-5.541
Z_{lat}	0.07900	-0.06750
Z_{ped}	0.03120	0.01020
Z_{col}	-8.921	-7.812
M_{lon}	0.4585	0.3965
M_{lat}	0.02830	0.01510
M_{ped}	-0.01170	-1.800E-03
M_{col}	0.1882	0.1579
Y_{lon}	-0.08940	-0.4851
Y_{lat}	0.9004	1.267
Y_{ped}	-1.484	-1.569
Y_{col}	-7.400E-03	-0.3069
L_{lon}	0.05590	-0.2438
L_{lat}	1.280	1.111
L_{ped}	-0.3844	-0.3294
L_{col}	0.2402	-0.05930
N_{lon}	-0.01900	-0.07390
N_{lat}	0.1541	0.1491
N_{ped}	0.4676	0.5437
N_{col}	0.1402	0.1629
τ_{lon}	0.08830	0.08830
τ_{lat}	0.1206	0.1206
τ_{ped}	0.07951	0.07951
τ_{col}	0.06107	0.06107

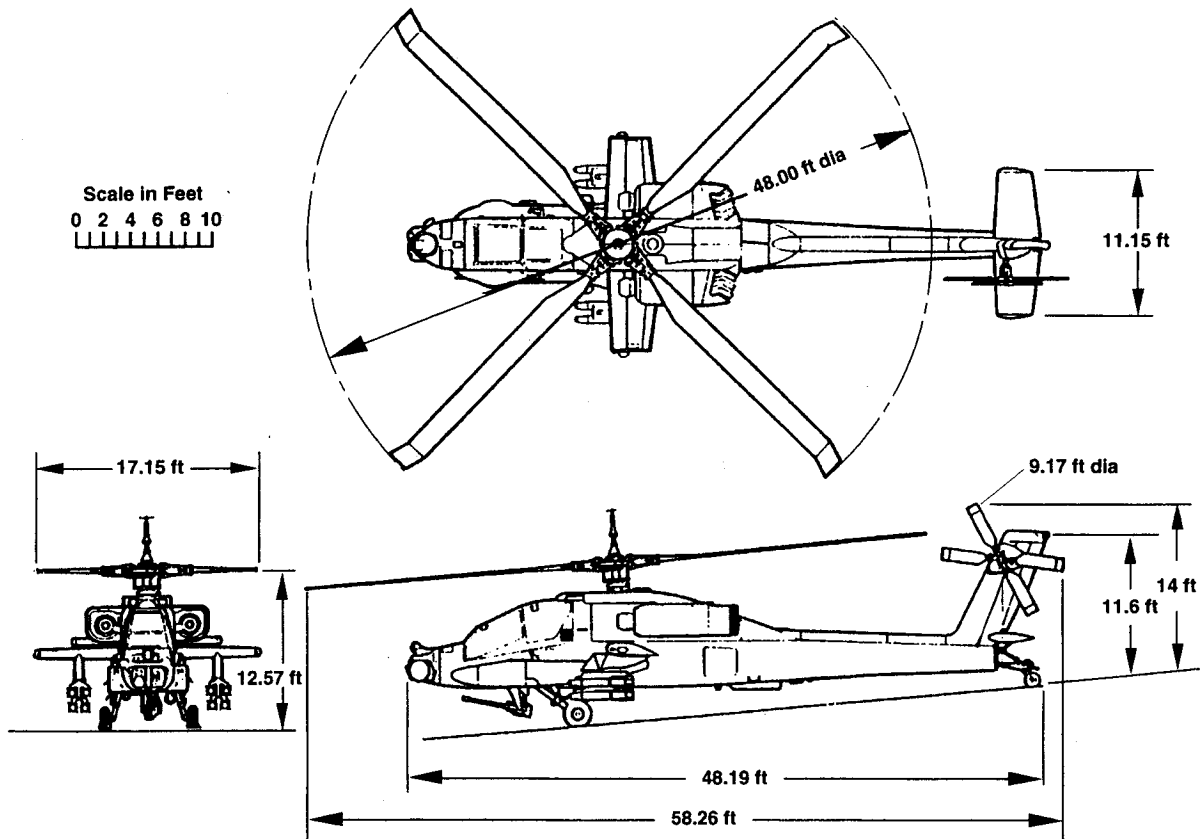
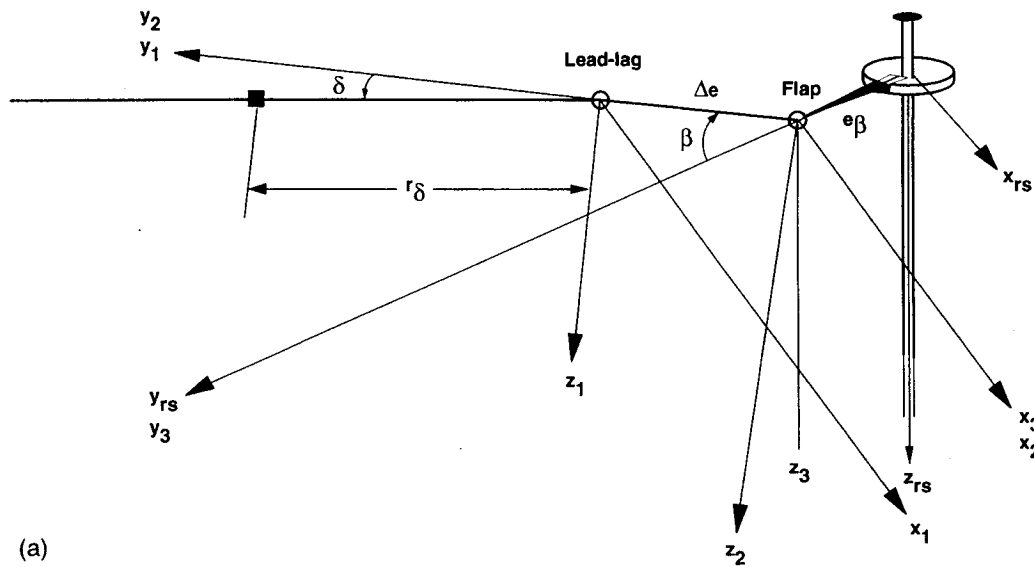


Figure 1. AH-64A three view illustration.



(a)

Figure 2. (a) Coordinate systems used in rotor derivations.

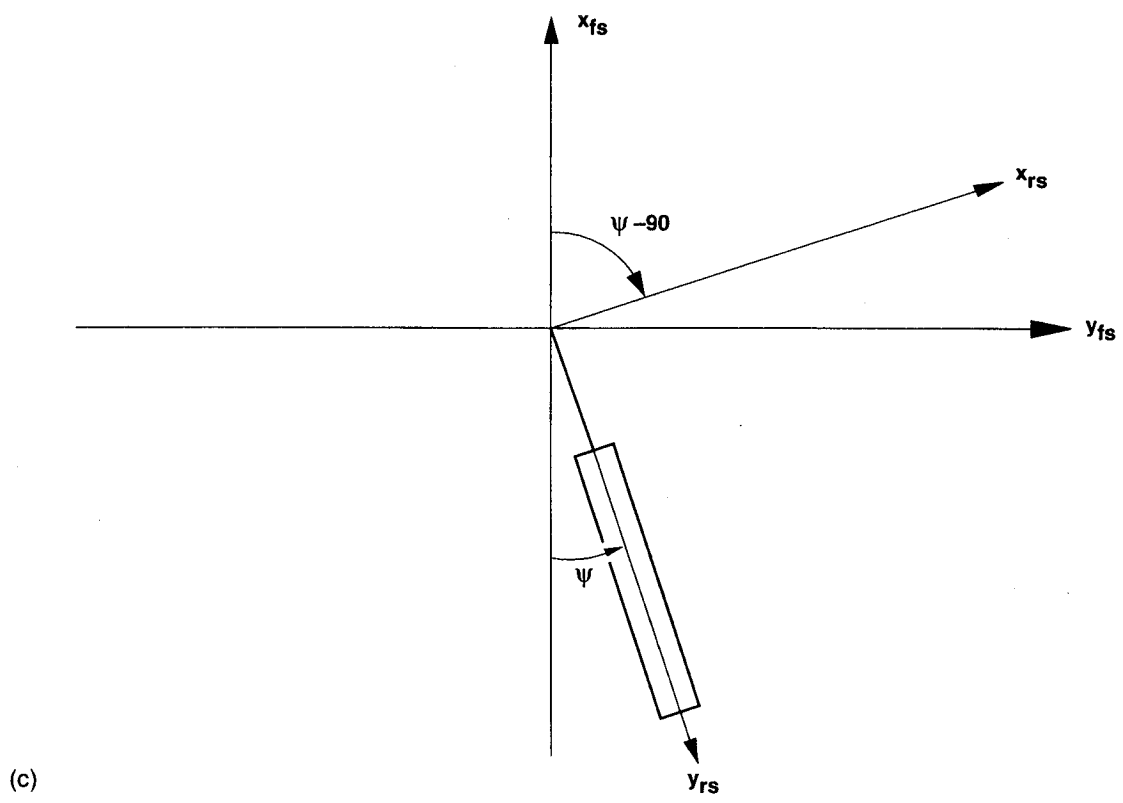
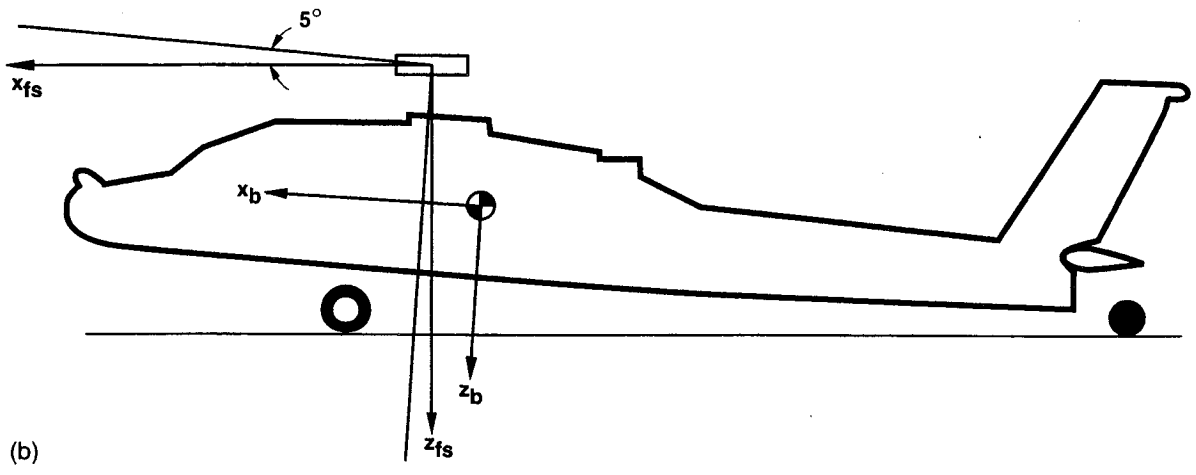


Figure 2. (b) Body and fixed-shaft coordinate systems (drawing not to scale), (c) transformation from fixed to rotating-shaft coordinates.

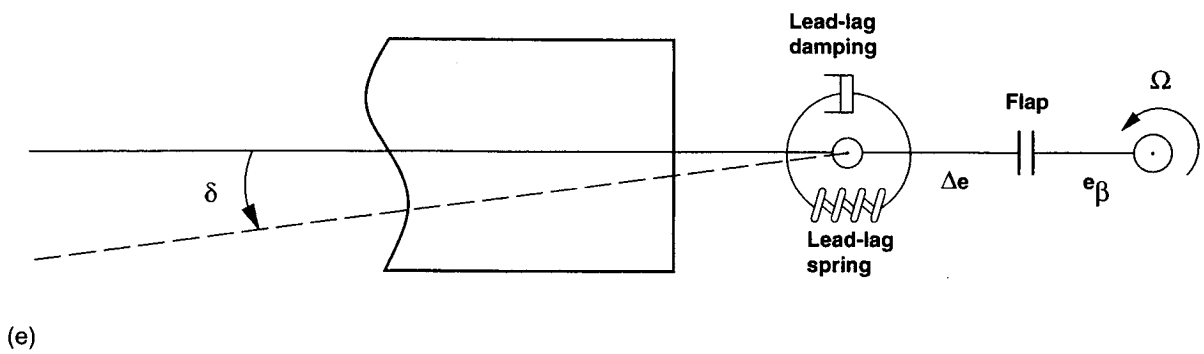
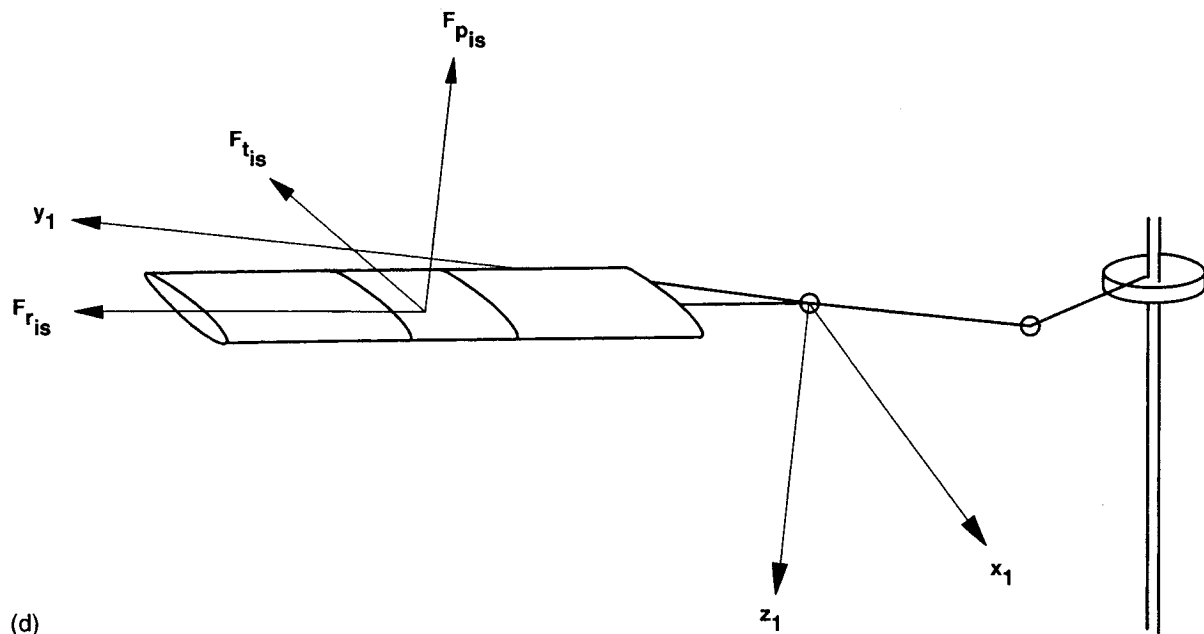


Figure 2. (d) Elemental aerodynamic force components, (e) lead-lag damper modeling.

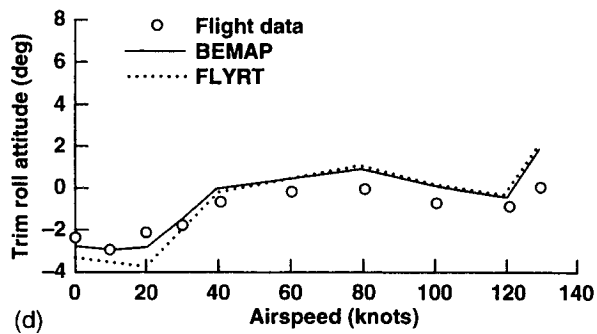
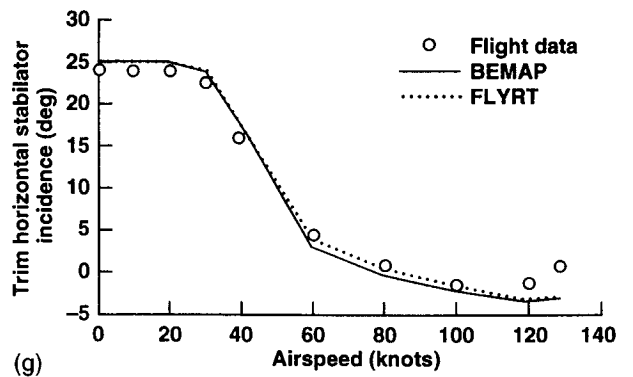
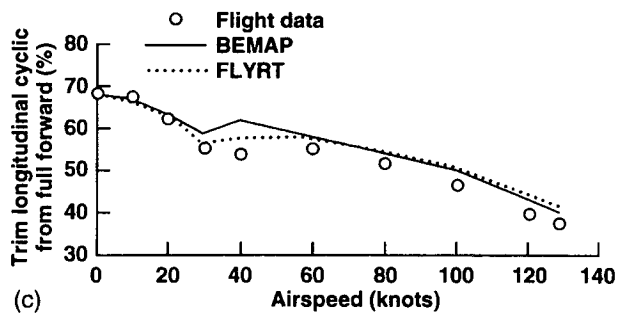
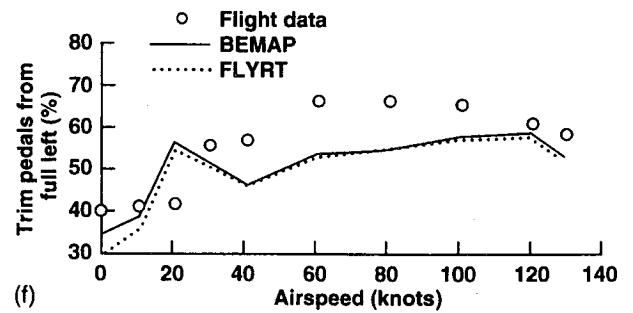
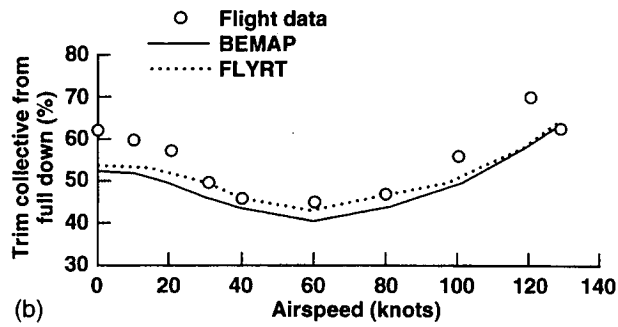
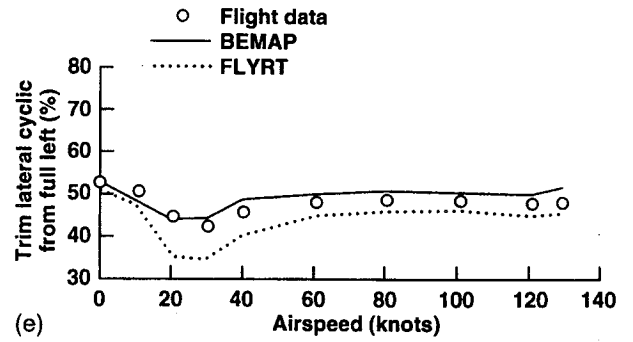
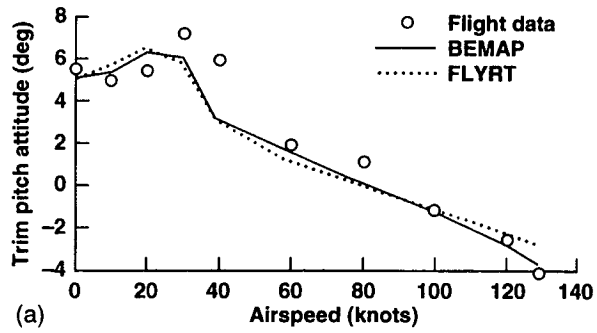


Figure 3. (a) Variation of trim pitch attitude with airspeed, (b) variation of trim collective with airspeed, (c) variation of trim longitudinal cyclic with airspeed, (d) variation of trim roll attitude with airspeed, (e) variation of trim lateral cyclic with airspeed, (f) variation of trim pedals with airspeed, (g) variation of trim horizontal stabilator incidence with airspeed.

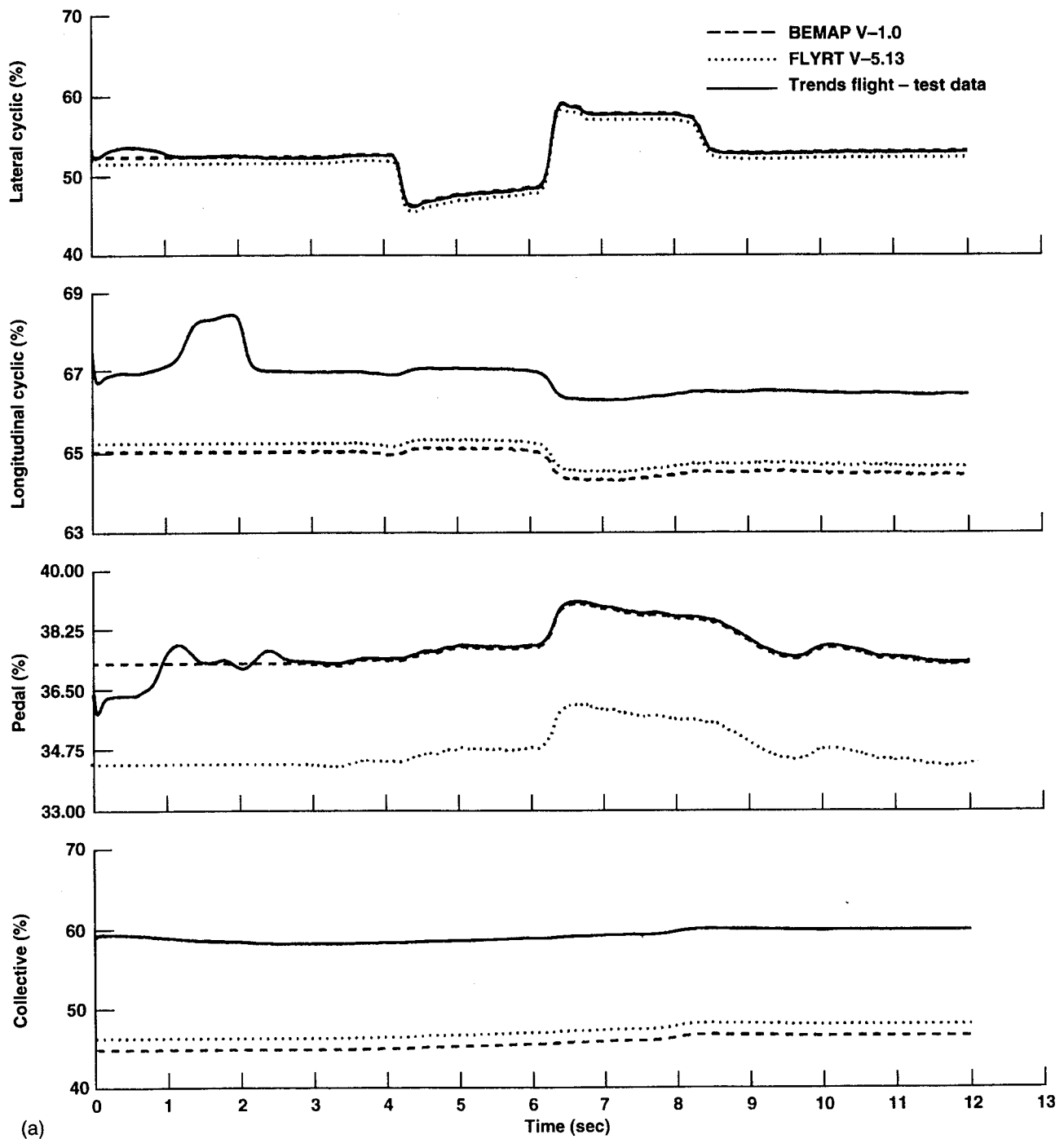


Figure 4. (a) Responses to lateral doublet in hover.

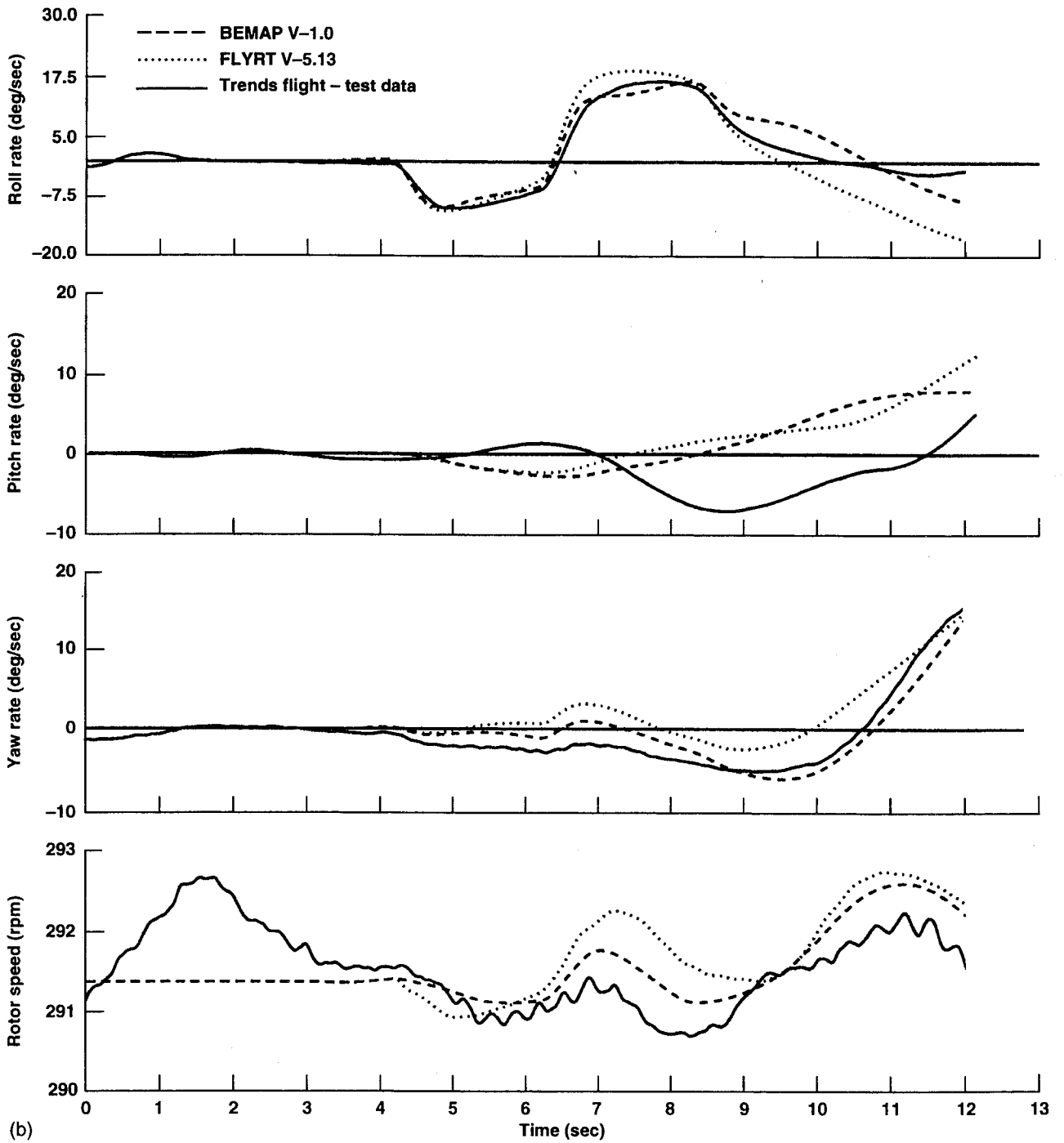


Figure 4. (b) Continued.

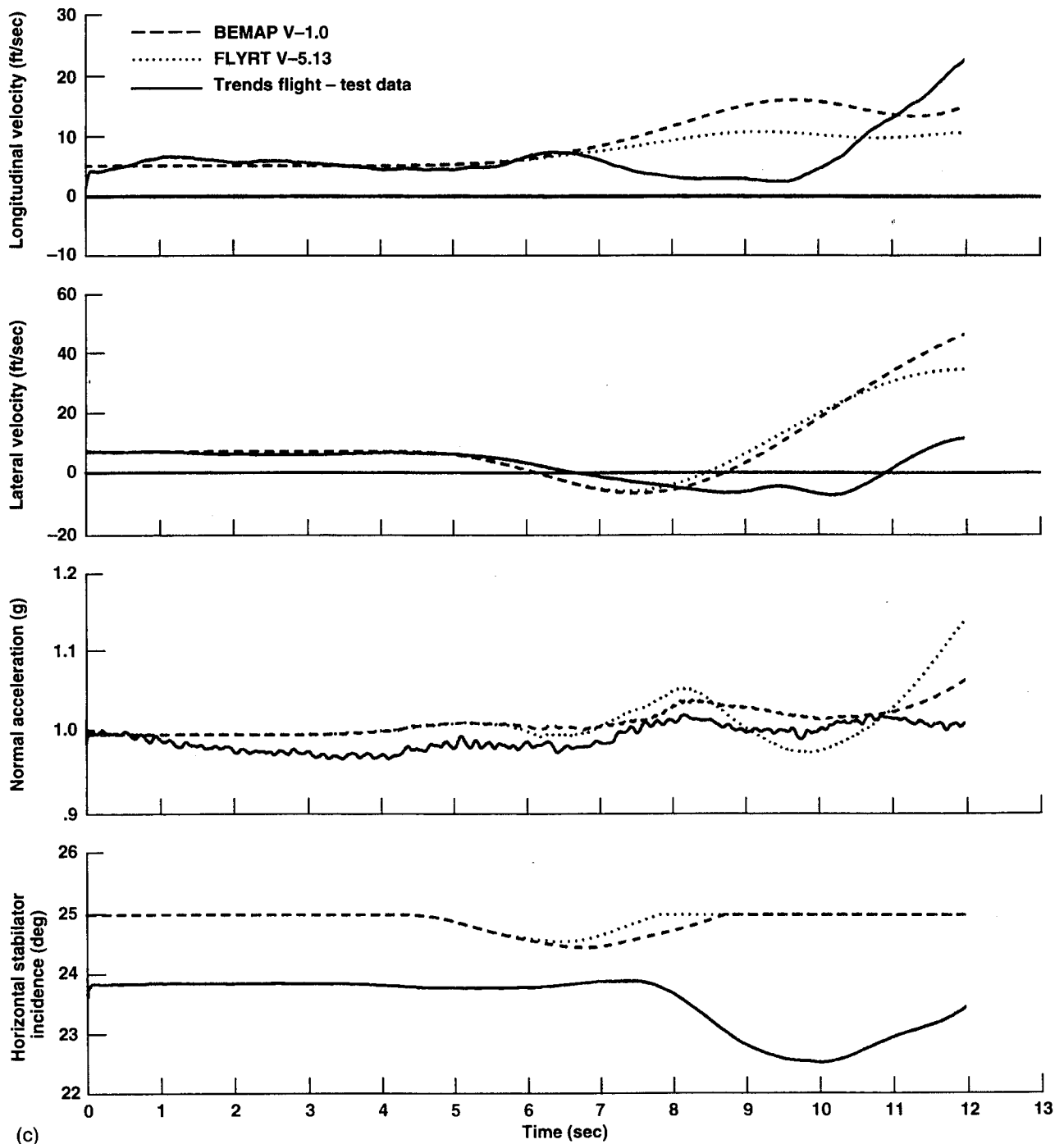


Figure 4. (c) Concluded.

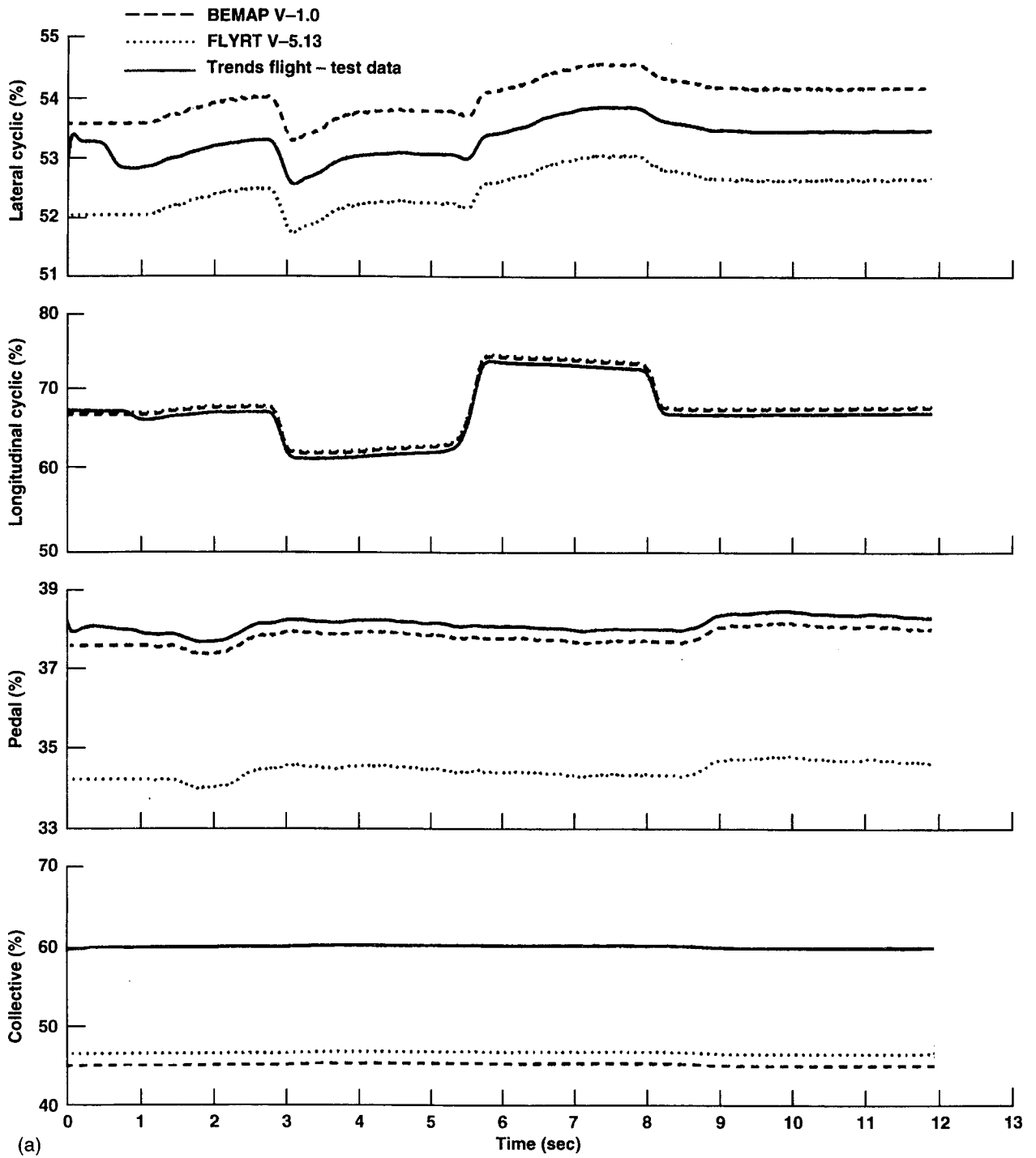


Figure 5. (a) Responses to longitudinal doublet in hover.

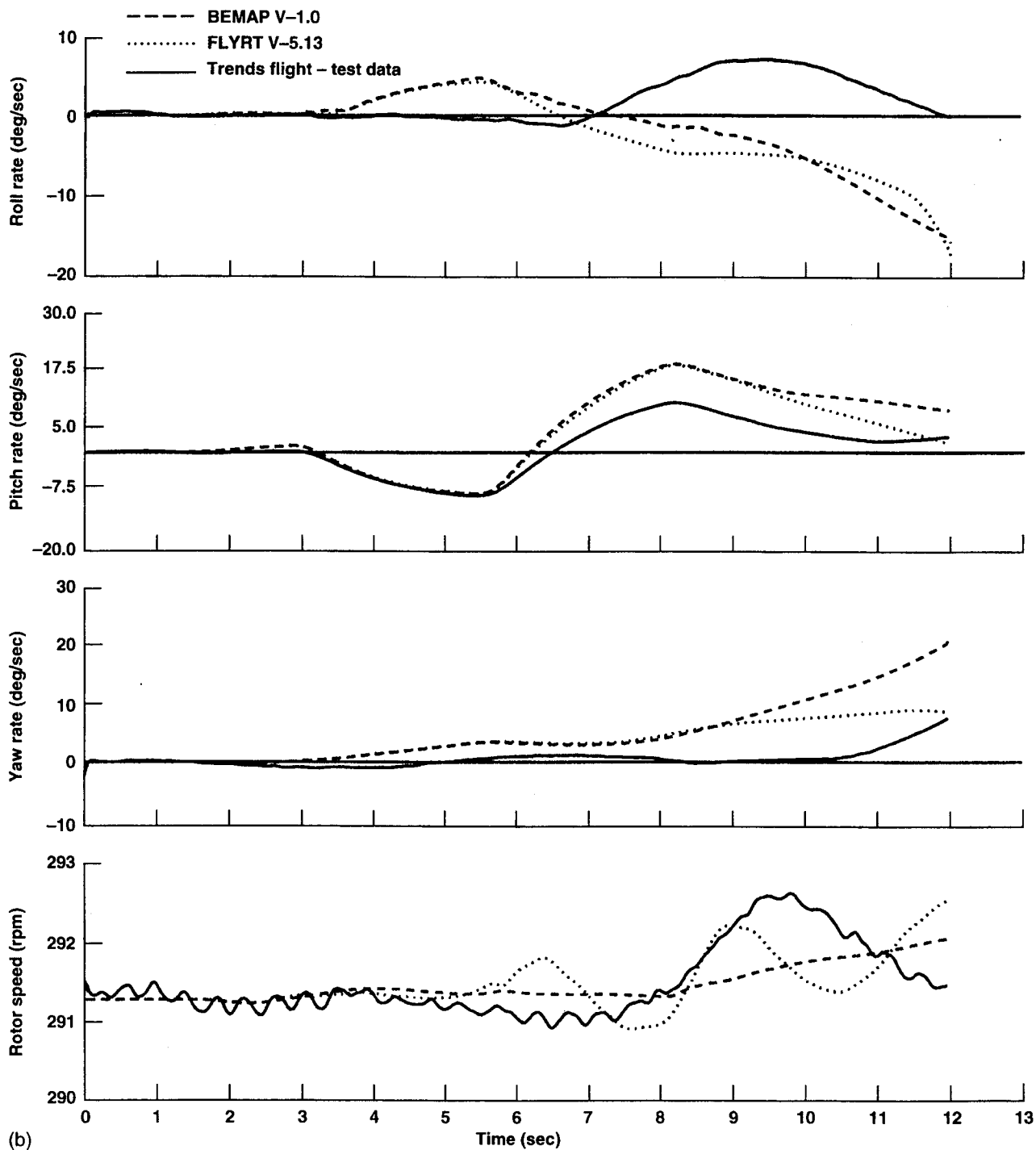


Figure 5. (b) Continued.

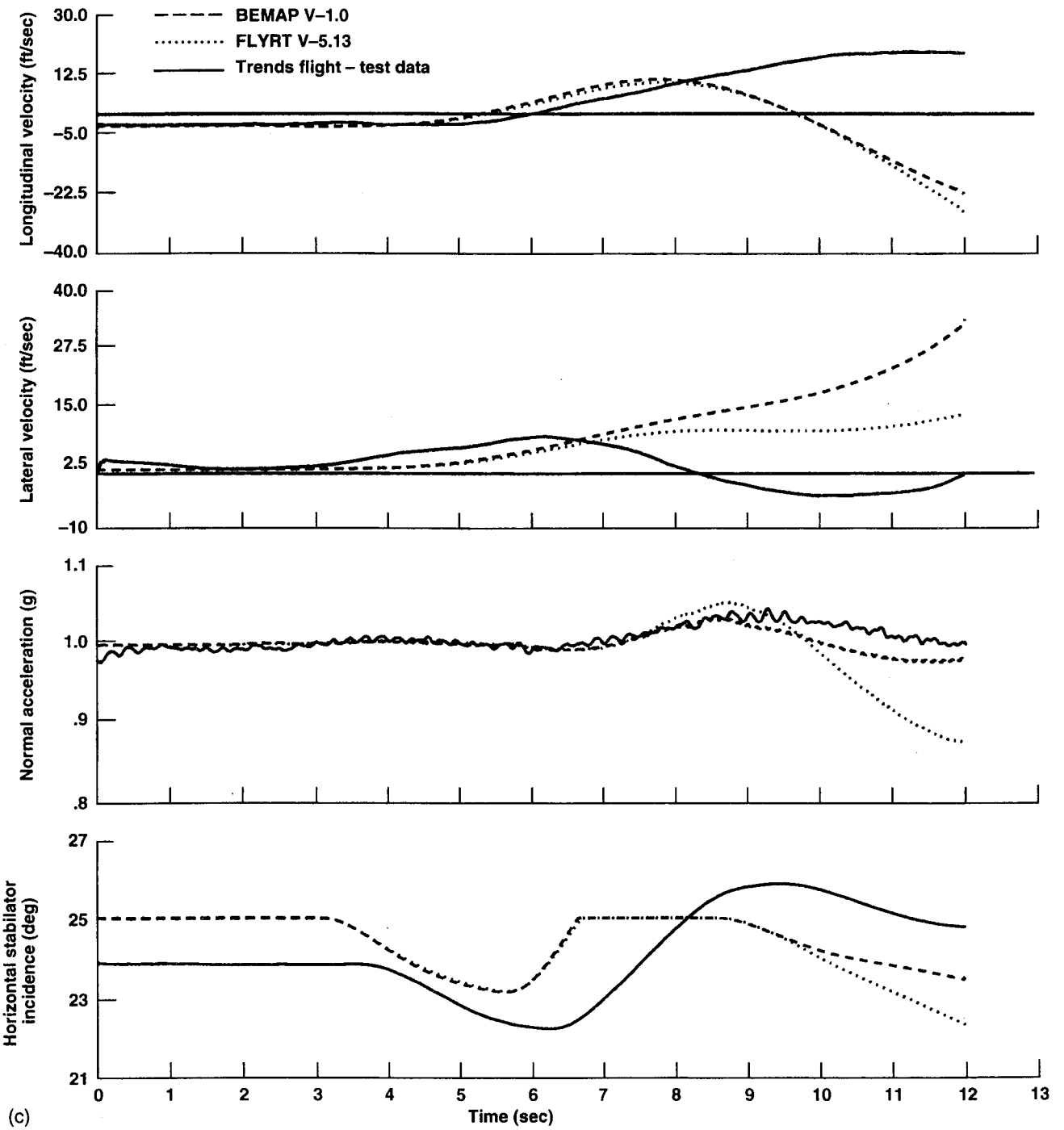


Figure 5. (c) Concluded.

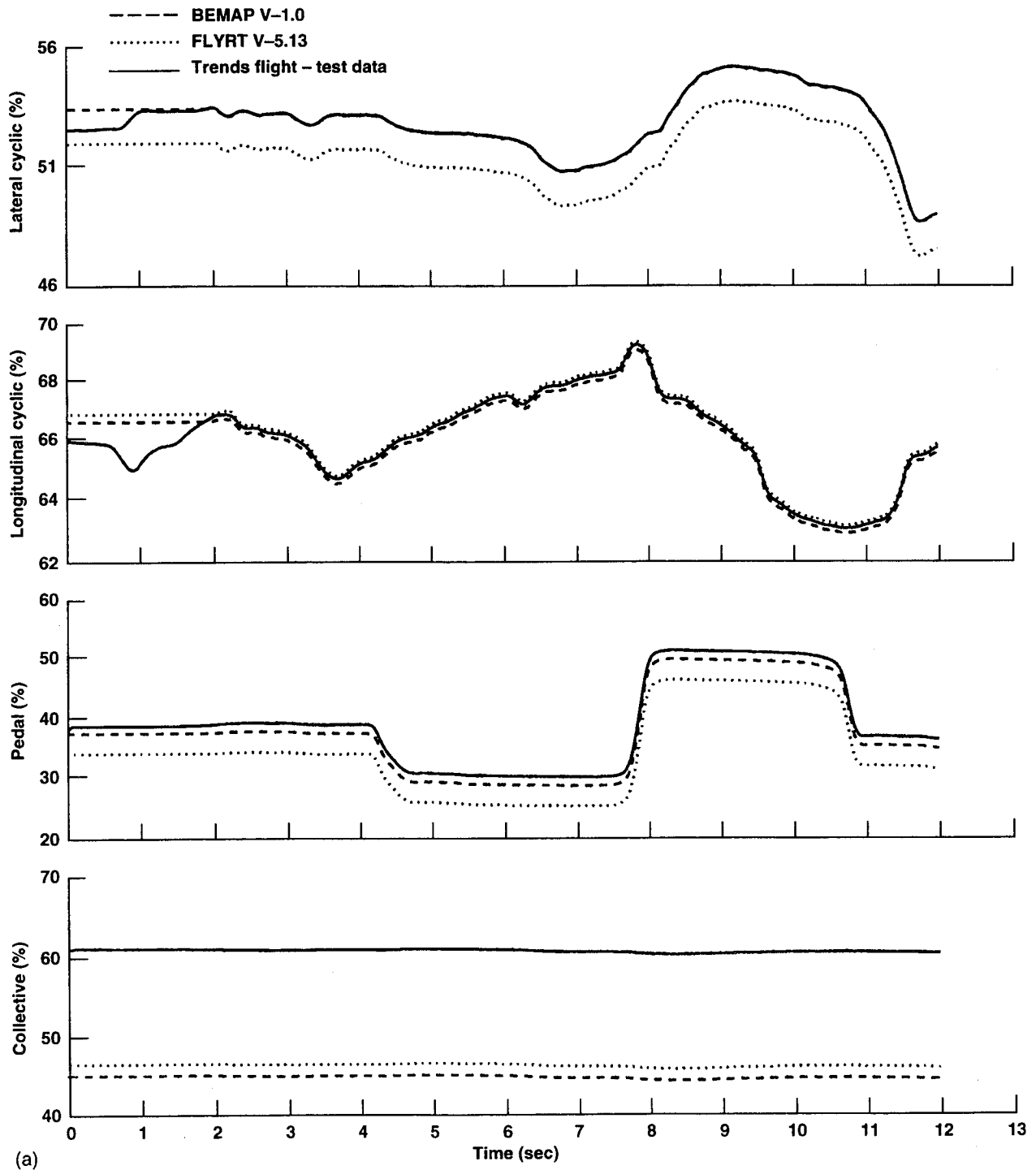


Figure 6. (a) Responses to directional doublet in hover.

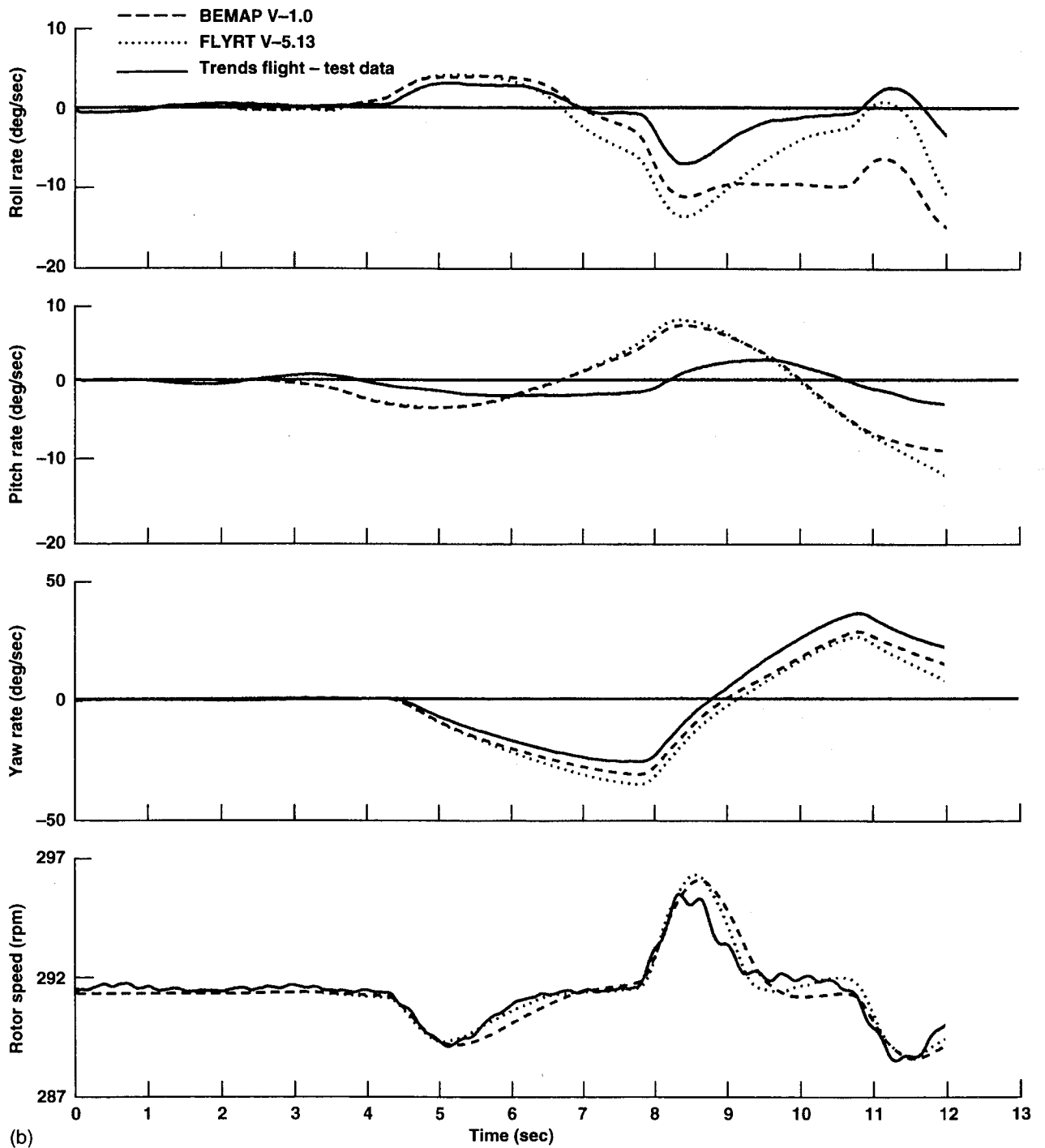


Figure 6. (b) Continued.

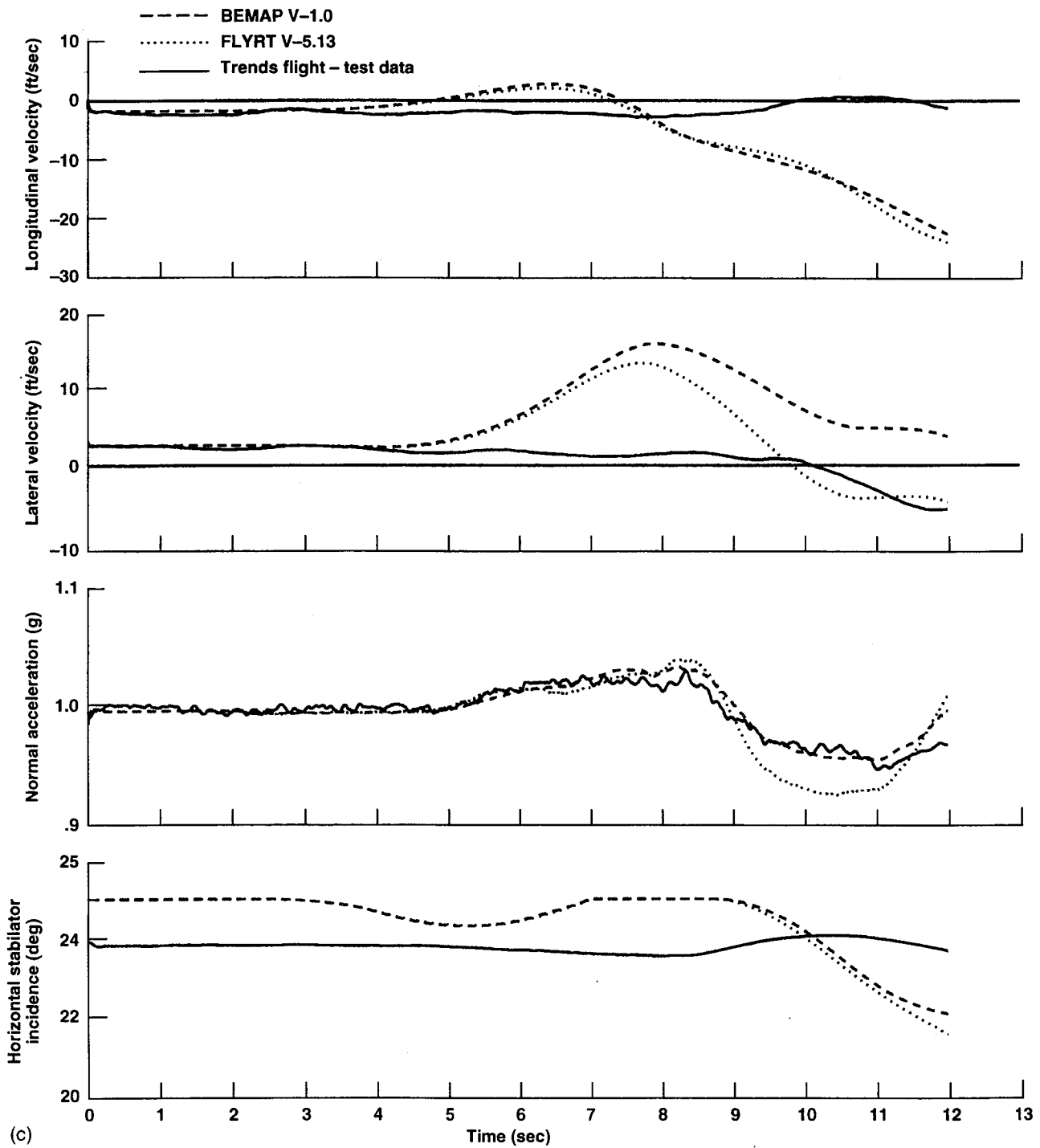


Figure 6. (c) Concluded.

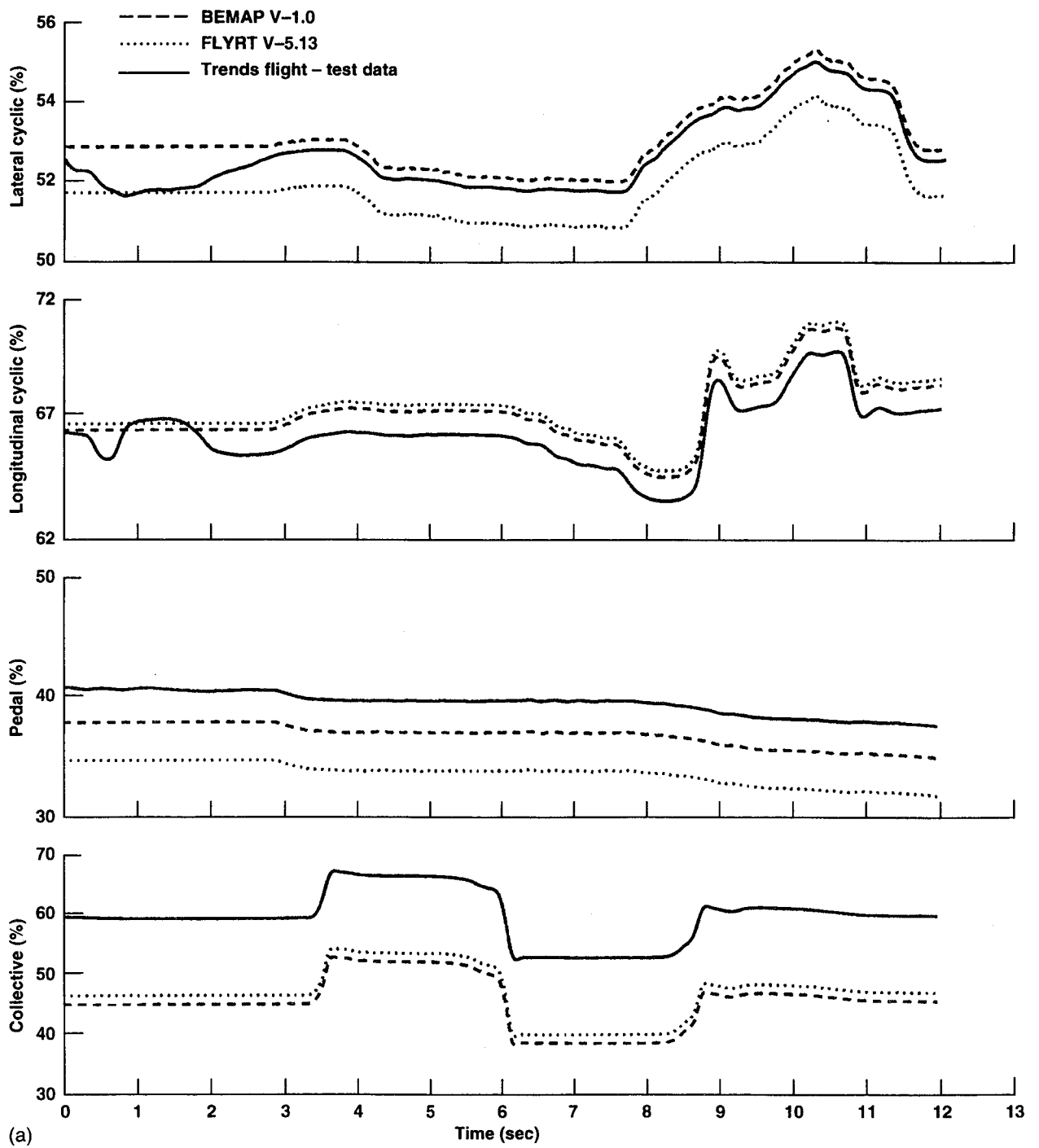


Figure 7. (a) Responses to collective doublet in hover.

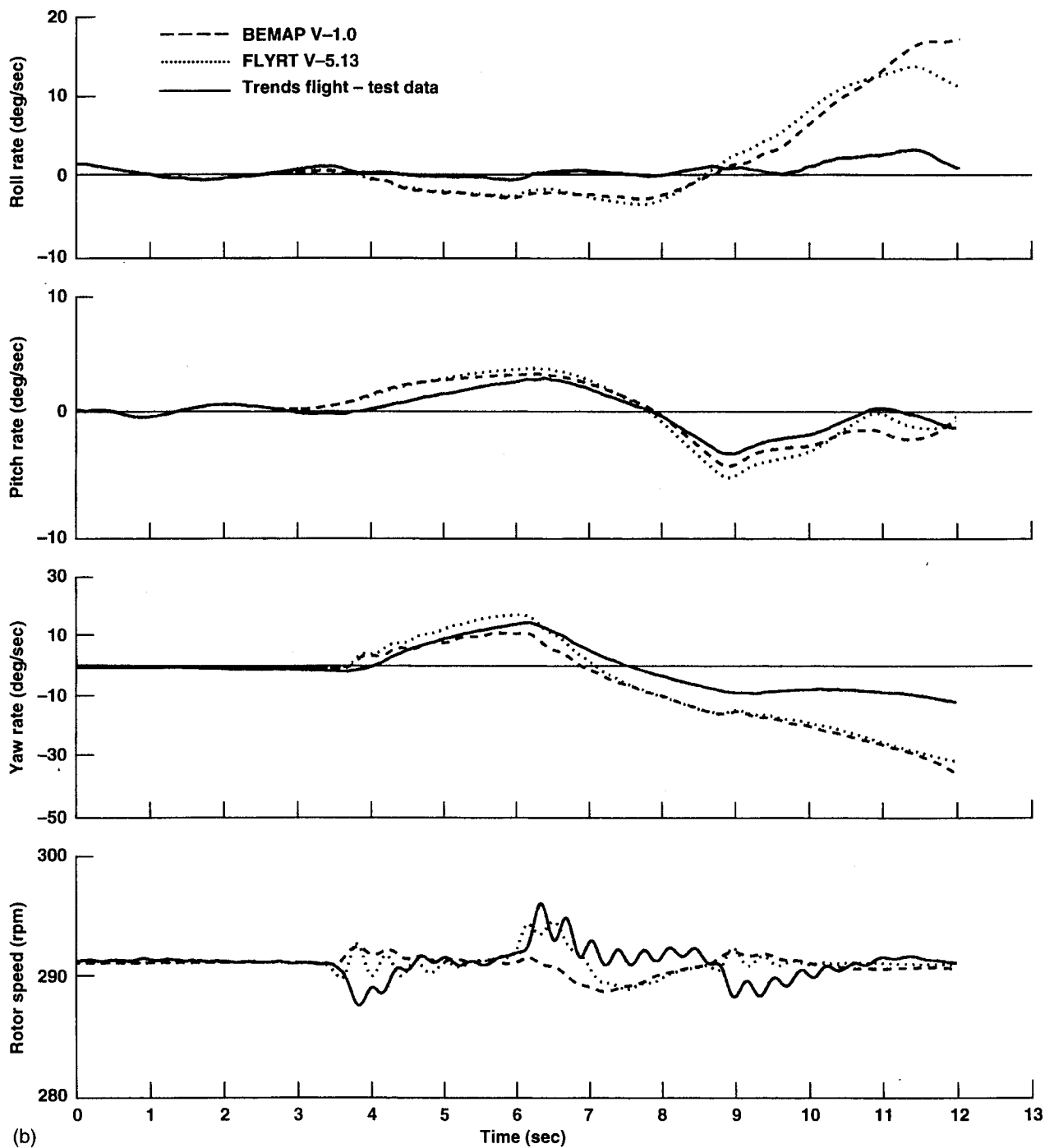


Figure 7. (b) Continued.

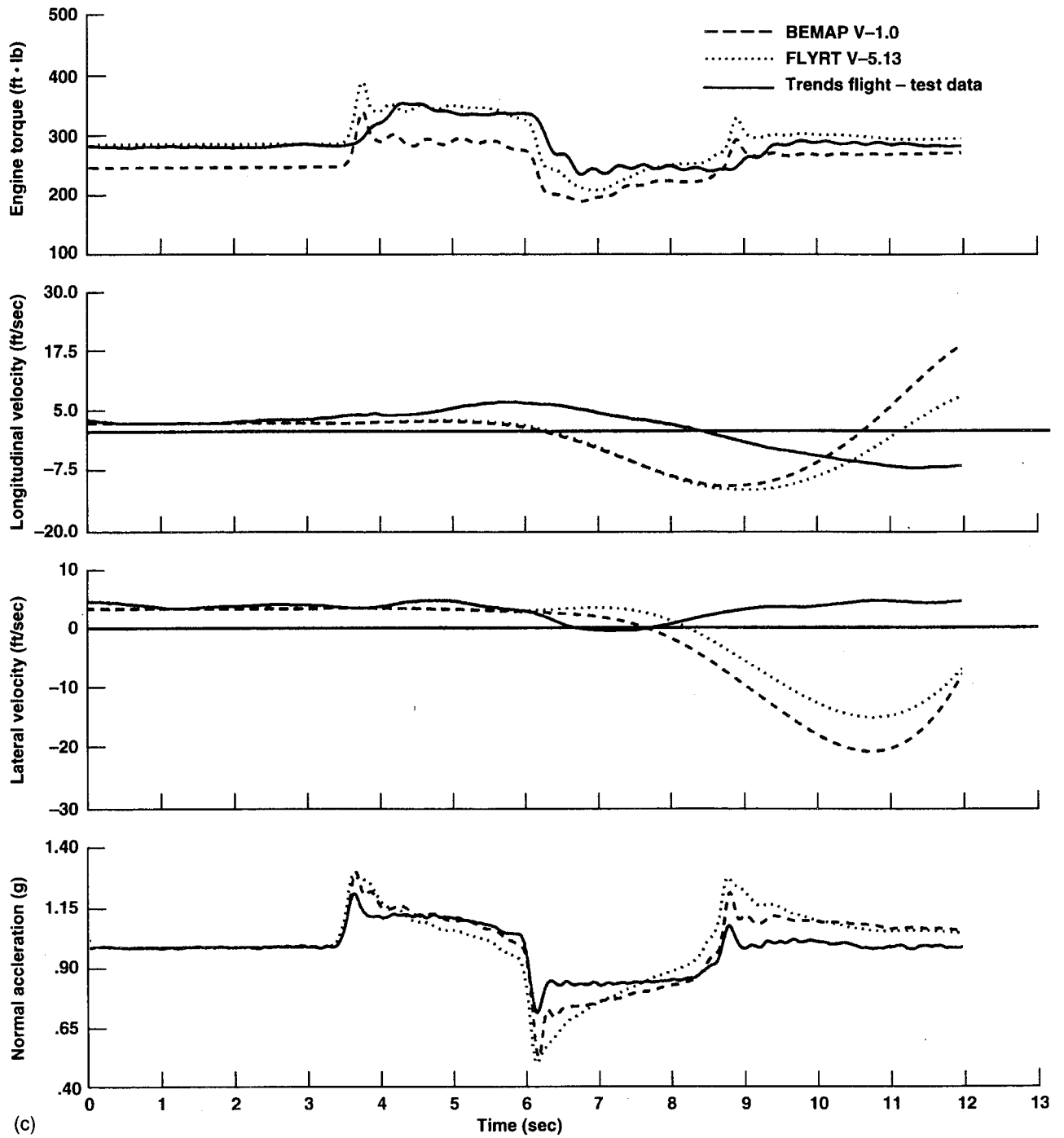


Figure 7. (c) Concluded.

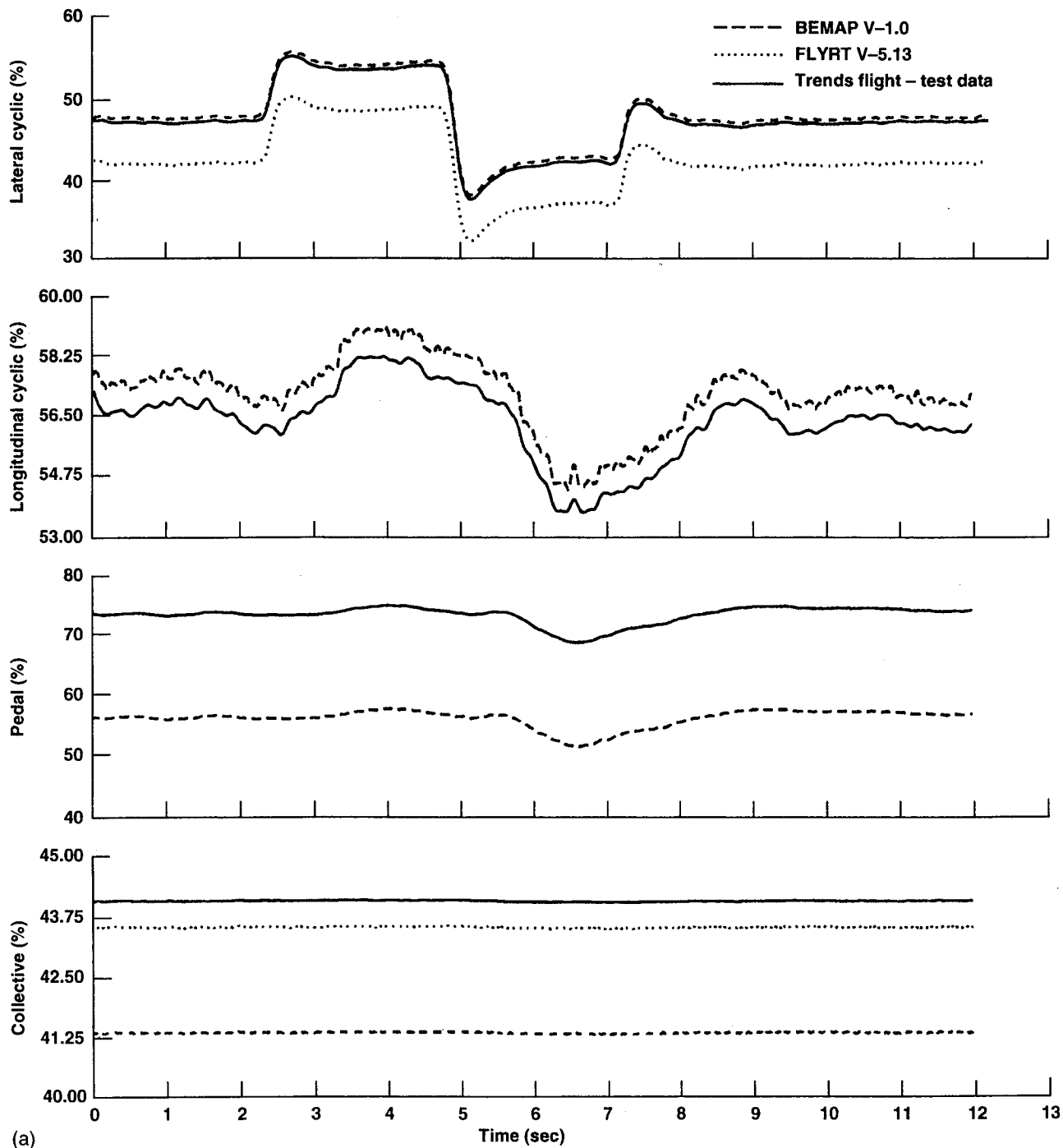


Figure 8. (a) Responses to lateral doublet at 60 kts.

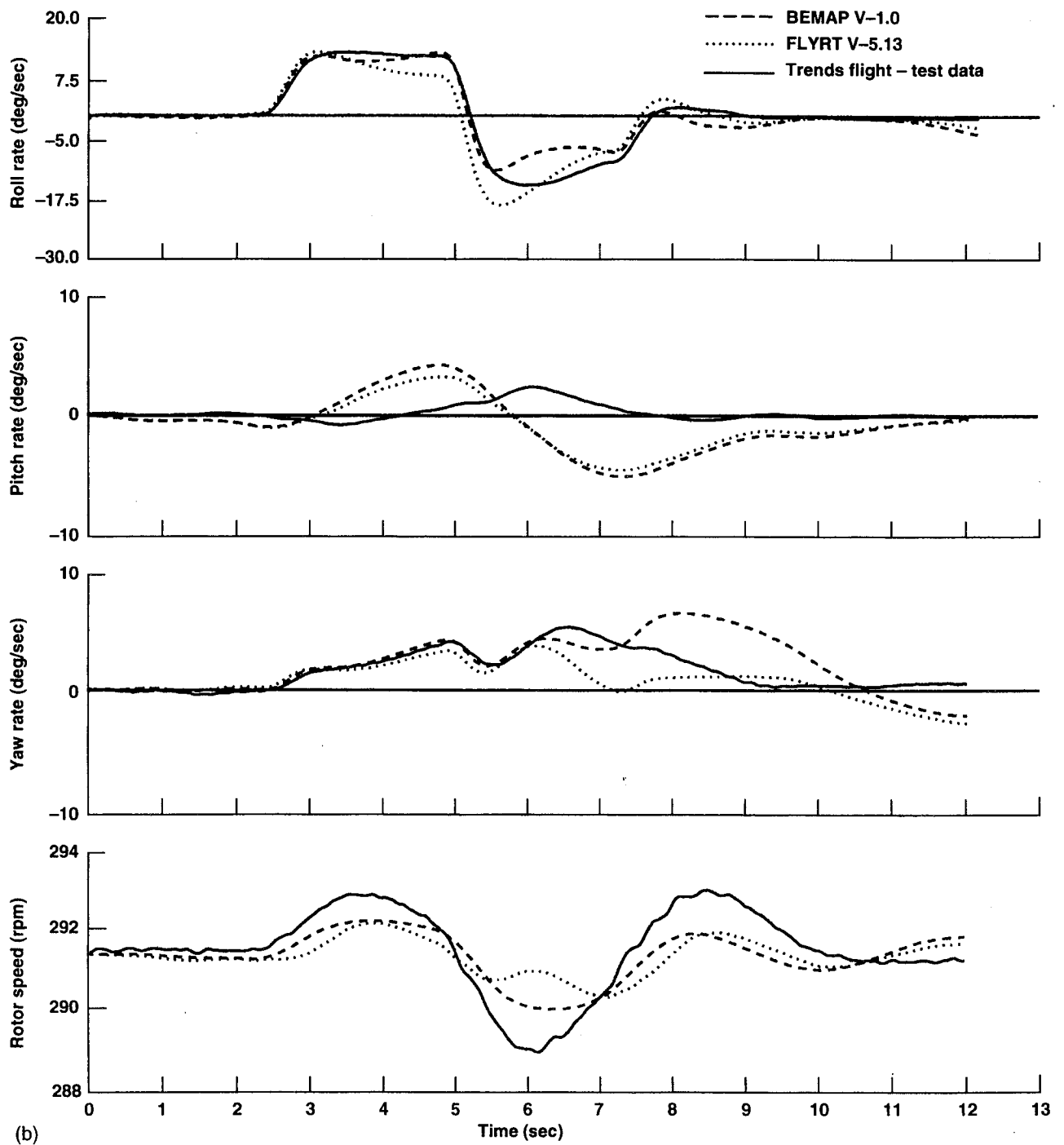


Figure 8. (b) Continued.

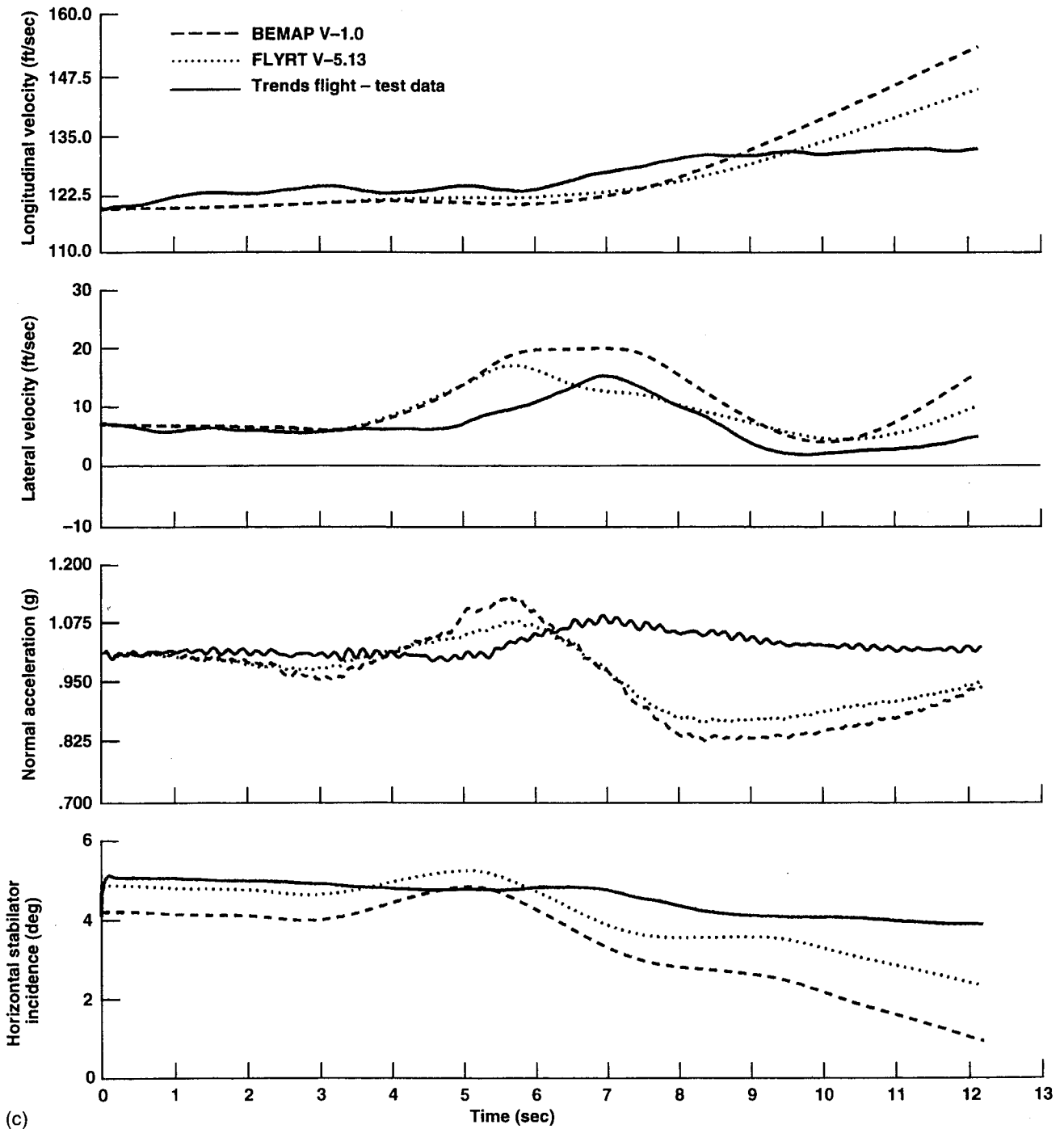


Figure 8. (c) Concluded.

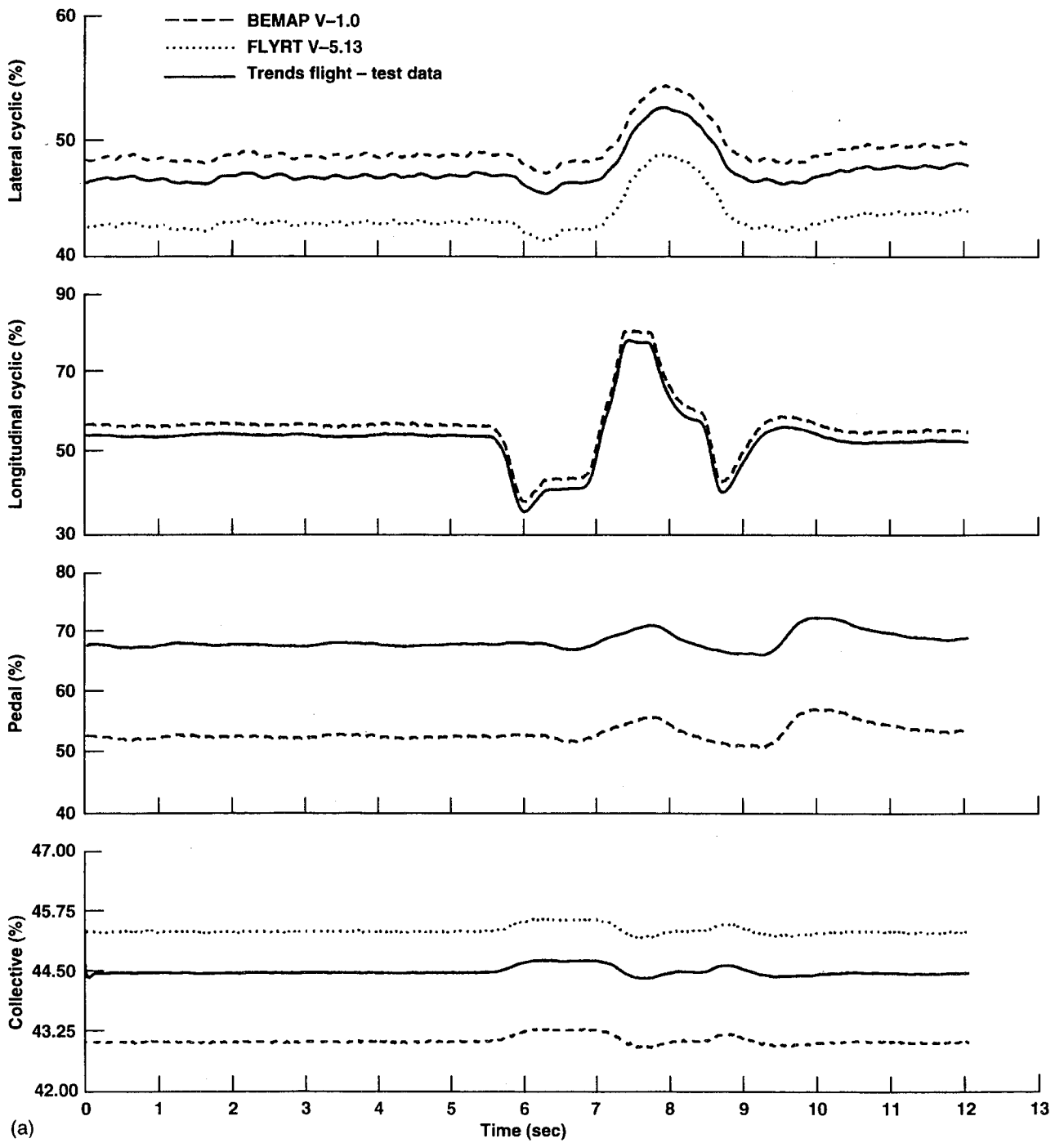


Figure 9. (a) Responses to longitudinal doublet at 60 kts.

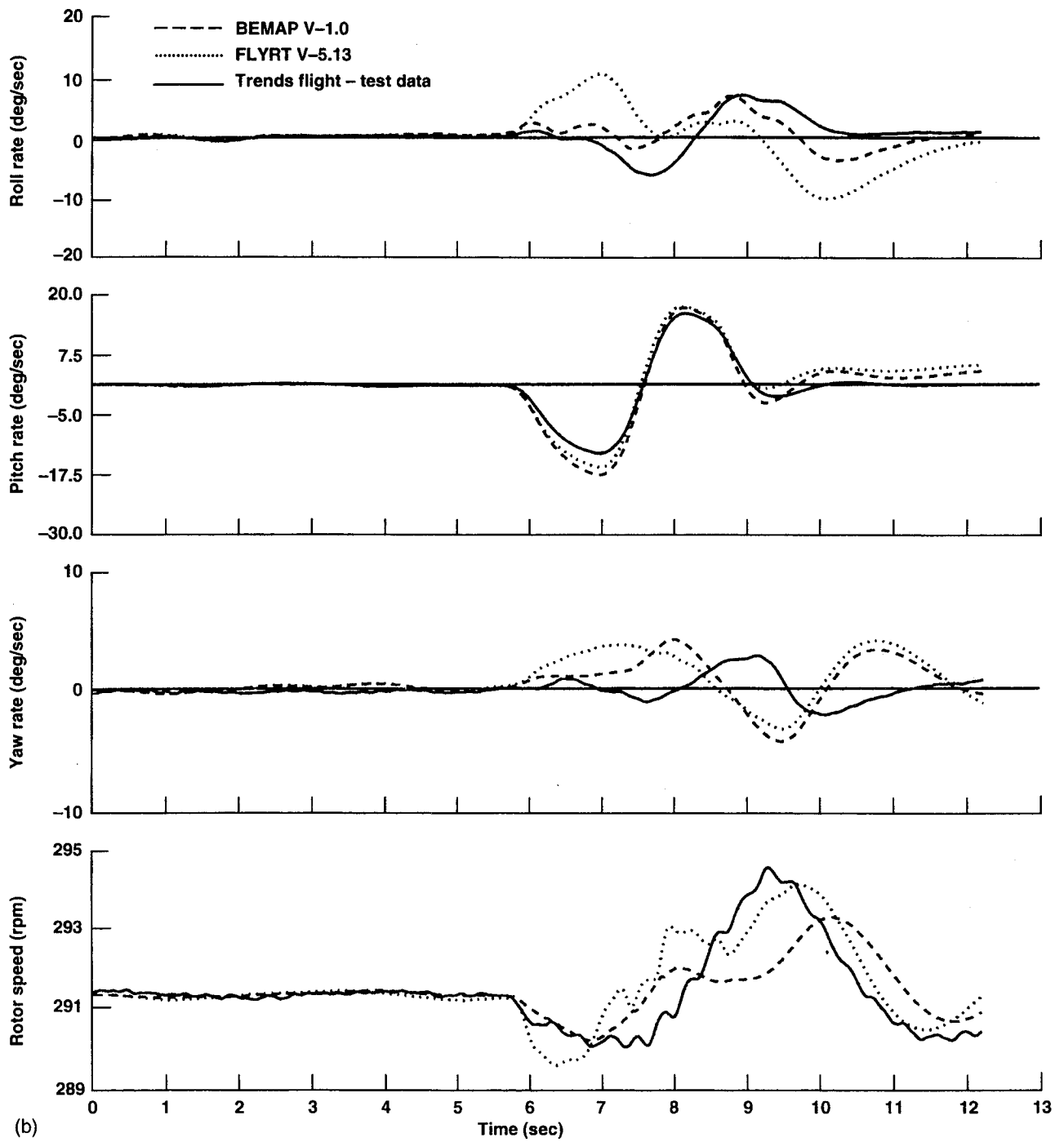


Figure 9. (b) Continued.

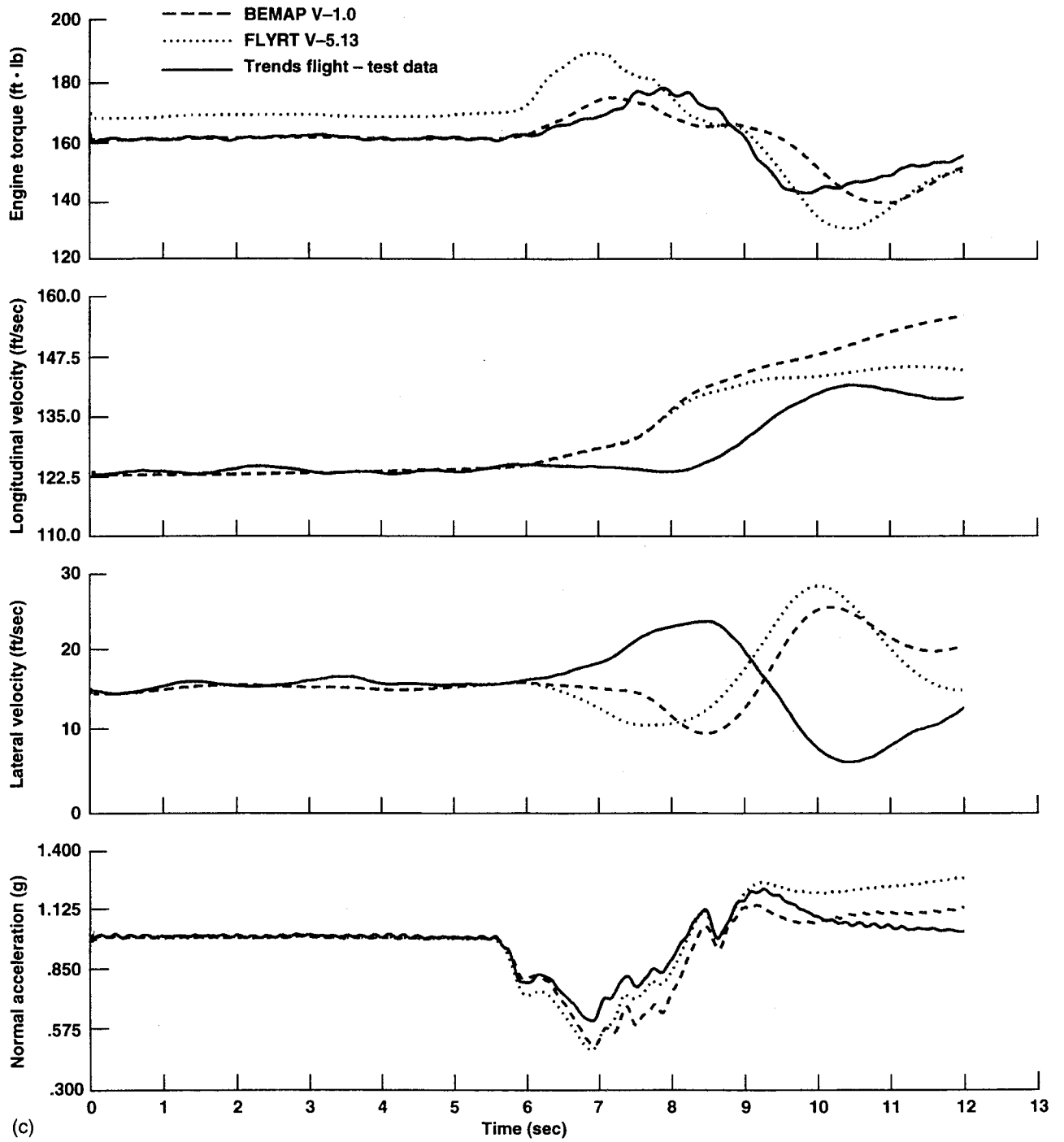


Figure 9. (c) Concluded.

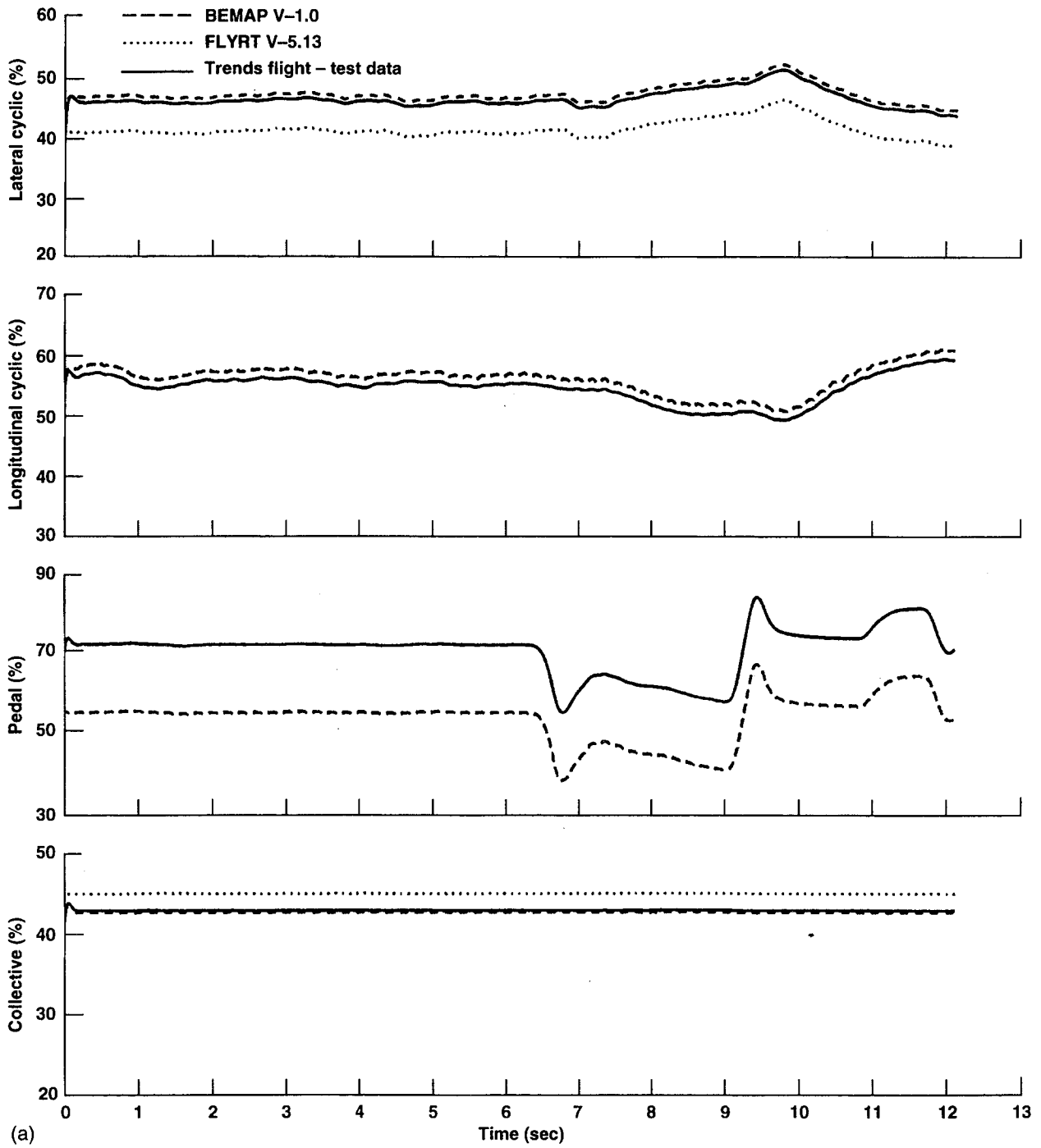
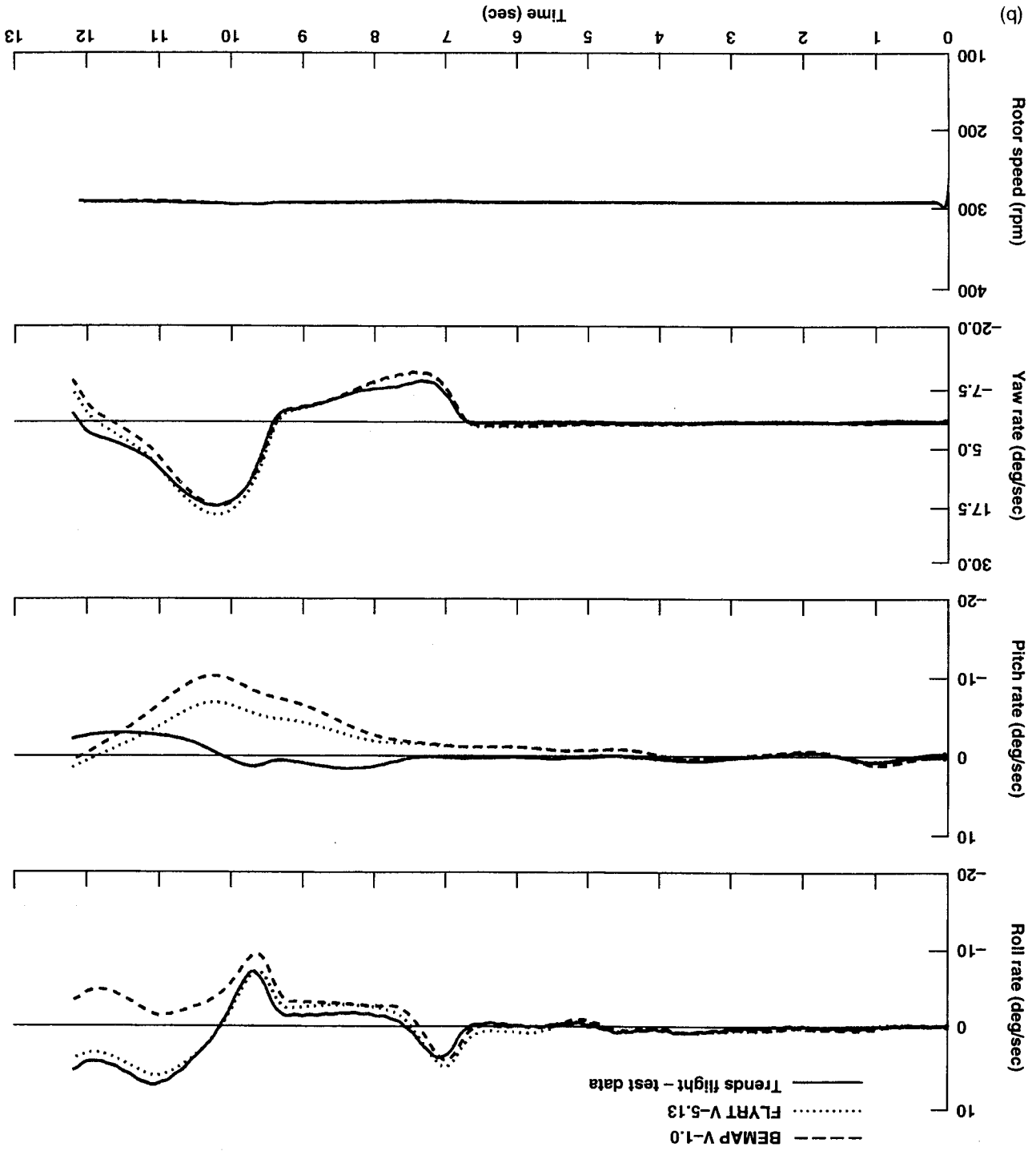


Figure 10. (a) Responses to directional doublet at 60 kts.

Figure 10. (b) Continued.



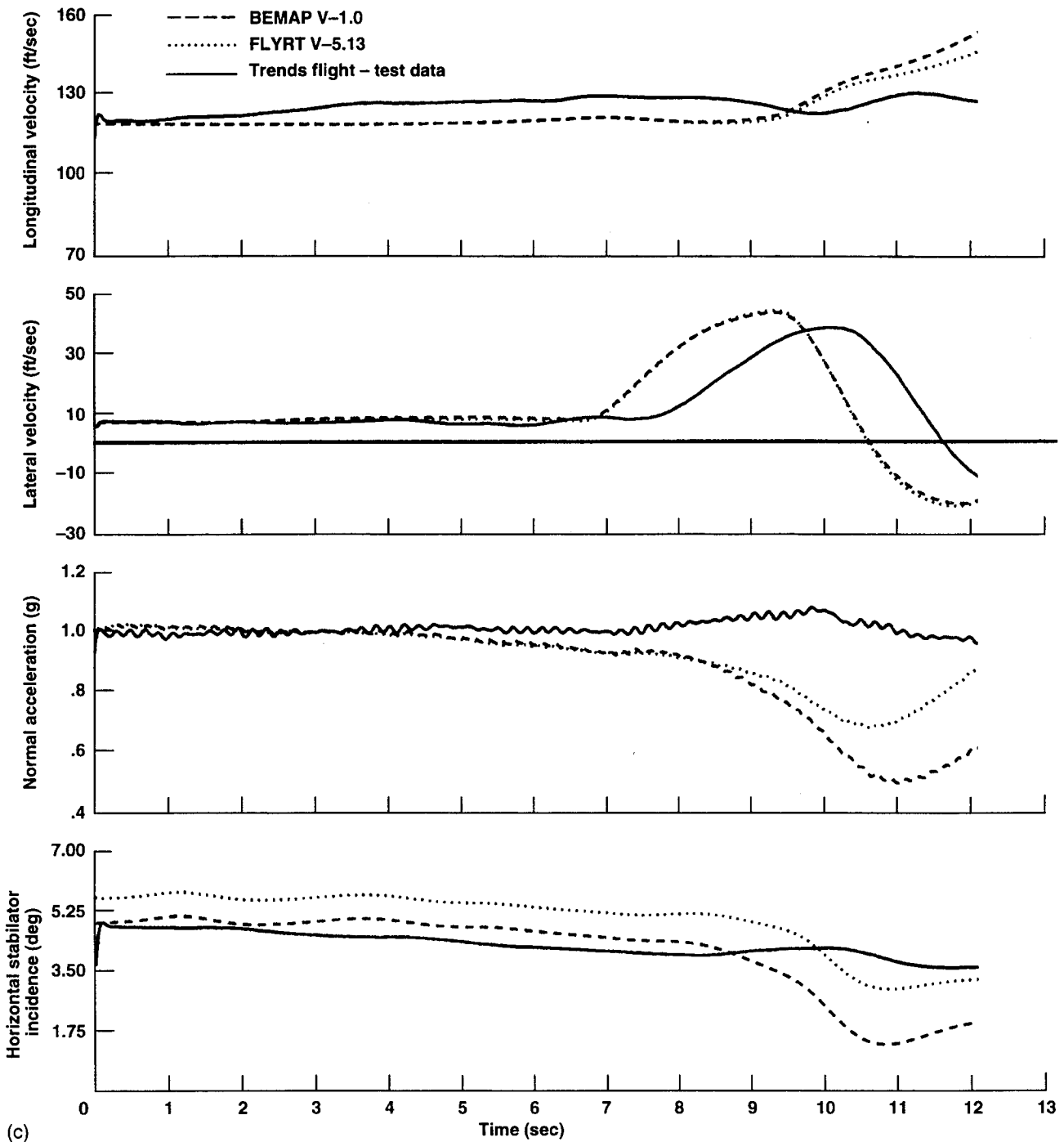


Figure 10. (c) Concluded.

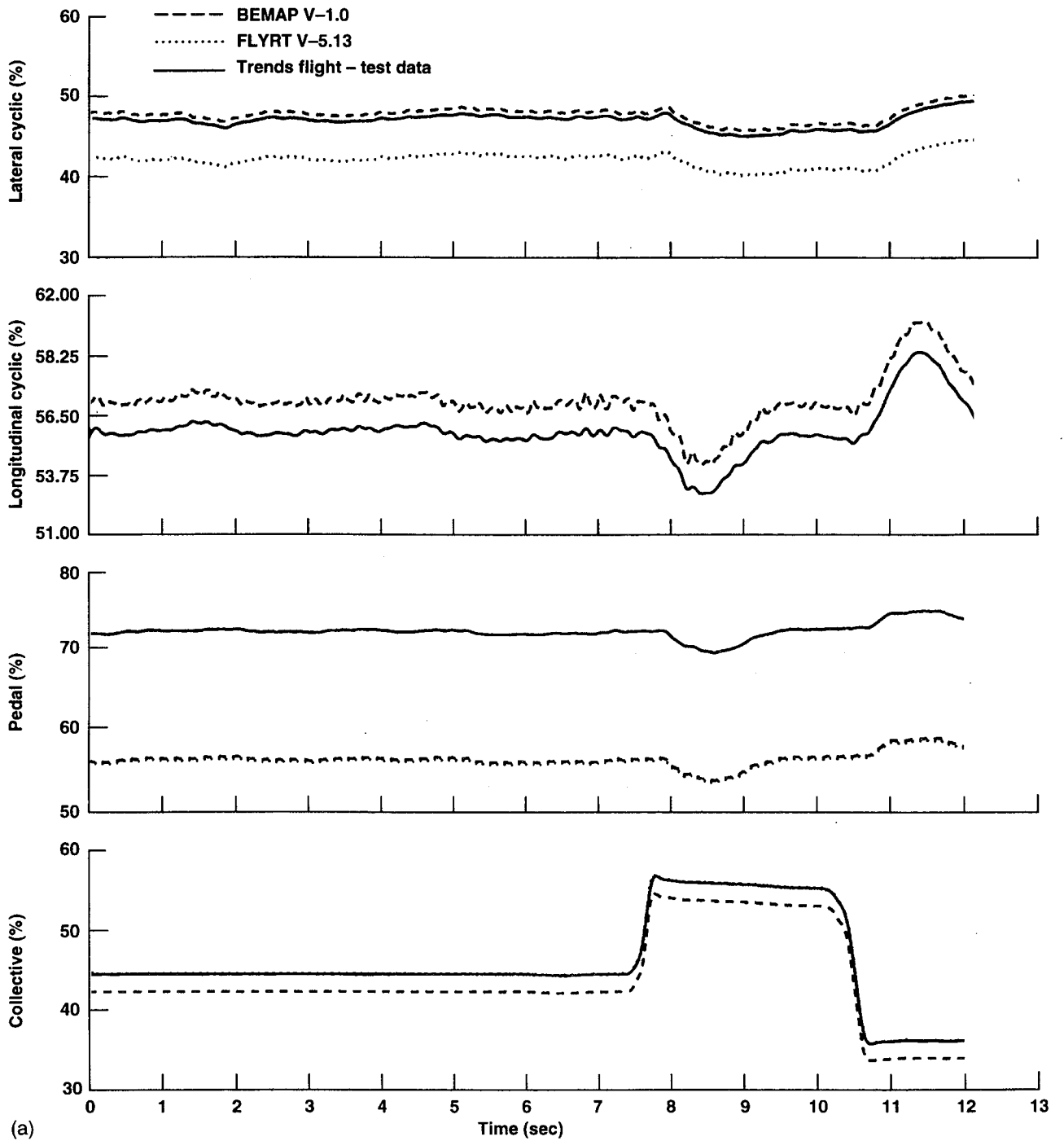


Figure 11. (a) Responses to collective doublet at 60 kts.

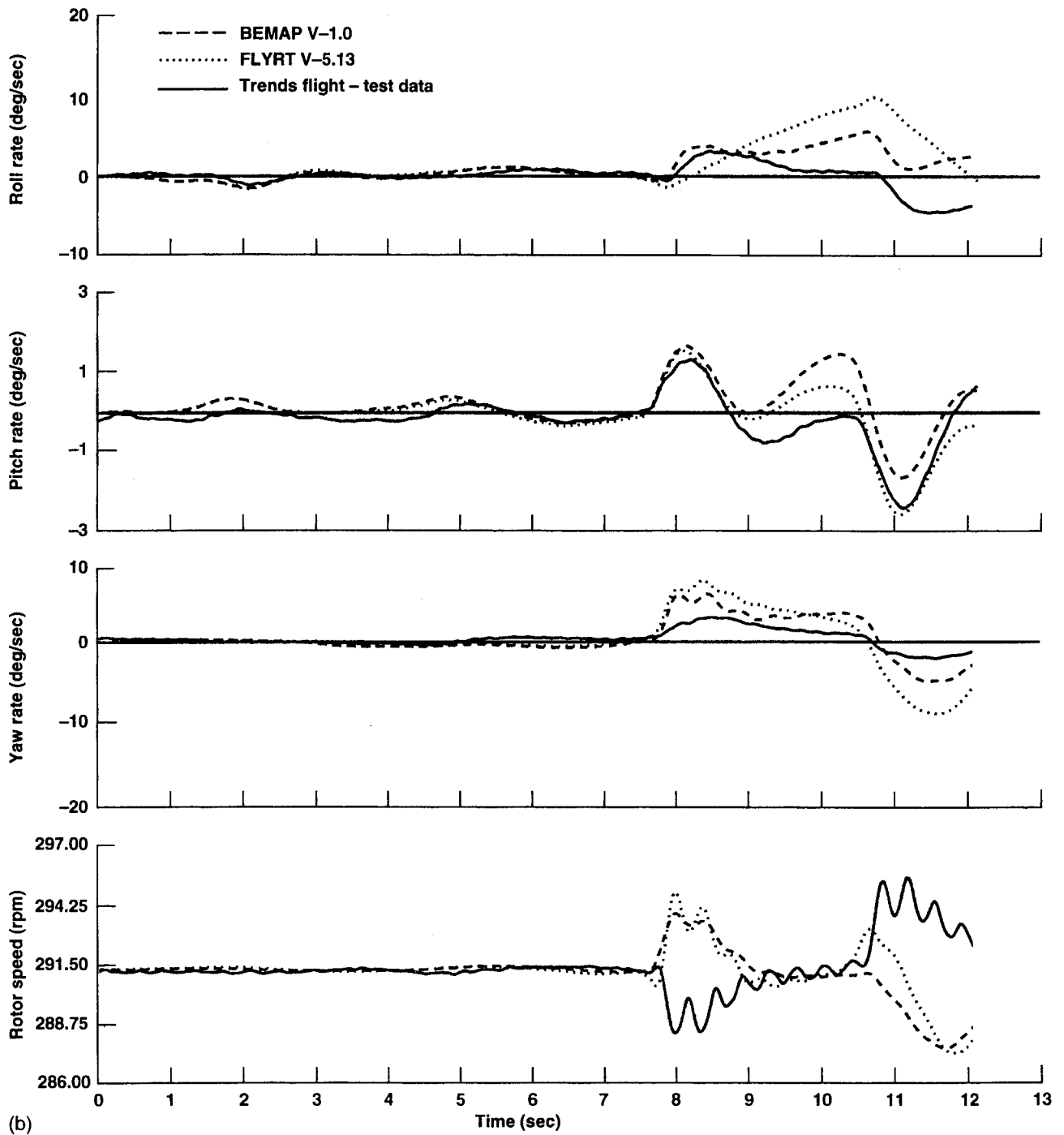
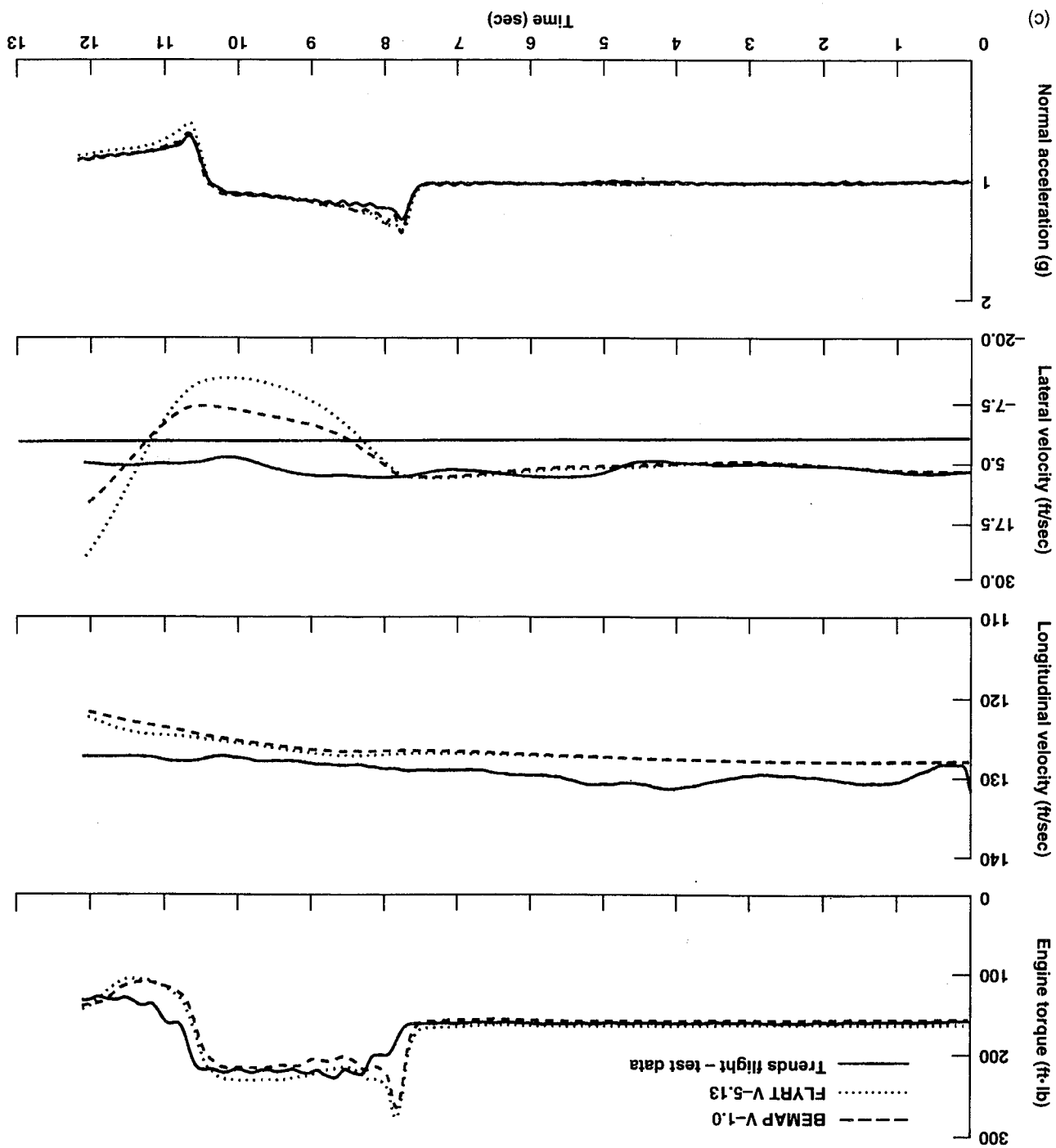


Figure 11. (b) Continued.

Figure 11. (c) Concluded.



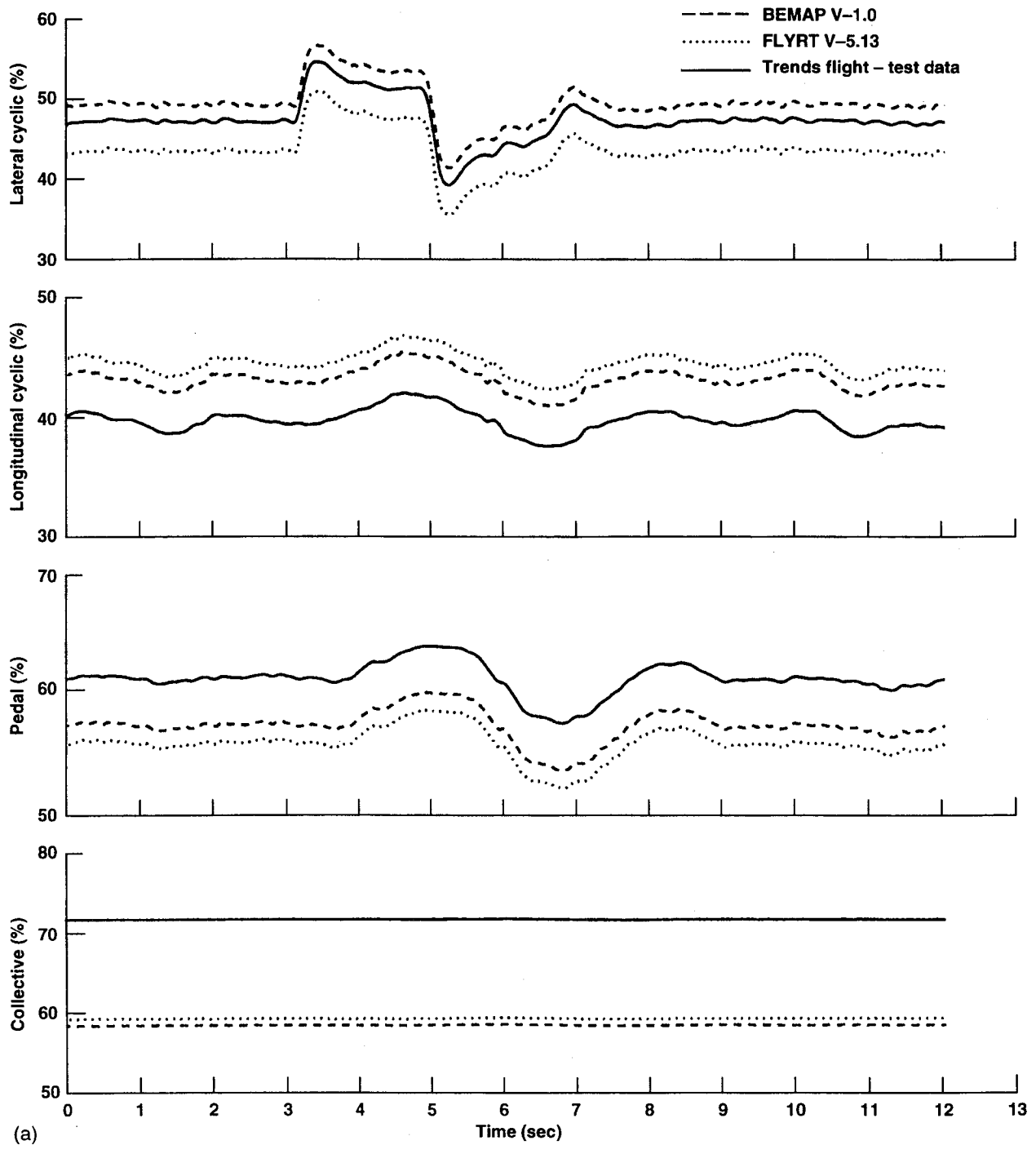


Figure 12. (a) Responses to lateral doublet at 120 kts.

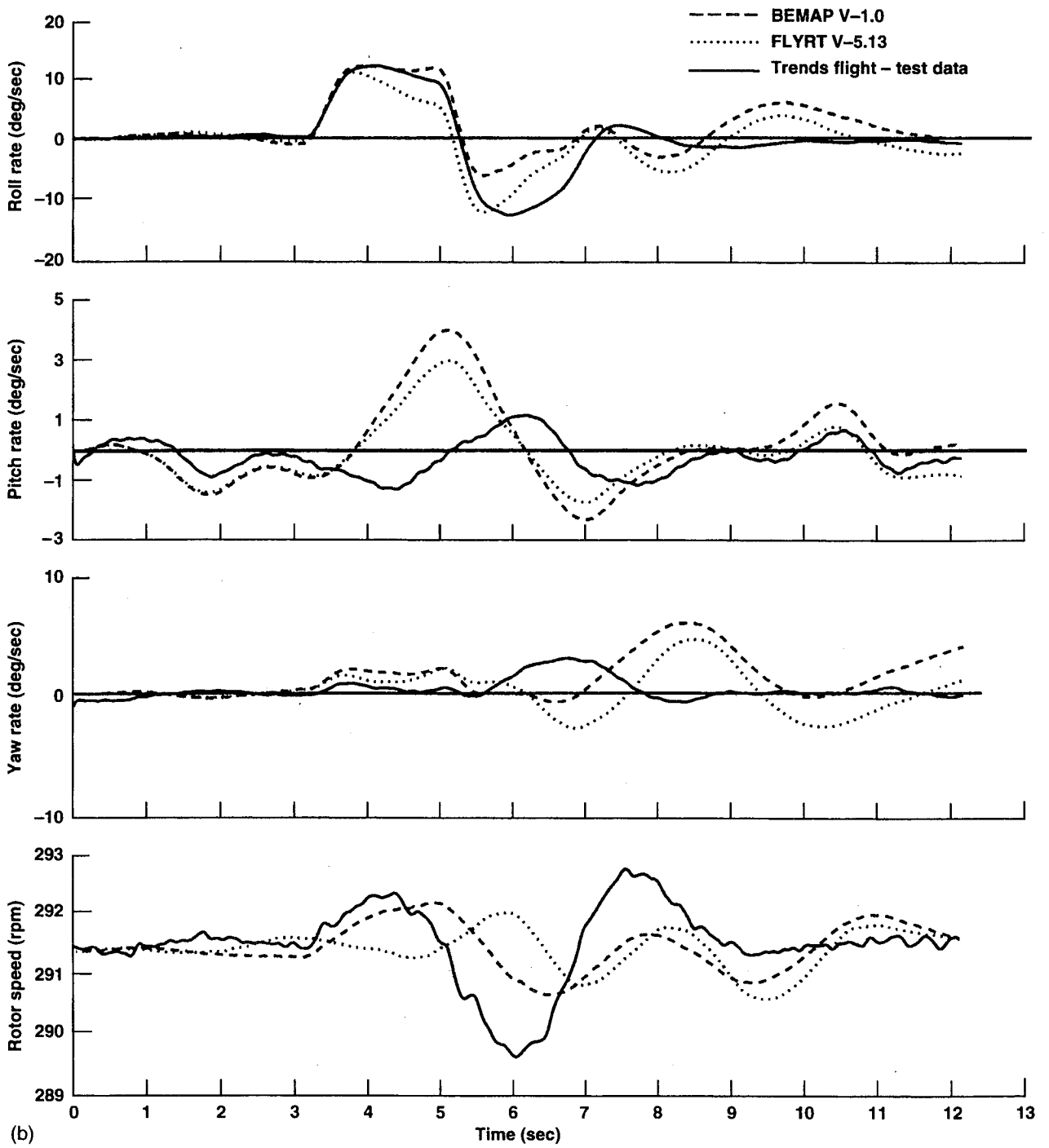


Figure 12. (b) Continued.

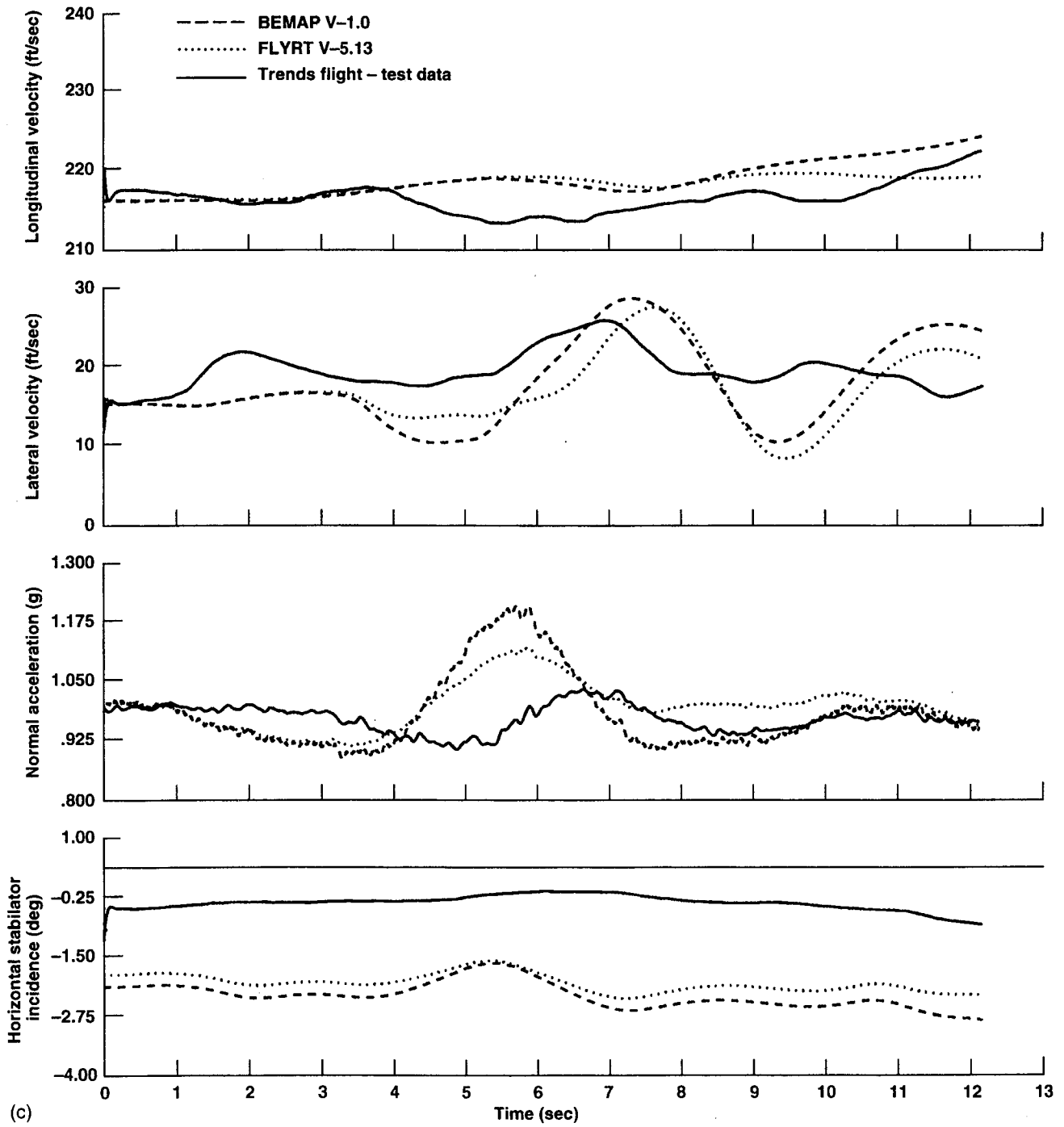


Figure 12. (c) Concluded.

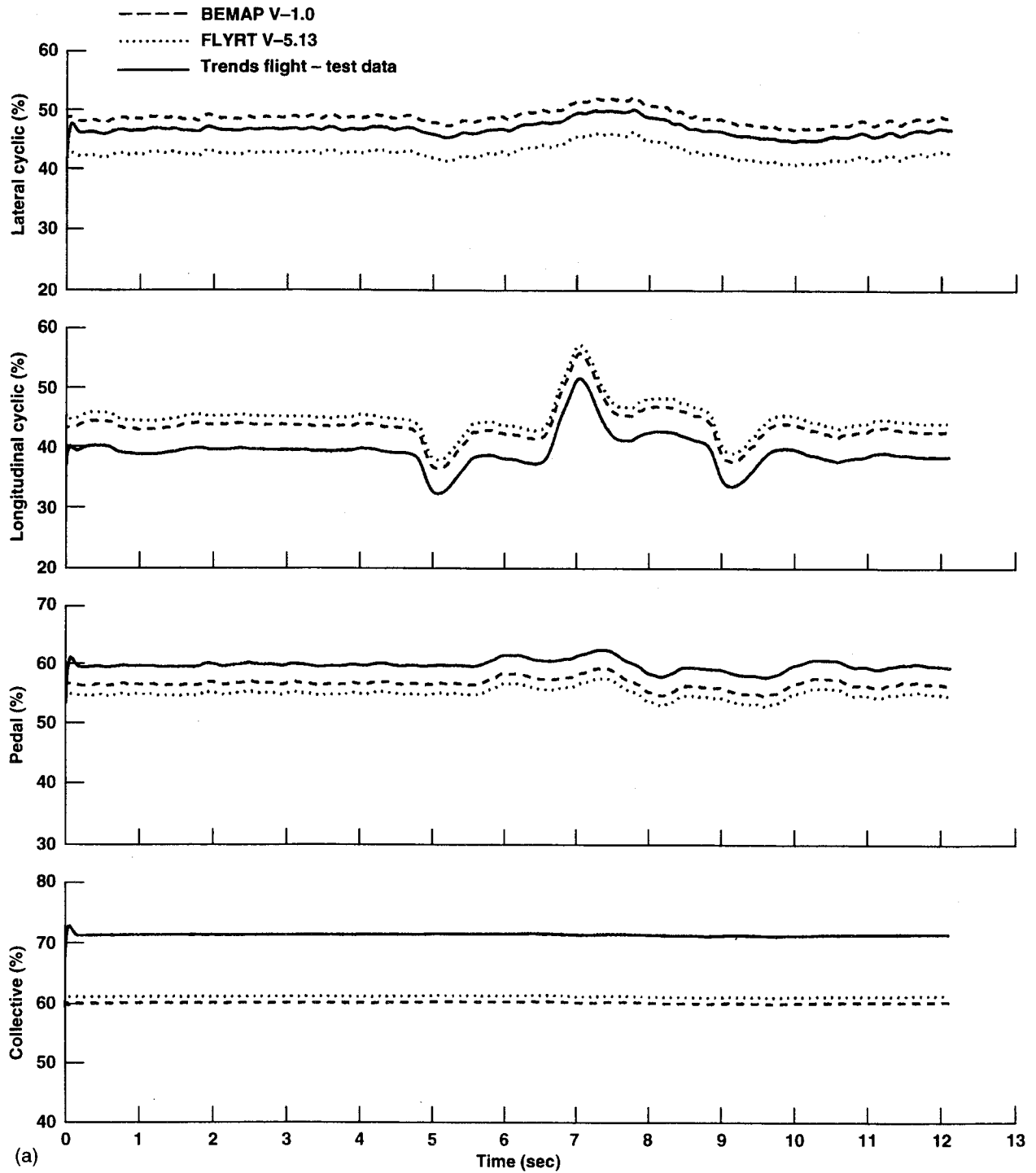


Figure 13. (a) Responses to longitudinal doublet at 120 kts.

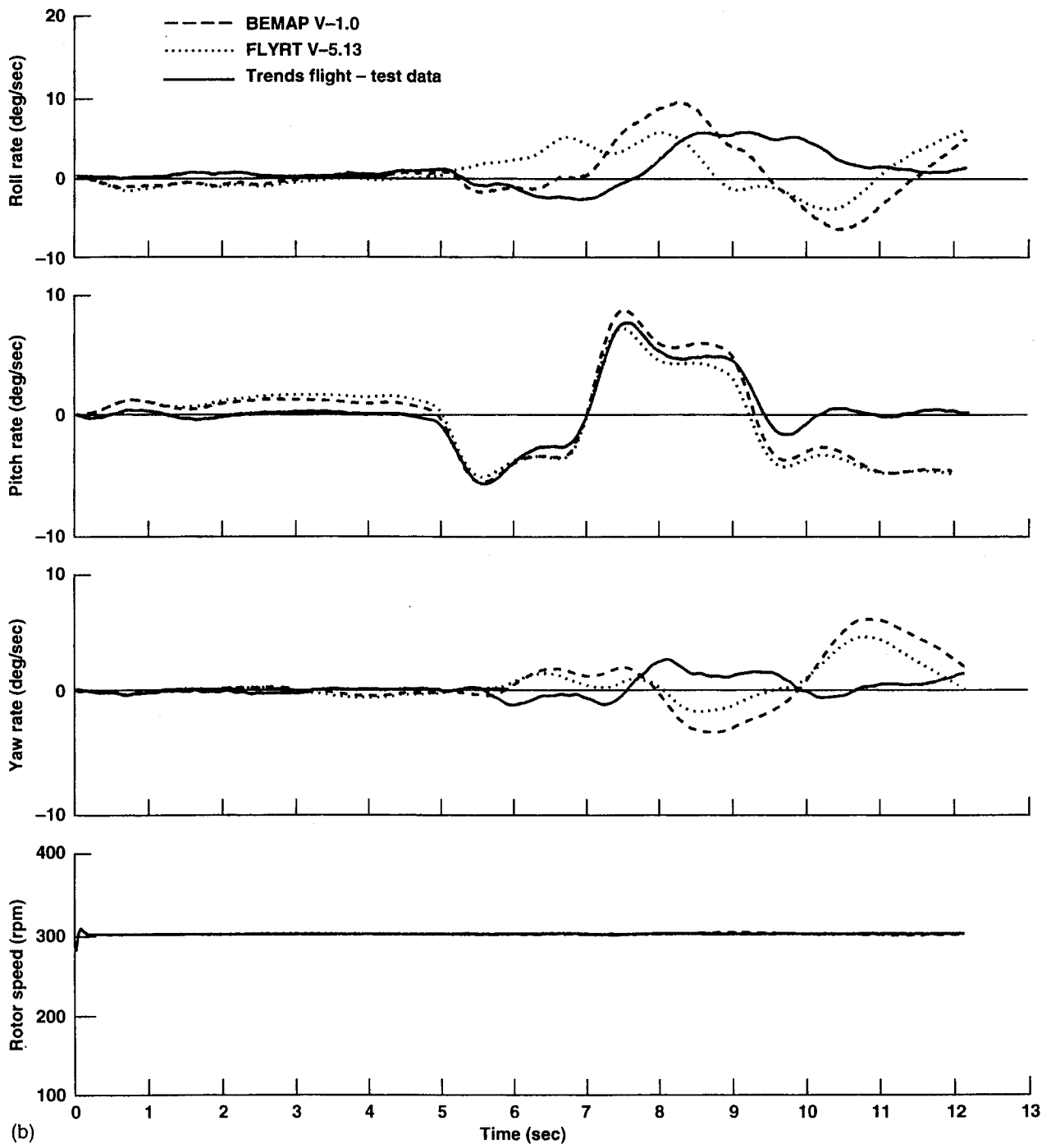


Figure 13. (b) Continued.

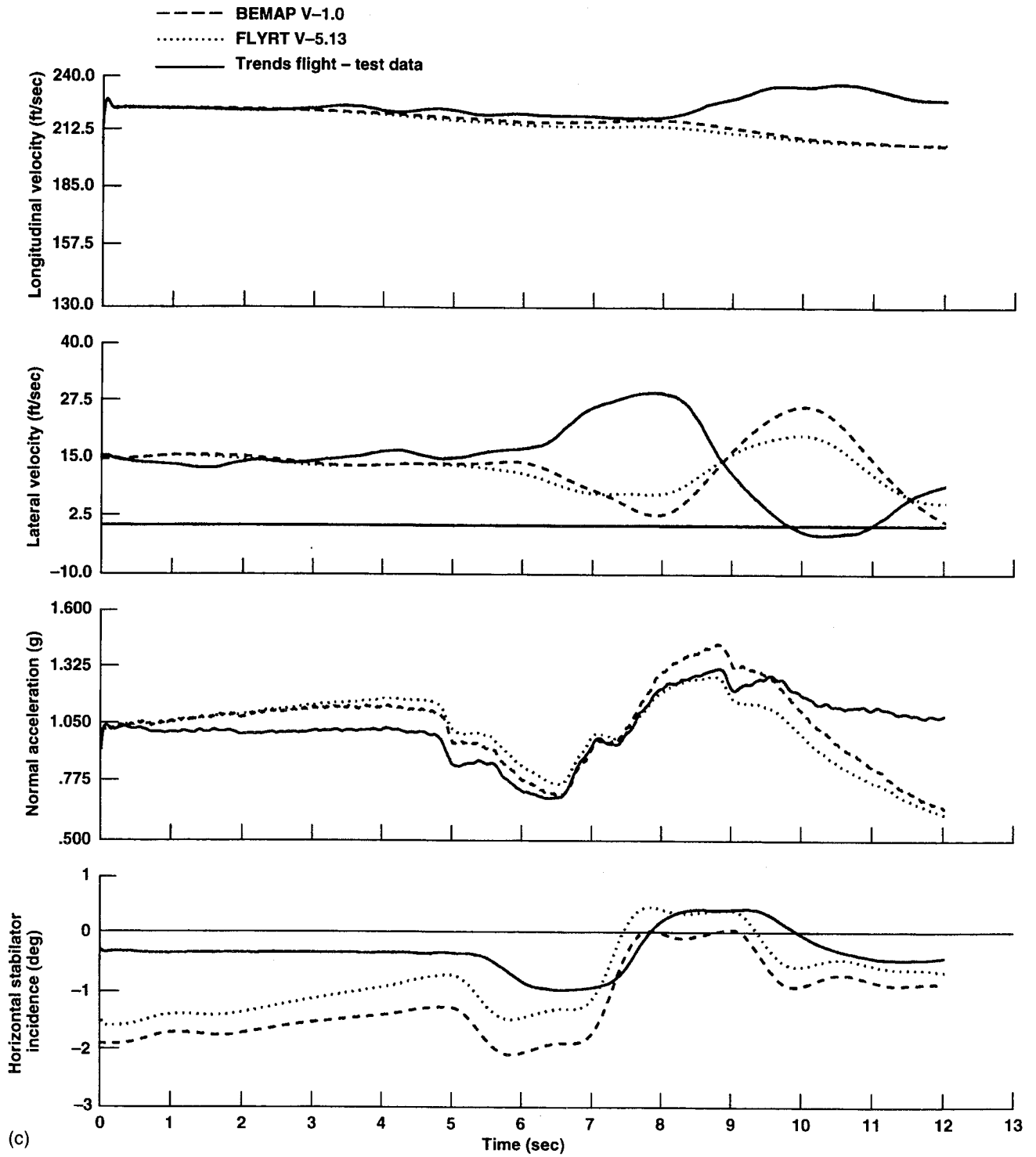


Figure 13. (c) Concluded.

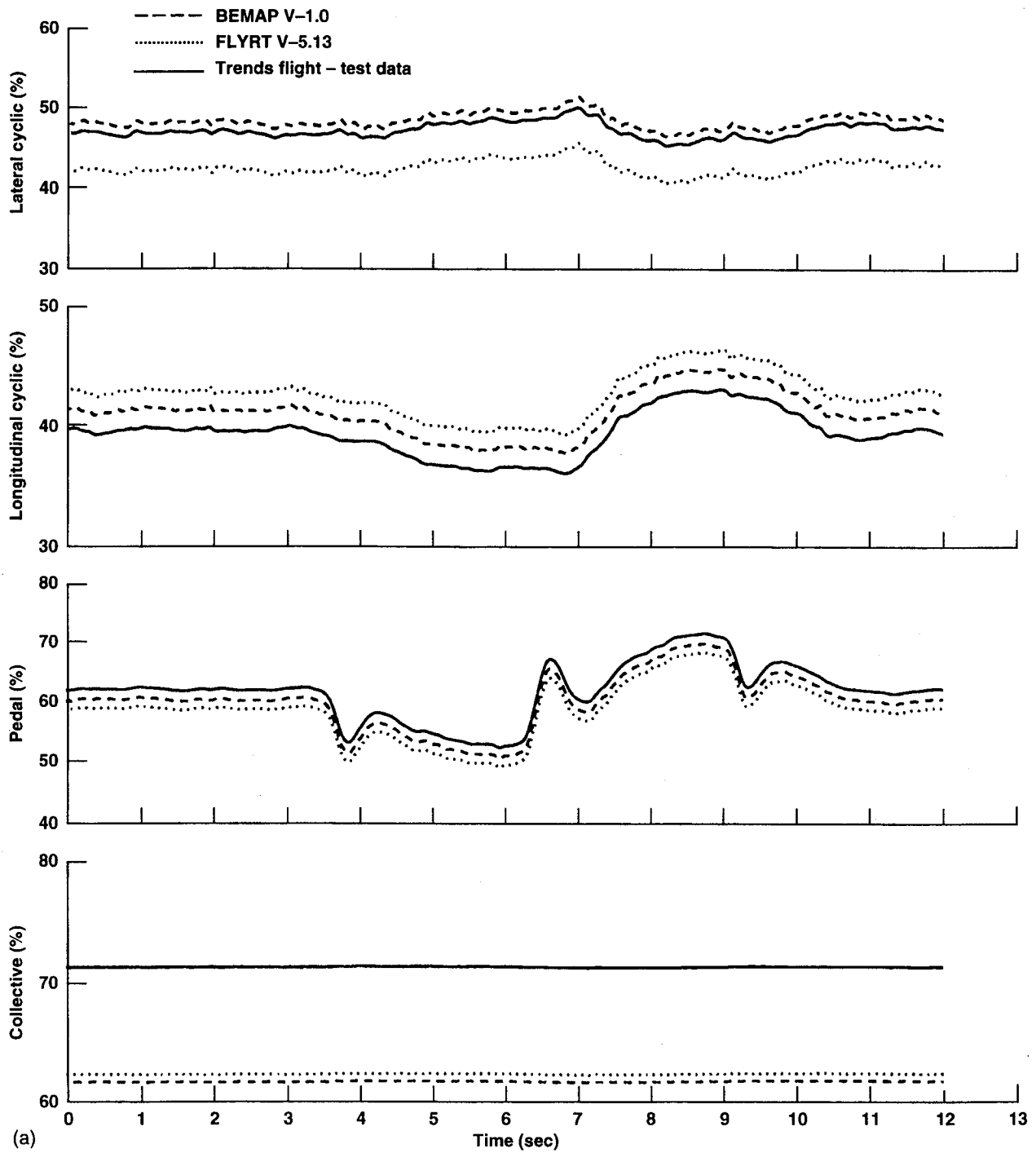


Figure 14. (a) Responses to directional doublet at 120 kts.

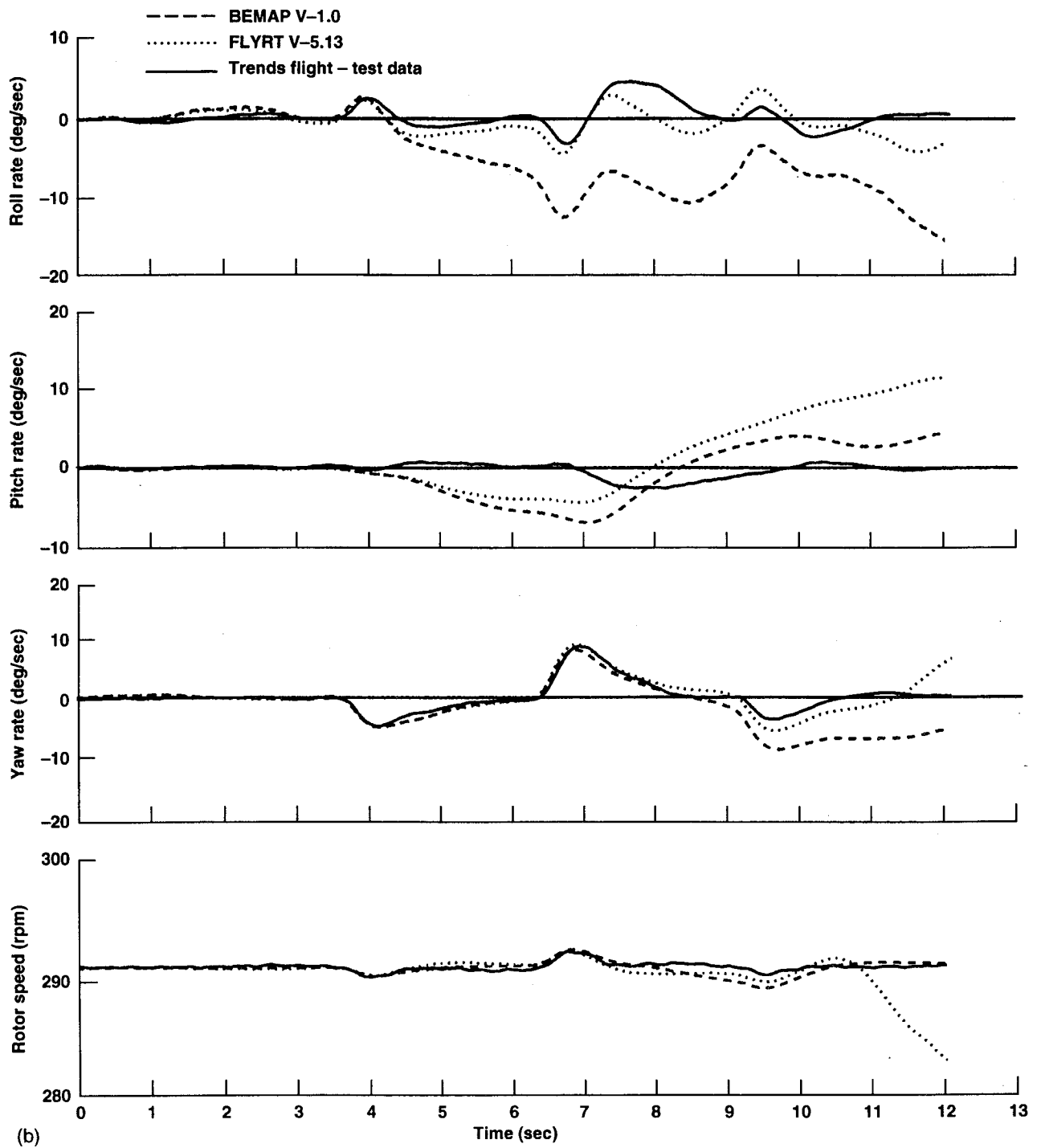


Figure 14. (b) Continued.

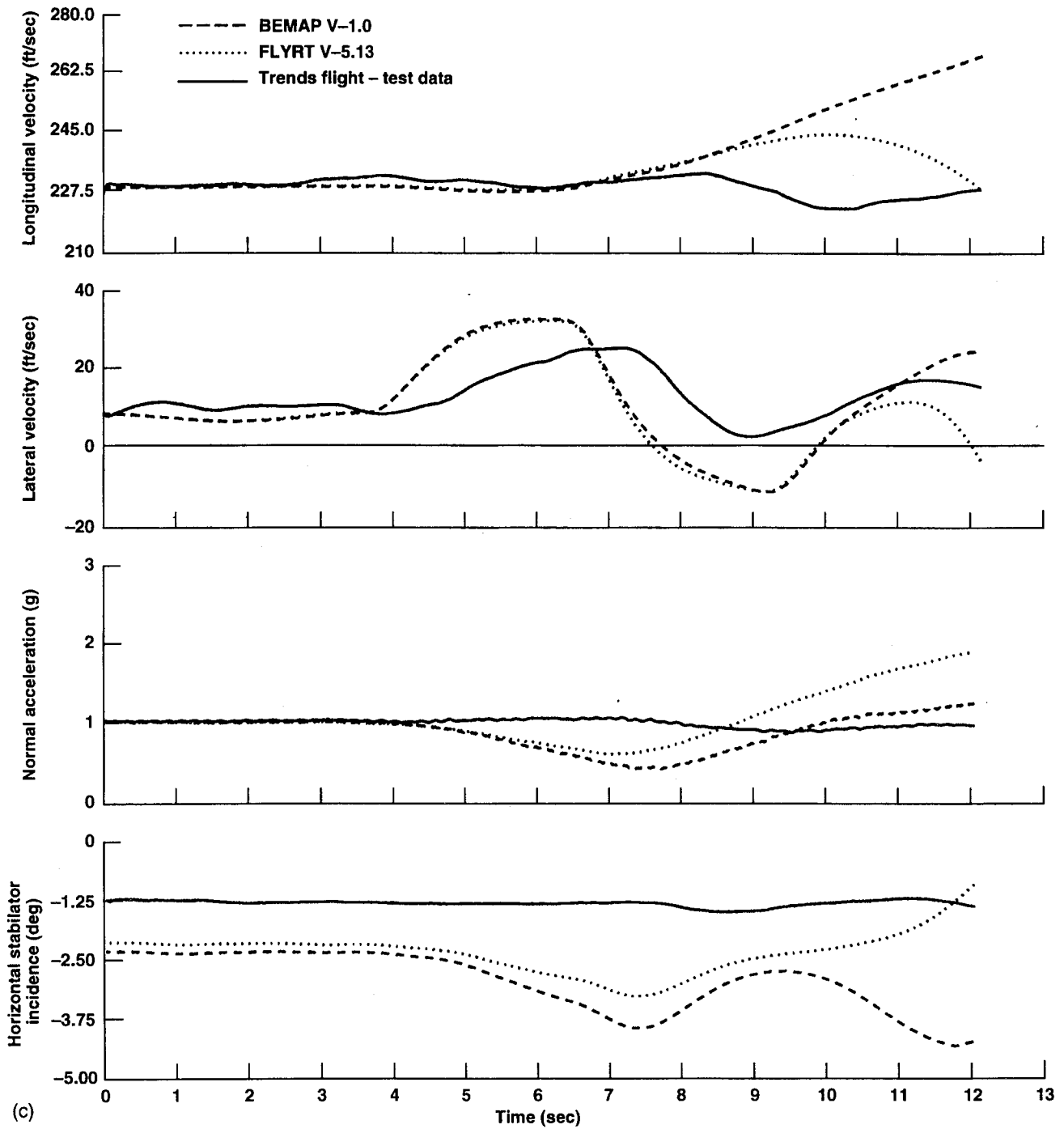


Figure 14. (c) Concluded.

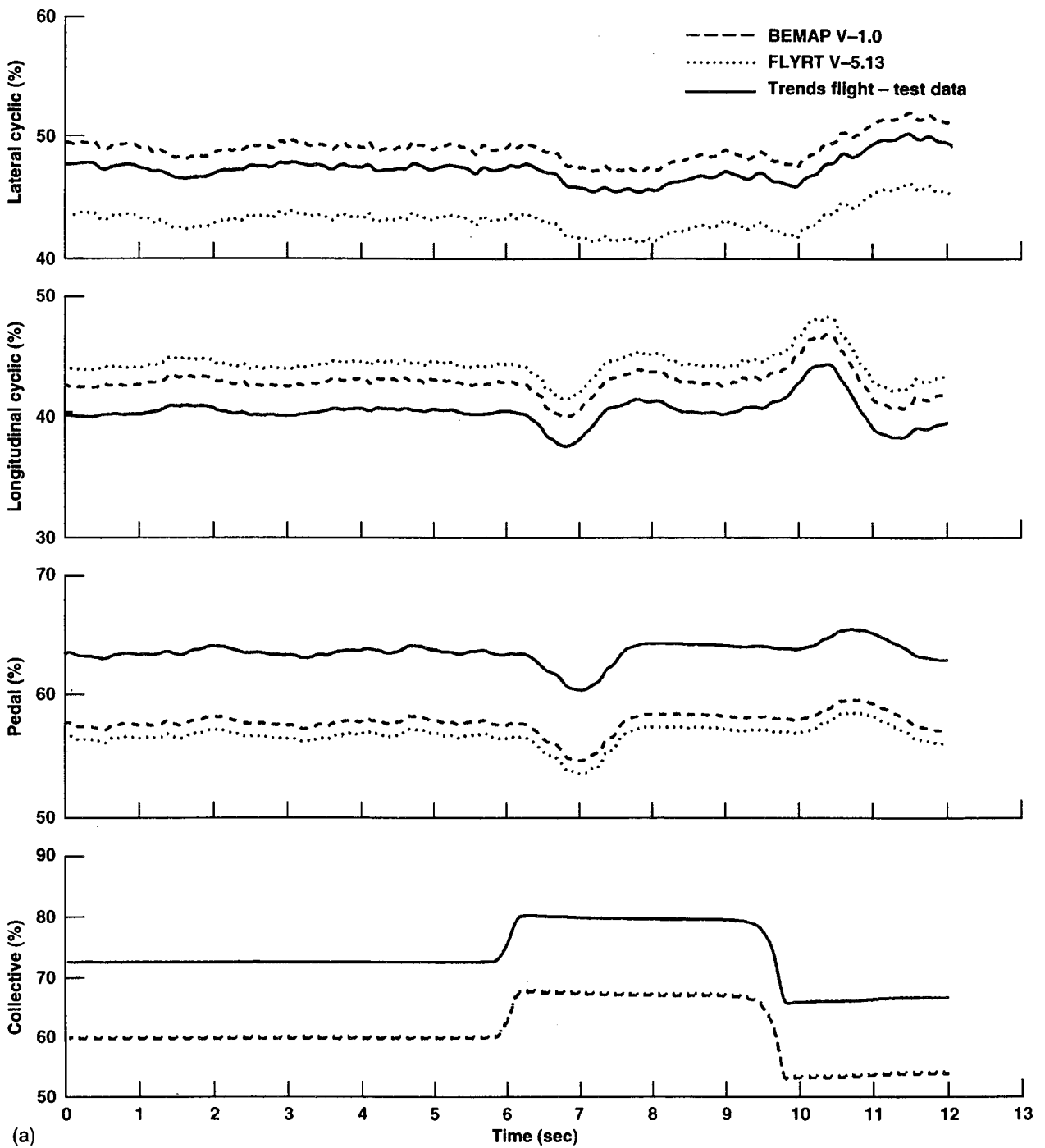


Figure 15. (a) Responses to collective doublet at 120 kts.

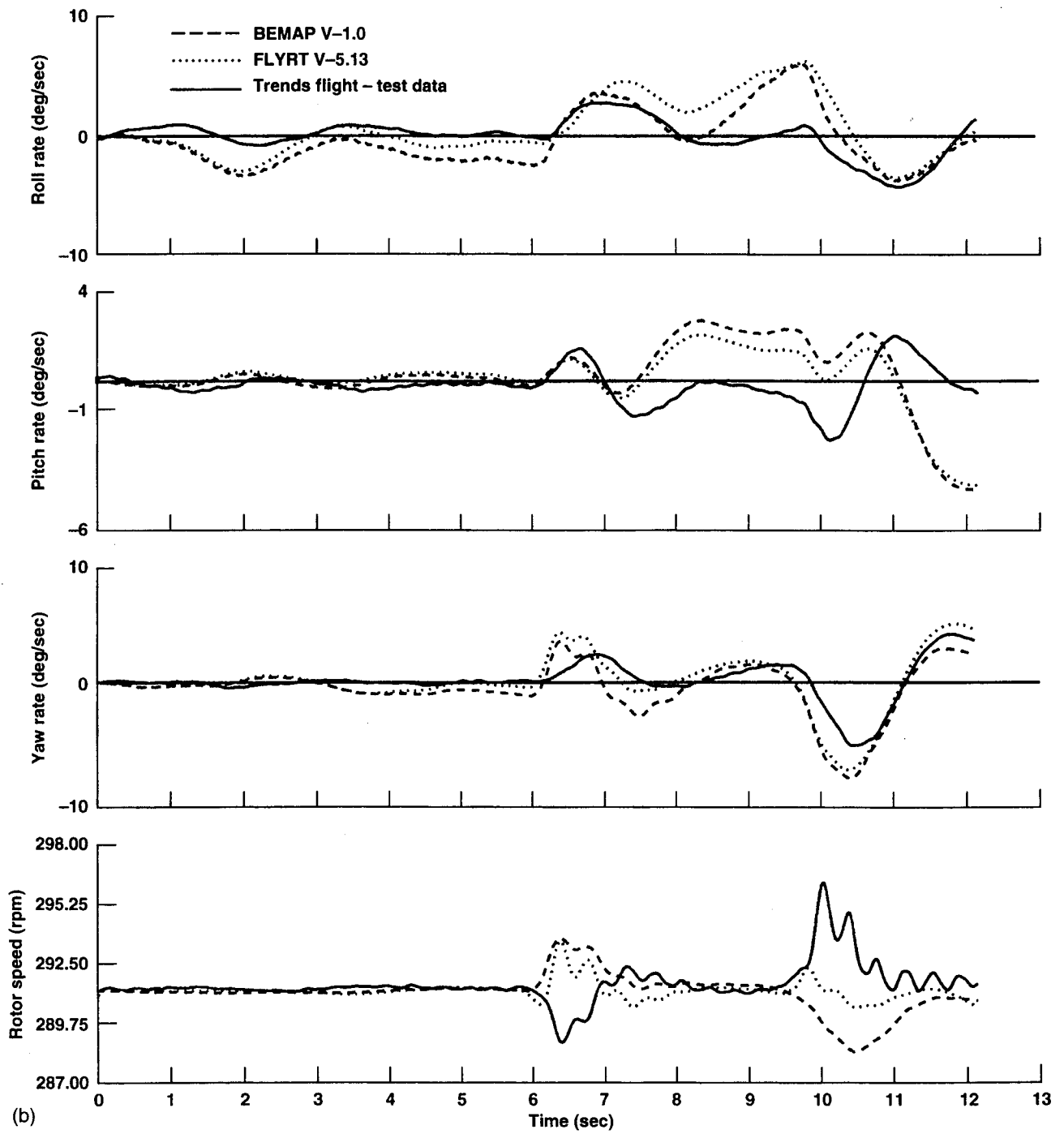


Figure 15. (b) Continued.

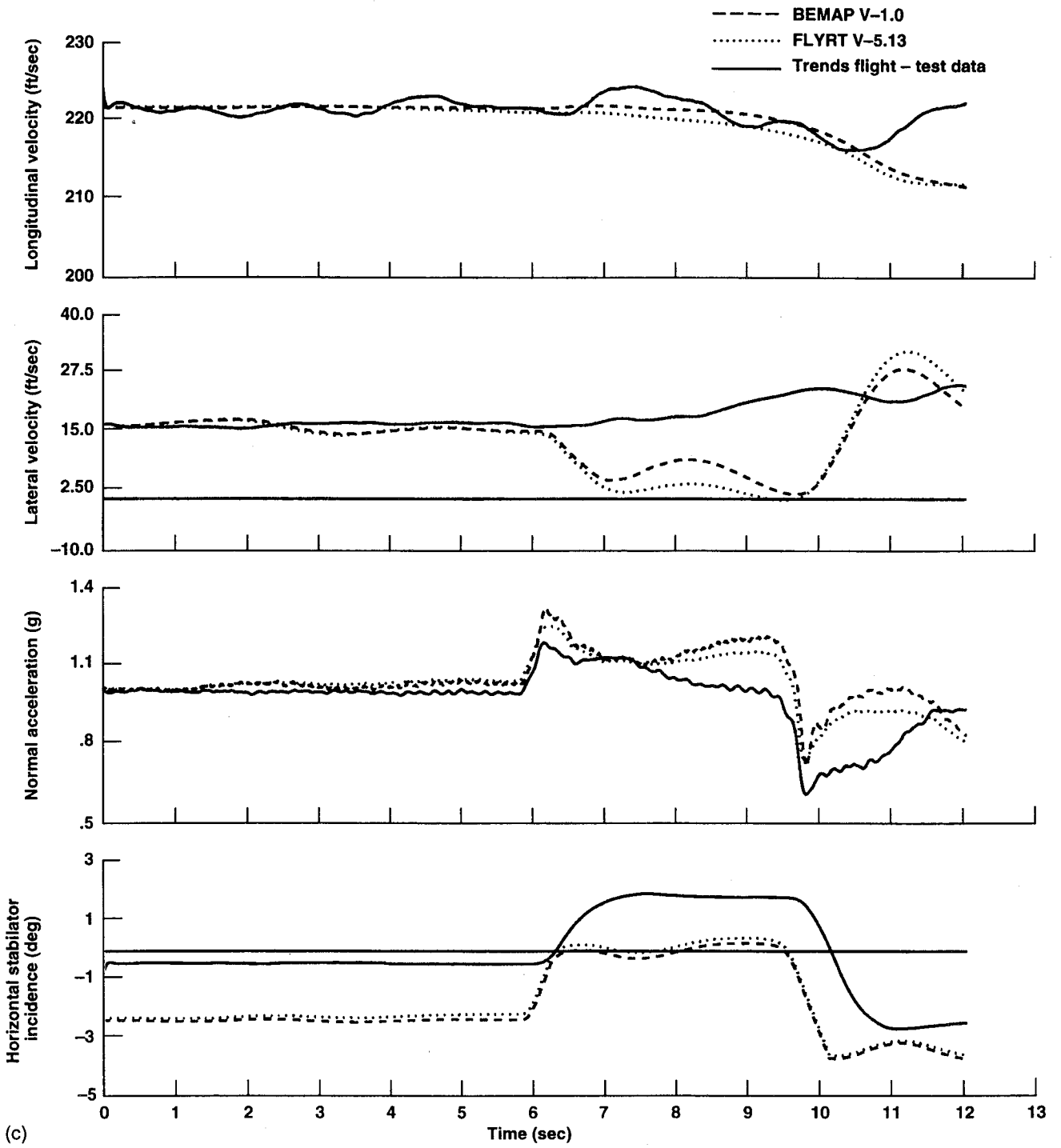


Figure 15. (c) Concluded.

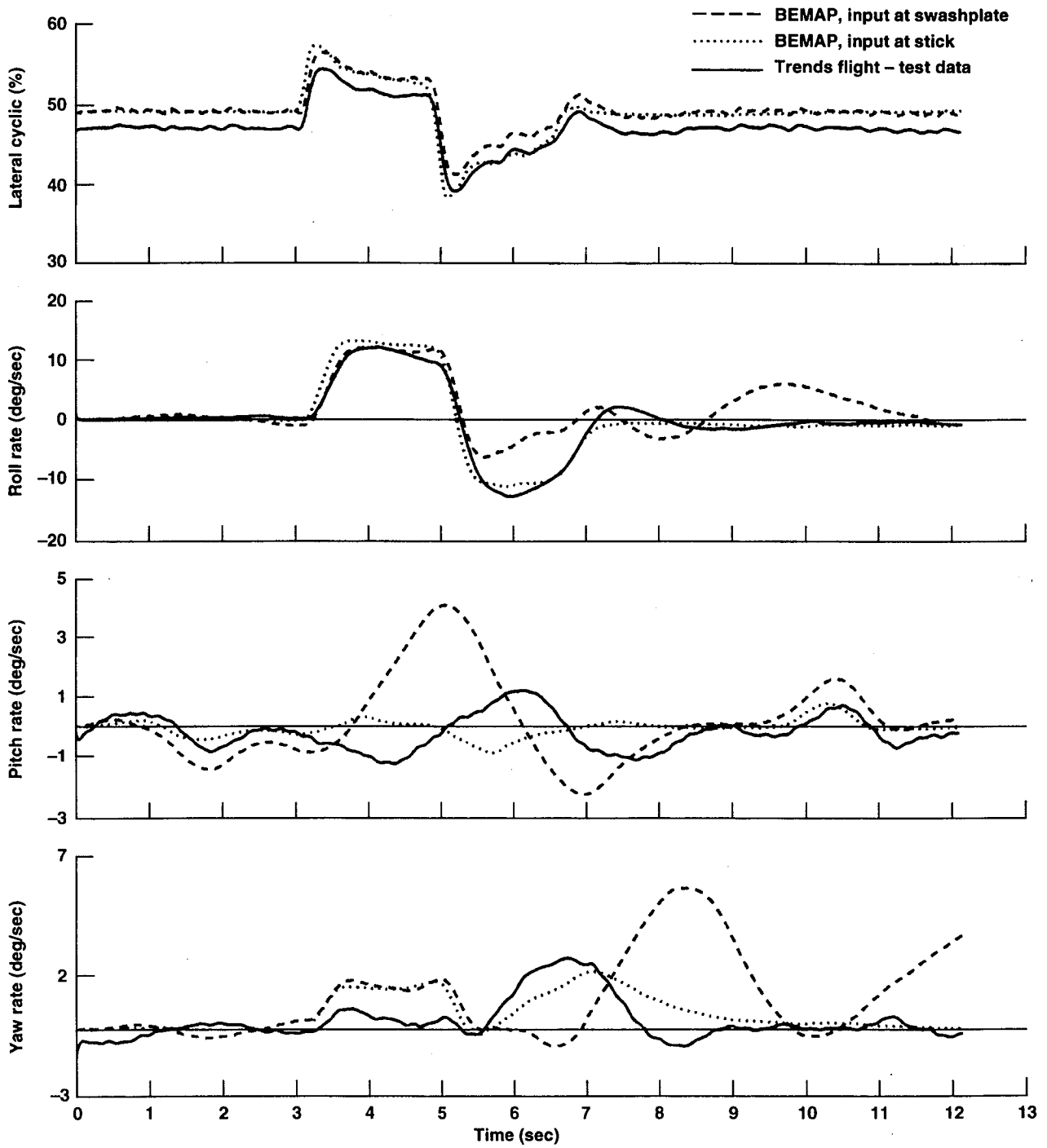


Figure 16. Lateral doublet at 60 kts, input at stick.

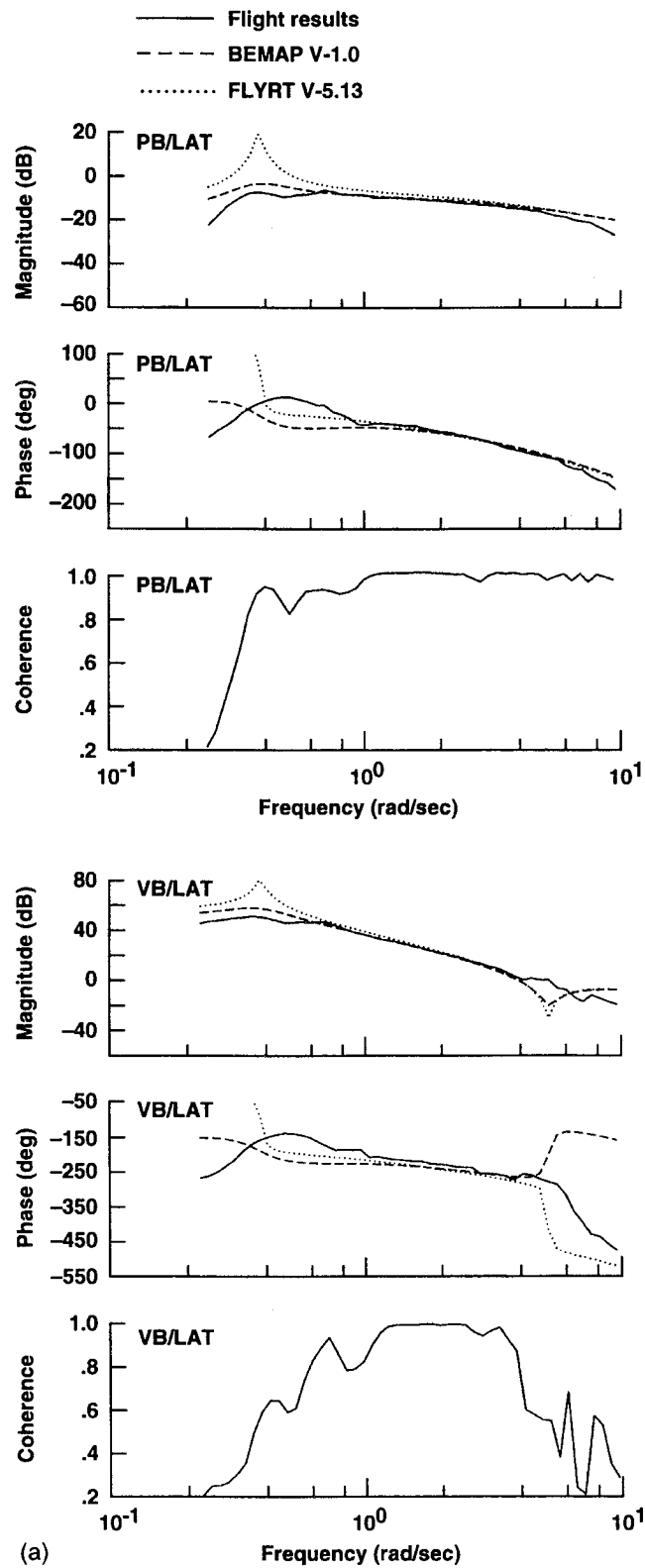


Figure 17. (a) Comparison of BEMAP responses with flight at hover.

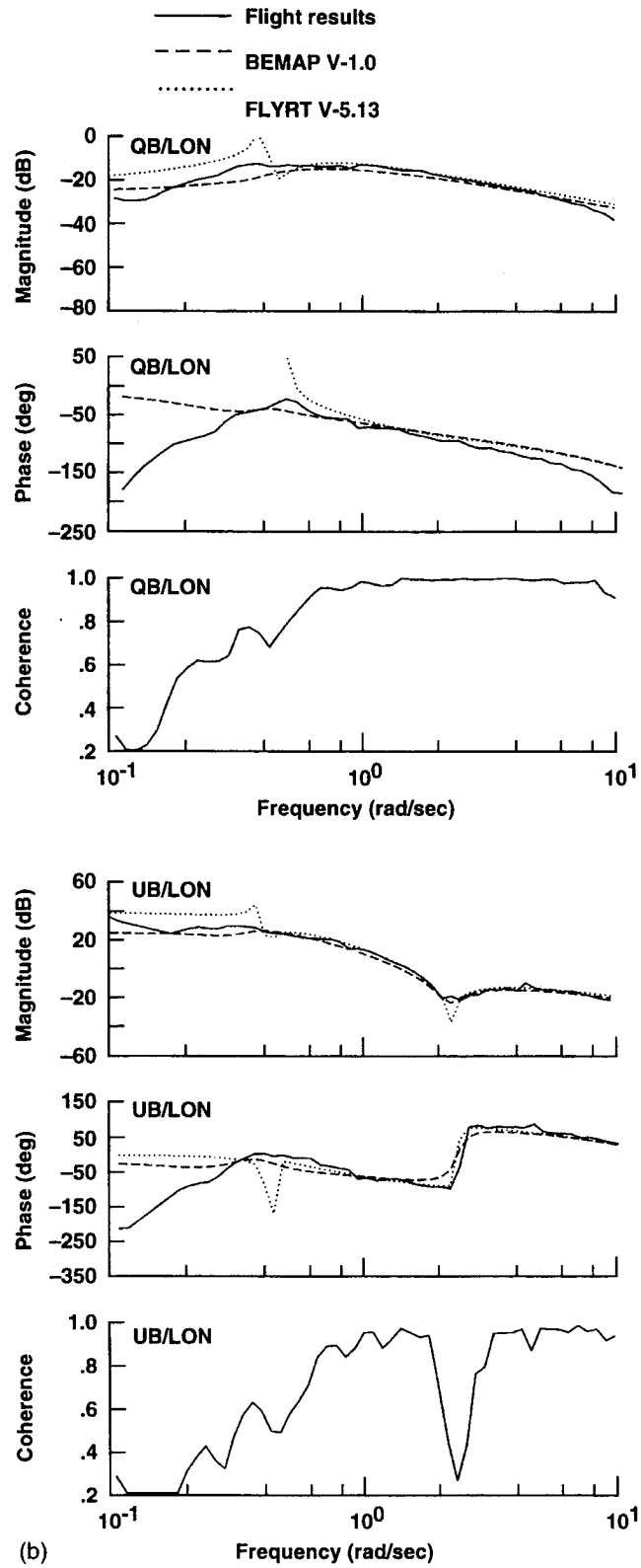


Figure 17. (b) Continued.

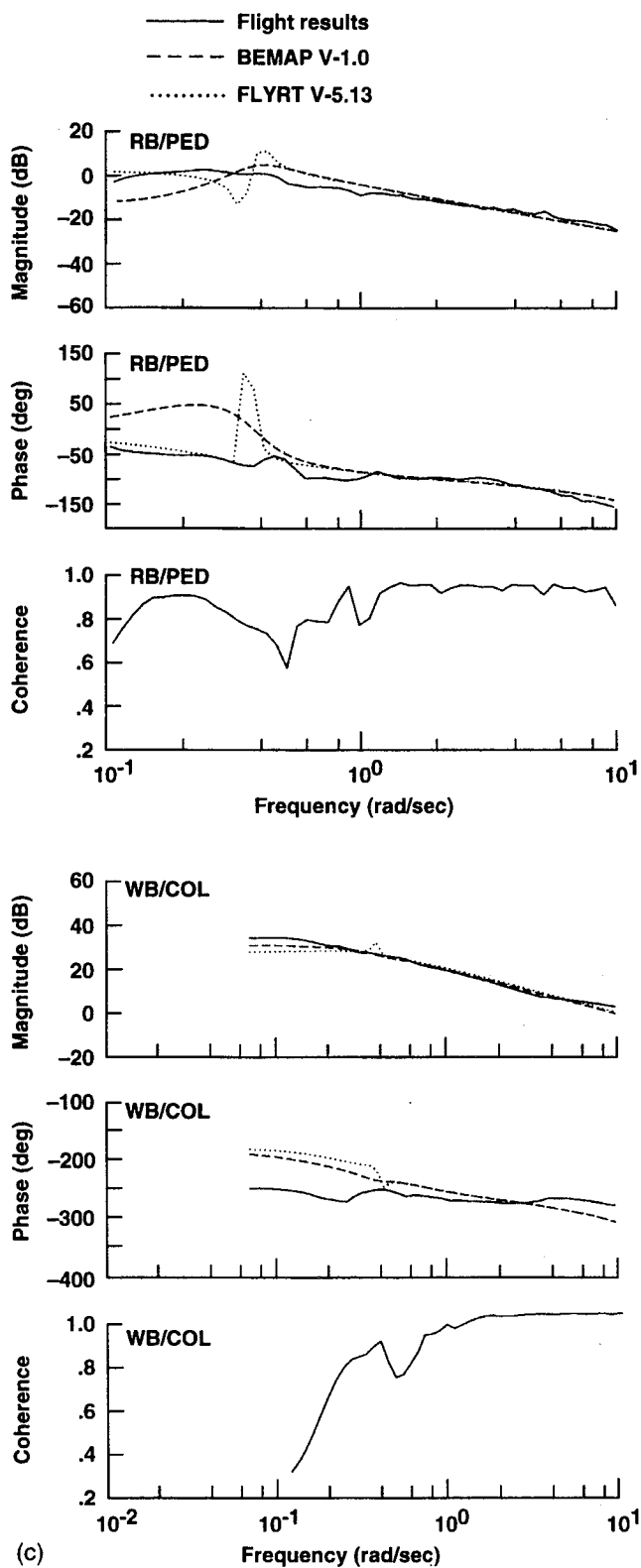


Figure 17. (c) Continued.

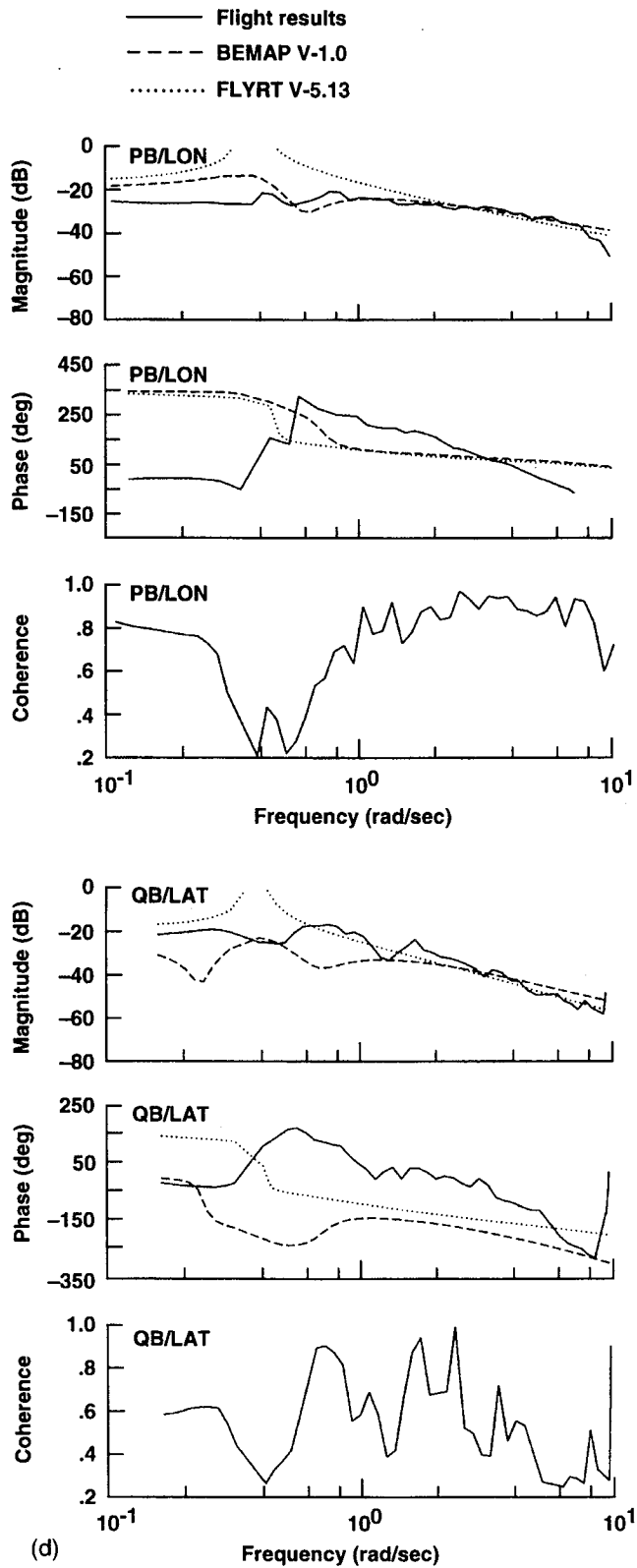


Figure 17. (d) Concluded.

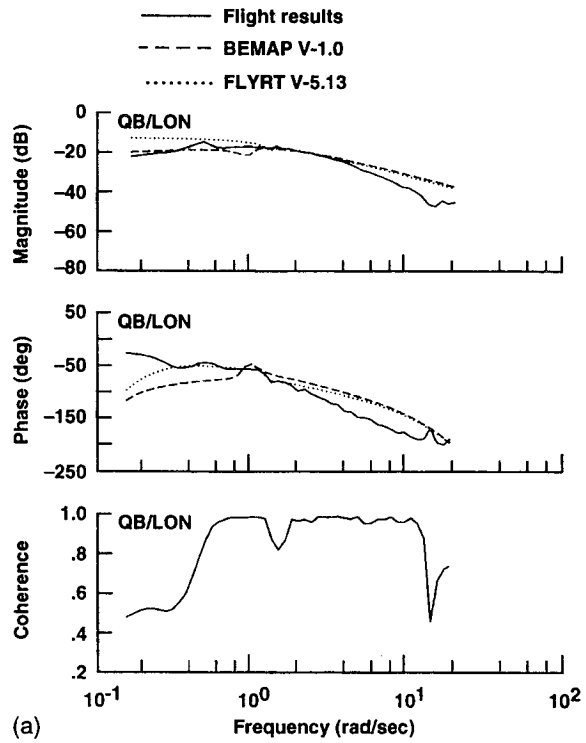
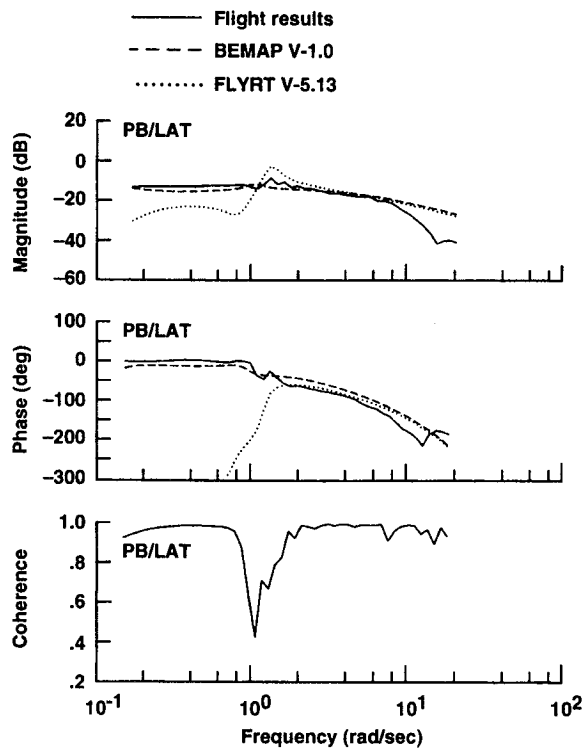


Figure 18. (a) Comparison of BEMAP responses with flight at 60 kts.

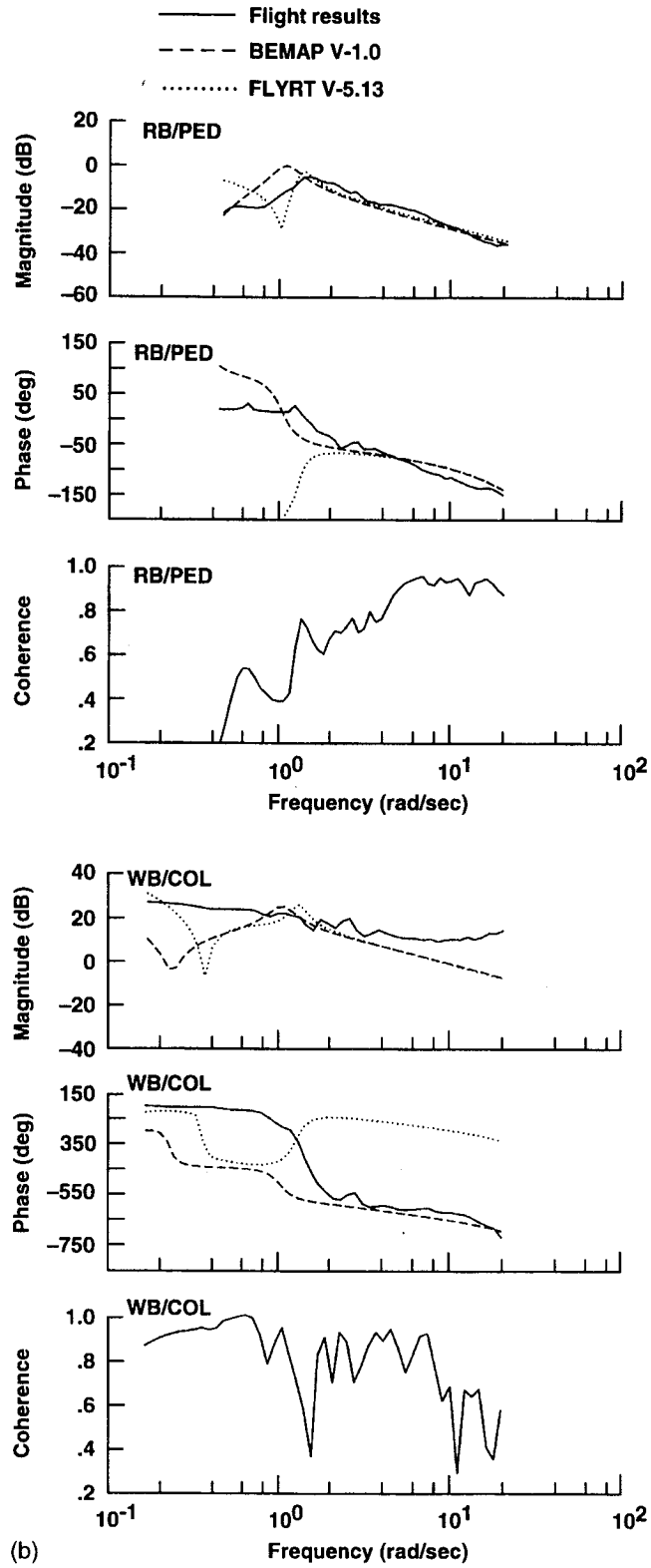


Figure 18. (b) Continued.

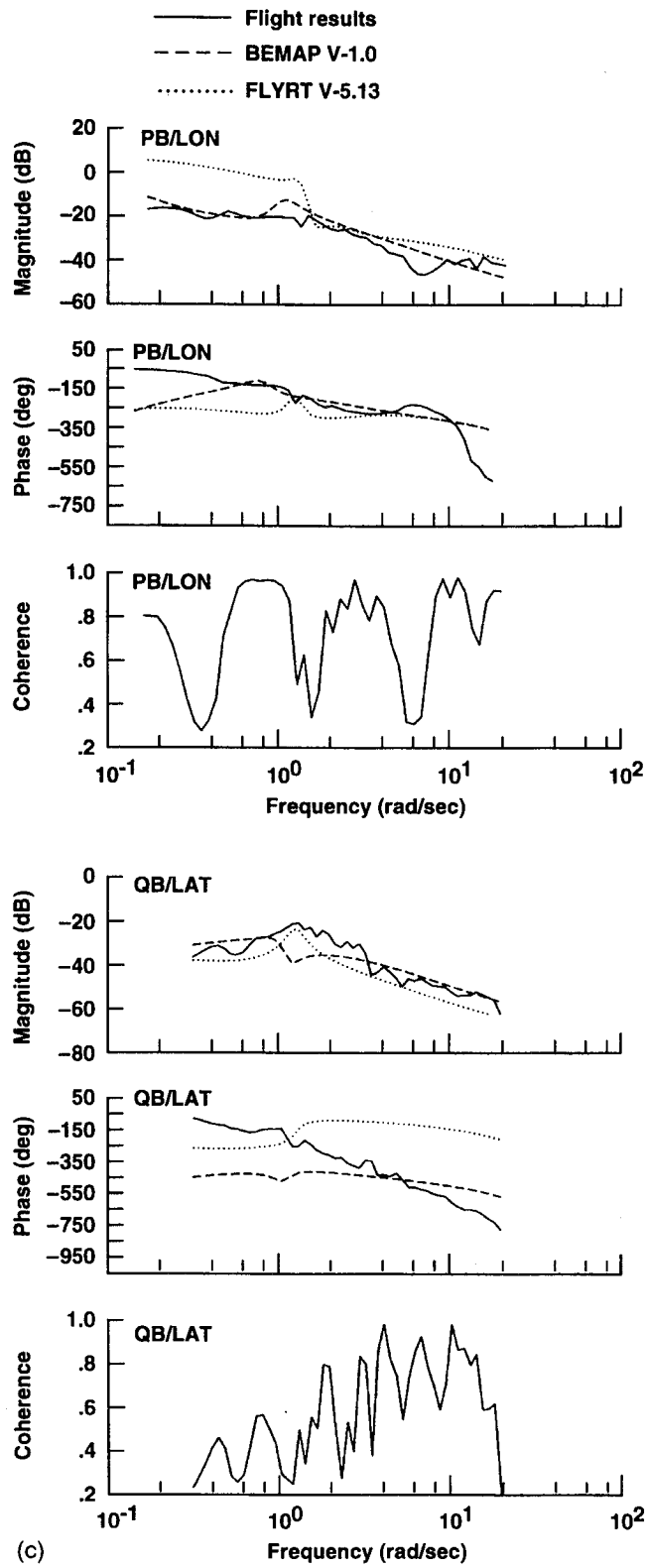


Figure 18. (c) Concluded.

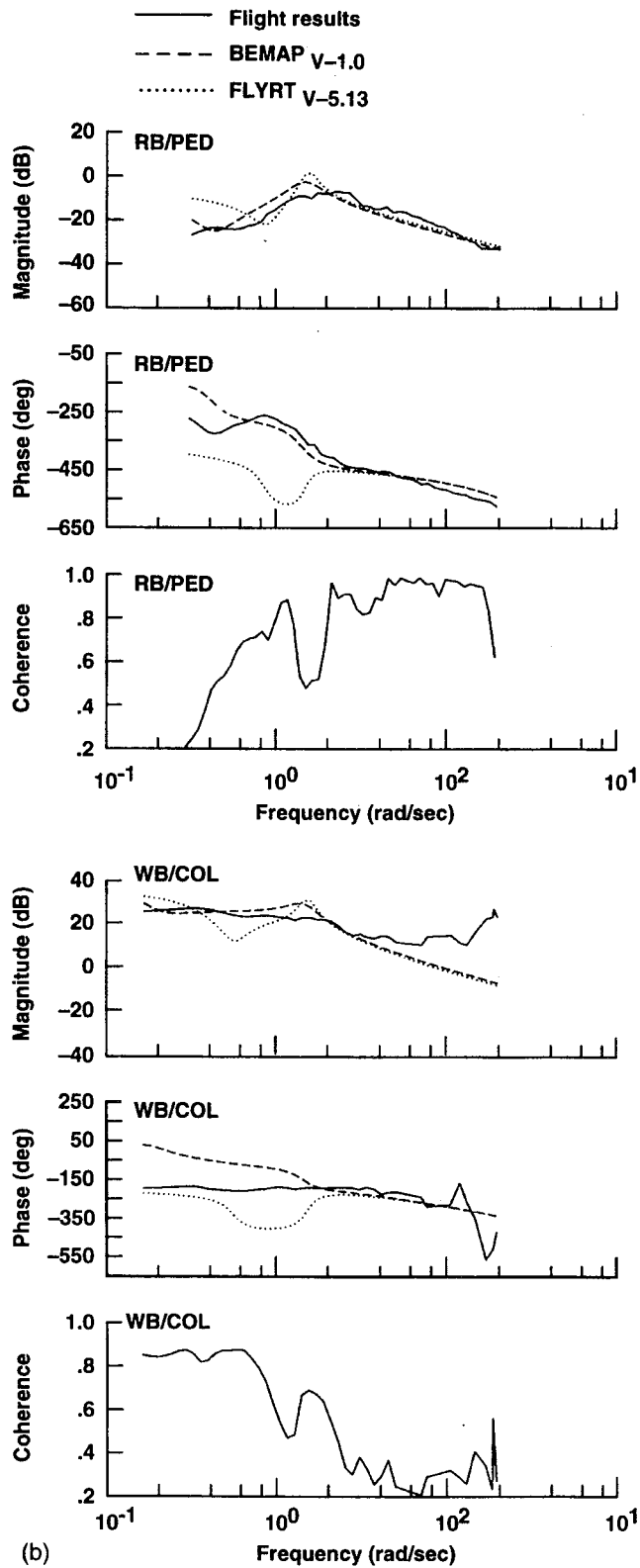


Figure 19. (b) Concluded.

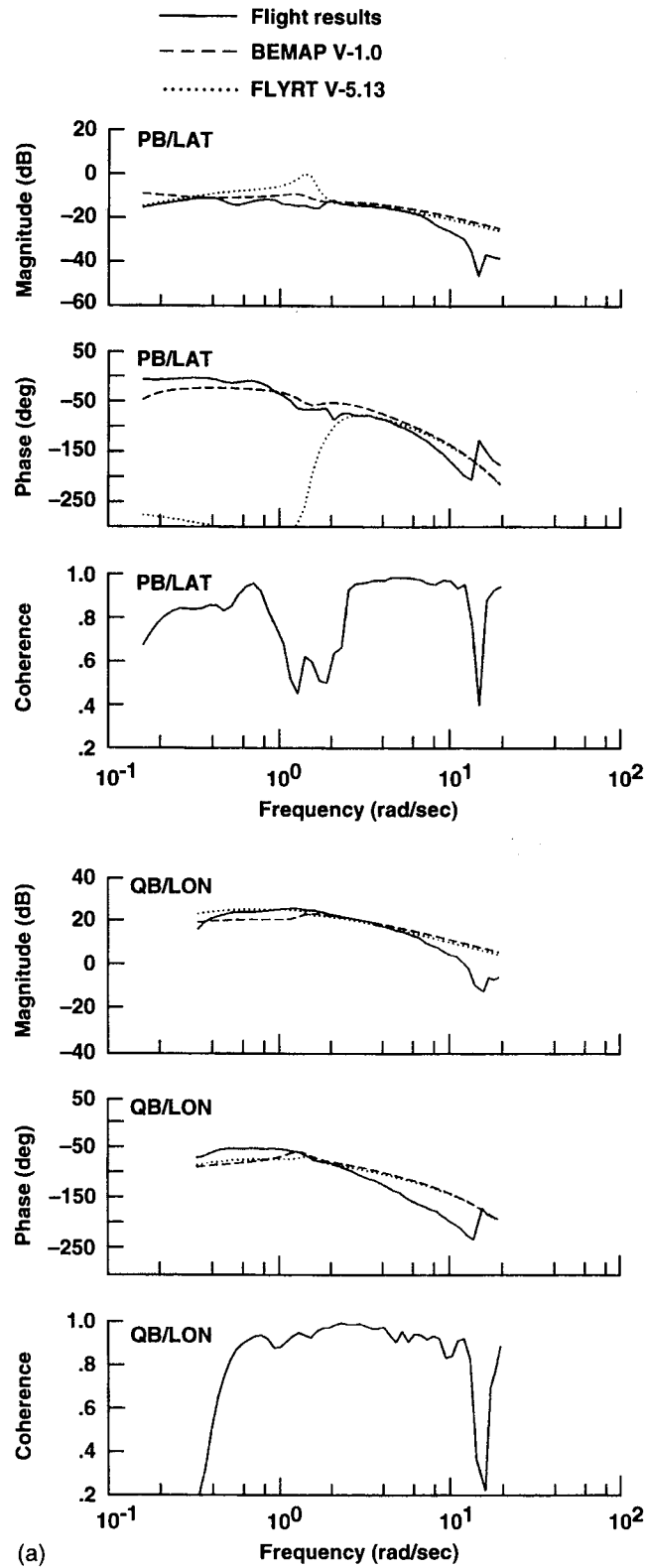


Figure 19. (a) Comparison of BEMAP responses with flight at 120 kts.

REPORT DOCUMENTATION PAGE

Form Approved
OMB No. 0704-0188

Public reporting burden for this collection of information is estimated to average 1 hour per response, including the time for reviewing instructions, searching existing data sources, gathering and maintaining the data needed, and completing and reviewing the collection of information. Send comments regarding this burden estimate or any other aspect of this collection of information, including suggestions for reducing this burden, to Washington Headquarters Services, Directorate for Information Operations and Reports, 1215 Jefferson Davis Highway, Suite 1204, Arlington, VA 22202-4302, and to the Office of Management and Budget, Paperwork Reduction Project (0704-0188), Washington, DC 20503.

1. AGENCY USE ONLY (Leave blank)		2. REPORT DATE April 1995	3. REPORT TYPE AND DATES COVERED Technical Memorandum	
4. TITLE AND SUBTITLE Development and Validation of a Blade-Element Mathematical Model for the AH-64A Apache Helicopter			5. FUNDING NUMBERS 505-59-36	
6. AUTHOR(S) M. Hossein Mansur				
7. PERFORMING ORGANIZATION NAME(S) AND ADDRESS(ES) Aeroflightdynamics Directorate, U.S. Army Aviation and Troop Command, Ames Research Center, Moffett Field, California			8. PERFORMING ORGANIZATION REPORT NUMBER A-95034	
9. SPONSORING/MONITORING AGENCY NAME(S) AND ADDRESS(ES) National Aeronautics and Space Administration Washington, DC 20546-0001 and U.S. Army Aviation and Troop Command, St. Louis, MO 63120-1798			10. SPONSORING/MONITORING AGENCY REPORT NUMBER NASA TM-108863 USAATCOM TR-94-A-022	
11. SUPPLEMENTARY NOTES Point of Contact: M. Hossein Mansur, Ames Research Center, MS 211-2, Moffett Field, CA 94035-1000; (415) 604-6037				
12a. DISTRIBUTION/AVAILABILITY STATEMENT Unclassified-Unlimited Subject Category - 01			12b. DISTRIBUTION CODE	
13. ABSTRACT (Maximum 200 words) A high-fidelity blade-element mathematical model for the AH-64A Apache Advanced Attack Helicopter has been developed by the Aeroflightdynamics Directorate of the U.S. Army's Aviation and Troop Command (ATCOM) at Ames Research Center. The model is based on the McDonnell Douglas Helicopter Systems' (MDHS) Fly Real Time (FLYRT) model of the AH-64A (acquired under contract) which was modified in-house and augmented with a blade-element-type main-rotor module. This report describes, in detail, the development of the rotor module, and presents some results of an extensive validation effort.				
14. SUBJECT TERMS Blade-element; Helicopter, Mathematical model			15. NUMBER OF PAGES 98	
			16. PRICE CODE A05	
17. SECURITY CLASSIFICATION OF REPORT Unclassified	18. SECURITY CLASSIFICATION OF THIS PAGE Unclassified	19. SECURITY CLASSIFICATION OF ABSTRACT	20. LIMITATION OF ABSTRACT	

